

P. 2 my
(NASA-CR-120124) UNSTEADY AERODYNAMIC
ANALYSIS OF SPACE SHUTTLE VEHICLES.
PART 3: BOOSTER INTERFERENCE EFFECTS
Final Technical Report (Lockheed Missiles
and Space Co.) 103 p HC \$7.25 CSCL 22B

N74-15531

Unclas
26372

SQT

August 1973

LMSC-D352320

UNSTEADY AERODYNAMIC ANALYSIS OF SPACE SHUTTLE VEHICLES

Part III: BOOSTER INTERFERENCE EFFECTS

Final Technical Report

Prepared by

I. Peter Reding

Research Specialist Aero-Thermodynamics

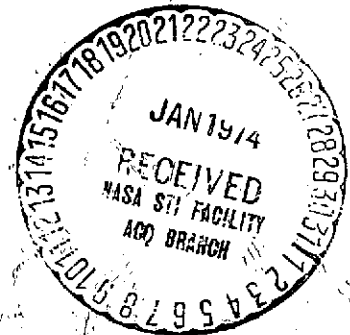
Lars E. Ericsson

Consulting Engineer, Engineering Technology

Prepared Under Contract NAS 8-28130

for

National Aeronautics and Space Administration



Lockheed

MISSILES & SPACE COMPANY, INC.
SUNNYVALE, CALIFORNIA

UNSTEADY AERODYNAMIC ANALYSIS
OF SPACE SHUTTLE VEHICLES

Part III: BOOSTER INTERFERENCE
EFFECTS

by

J. Peter Reding and Lars E. Ericsson

August 1973

Prepared Under Contract NAS 8-28130

for

National Aeronautics and Space Administration

Lockheed Missiles & Space Company, Inc.
A Subsidiary of Lockheed Aircraft Corporation
Sunnyvale, California

ABSTRACT

An investigation of the interference flow field on the space-shuttle boost configuration has been made. The results show that the interference effects can dominate the shuttle aerodynamics. Furthermore, vortices shed from shock-induced flow separations on the forward portion of the vehicle affect the aerodynamic loads on the aft portion of the booster. Thus, the forebody and aft-body flow fields are coupled. This coupling and the associated time lag due to the finite convection speed of the vortices furnish a mechanism whereby the unsteady aerodynamics can cause undamping of certain low frequency elastic modes of the booster. A preliminary order-of-magnitude analysis of the aeroelastic stability of the shuttle booster indicates that negative aerodynamic damping could occur for at least one bending mode and be of sufficient magnitude to dominate the structural damping. The implication of these results (i. e., the possibility of undamped oscillations leading to structural failure), is serious enough to warrant further, more detailed analysis.

PRECEDING PAGE BLANK NOT FILMED

CONTENTS

Section		Page
	ABSTRACT	iii
	ILLUSTRATIONS	vii
1	INTRODUCTION	1-1
2	ORBITER LOADS	2-1
	2.1 Orbiter Loads at $\alpha = 0$	2-1
	2.2 Orbiter α -Derivatives	2-4
	2.3 Orbiter β -Derivatives	2-9
	2.4 Orbiter Loads $\alpha > 0$	2-11
3	BOOSTER LOADS	3-1
4	PLUME-INDUCED EFFECTS	4-1
5	CONCLUSIONS	5-1
6	RECOMMENDATIONS FOR FURTHER STUDY	6-1
7	REFERENCES	7-1
Appendix		
A	NOMENCLATURE	A-1

PRECEDING PAGE BLANK NOT FILMED

PRECEDING PAGE BLANK NOT FILMED

LIST OF ILLUSTRATIONS

Figure		Page
1.	Space Shuttle Liftoff Configurations	1-2
2.	Effect of Booster Interference on Orbiter Loads at $\alpha = 0$, ATP Configuration	2-13
3.	Effect of Booster Interference on 049 Orbiter Bottom-side Pressures (Ref. 3)	2-15
4.	Shadowgraph Photographs of the ATP Booster at $\alpha = 0$	2-19
5.	Shadowgraph Photographs of the Current Boost Configuration at $\alpha = 0$	2-22
6.	Effect of Booster Interference on Oilflow Patterns on the Bottom of the Orbiter at $\alpha = 0$, $\beta = 0$	2-23
7.	Interference Flow Field	2-27
8.	Typical Nose Induced Separation Flow Field at $M = 0.9$ (Ref. 5)	2-31
9.	Flow Field Due to SRM-HO Tank Interference	2-32
10.	Detail of, Retro-rocket, Spike-induced Separated Flow Region, $M = 0.9$, $\alpha = 10$	2-33
11.	Effect of Retro-rocket, Spike-induced, Separation on Orbiter Bow Shock, $M = 1.46$, $\alpha = 10^\circ$	2-34
12.	Effect of Booster Interference on Orbiter Stability at $\alpha = 0$, ATP Configuration	2-35
13.	Effect of Booster Interference on Orbiter Bottom-Side Pressures at $\alpha = 6^\circ$, 049 Configuration (Ref. 3)	2-37
14.	Effect of Angle of Attack on Interference Flow Field, ATP Booster with Forward SRMs, $M = 1.46$	2-38
15.	Comparison of Orbiter Pitch Characteristics for Two SRM Positions, ATP Booster, $M = 1.46$	2-39
16.	Effect of Angle of Attack on the Orbiter Bottom-side Oilflow Patterns, ATP Configuration with Normal SRM Position, $M = 1.46$	2-40
17.	Leeside Interference Flow Patterns on the ATP Booster at $M = 1.46$, $\alpha = 10^\circ$	2-41

ILLUSTRATIONS (Continued)

Figure		Page
18.	Shadowgraph Photographs of ATP Booster at $M = 1.46$, $\alpha > 0$	2-42
19.	Effect of Booster Interference on Orbiter Lateral-Directional Stability at $\alpha = 0$, ATP Configuration	2-43
20.	Effect of Sideslip Angle on the Interference Flow Field, ATP Configuration, $\alpha = 0$	2-45
21.	Comparison of Booster Element Shoulder Pressures, 049 Booster, $\alpha = 0$	3-5
22.	Comparison of HO Tank and SRM Pressures, 049 Booster, $M = 0.95$, $\alpha = 0$ (Ref. 12)	3-6
23.	Comparison of Orbiter, HO Tank, and SRM Pressures, 049 Booster, $M = 1.2$, $\alpha = 0$ (Refs. 3 and 12)	3-7
24.	Comparison of Orbiter, HO Tank, and SRM Pressures, 049 Booster, $M = 1.96$, $\alpha = 0$ (Refs. 3 and 12)	3-8
25.	Effect of Orbiter Mounting Posts on the Interference Flow Field on the Bottom of the 049 Orbiter, $M = 1.96$	3-9
26.	Interference Effects on HO Tank Load Distribution, 049 Booster, $M = 1.2$ (Ref. 12)	3-10
27.	HO Tank Lumped Loads for 049 Booster, $M = 1.2$	3-11
28.	Comparison of Interference Effects on HO Tank $\phi = 0$ Pressures, 049 Booster, $M = 1.2$, $\alpha = 0$ (Ref. 12)	3-12
29.	Effect of α on HO Tank Load Distribution for HO Tank and Orbiter, 049 Booster, $M = 1.2$ (Ref. 12)	3-13
30.	Comparison of HO Tank and SRM $C_{N\alpha}$ Distributions at $\alpha = 0$ for the 049 Booster, $M = 1.2$ (Ref. 12)	3-14
31.	SRM Lumped Loads for 049 Booster, $M = 1.2$	3-15
32.	Effect of α on Skewing the Expansion-Separation Vortices Between HO Tank and SRM	3-16
33.	3.64-Hz Symmetric Mode of the 049 Booster (Ref. 17)	3-17
34.	Effect of the Induced Interference Load on the Aerodynamic Damping Factor of the 049 Booster, 3.64-Hz Symmetric Mode, $M = 1.2$, $\alpha = 0$	3-18
35.	Effect of HO Tank and SRMs on the Aerodynamic Damping Factor of the 0.49 Booster, 3.64-Hz Symmetric Mode, $\alpha = 0$	3-19

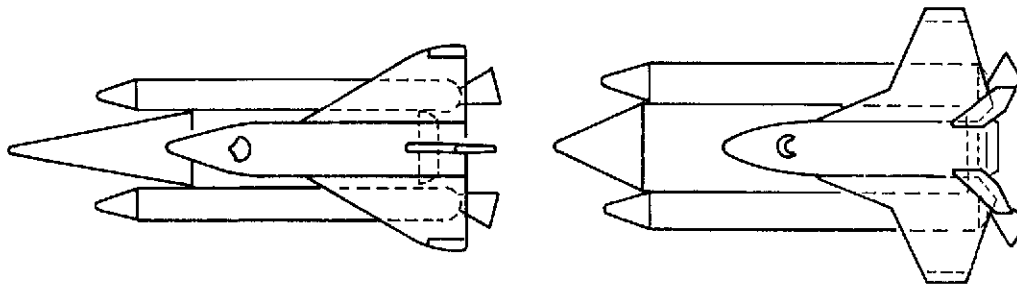
ILLUSTRATIONS (Continued)

Figure		Page
36.	Plume-Induced Effects on Pitch Stability, 040A Booster	4-6
37.	Postulated Effects of Small α and β on Plume-Induced Separation	4-8
38.	Plume-Induced Effects on Directional Stability, 040A Booster (Ref. 18)	4-9
39.	Effect of Solid Plumes on the Aerodynamic Damping Factor of the 3.64-Hz Symmetric Mode of the 049 Booster	4-10
40.	Typical Asymmetric Modes of the 049 Booster (Ref. 17)	4-11
41.	Effect of Solid Plumes on the Aerodynamic Damping Factor of Some Typical Asymmetric Modes of the 049 Booster	4-13
42.	Comparison of Solid and Gaseous Plumes and Nozzle Load Effects	4-15
43.	Comparison of Configurations Used in Plume Tests	4-16
44.	Effect of Gaseous Plumes and Nozzle Loads on the Aerodynamic Damping Factor of the 3.64-Hz Symmetric Mode of the 049 Booster, $M = 1.6$	4-18
45.	Effect of Gaseous Plumes and Nozzle Loads on the Aerodynamic Damping Factor of Some Typical Asymmetric Modes of the 049 Shuttle Booster, $M = 1.6$	4-19
46.	Effect of Solid Plumes and Booster Interference on the Aerodynamic Damping of the 3.64-Hz Symmetric Mode of the 049 Booster	4-20
47.	Effect of Gaseous Plumes and Booster Interference on the Aerodynamic Damping of the 3.64-Hz Symmetric Mode of the 049 Booster, $M = 1.6$	4-21
48.	Evidence of Leading Edge Vortex-Exhaust Plume Interaction, 15 Inches Downstream of Nozzles, $M = 1.6$, $\alpha = -4^\circ$	4-22

Section 1 INTRODUCTION

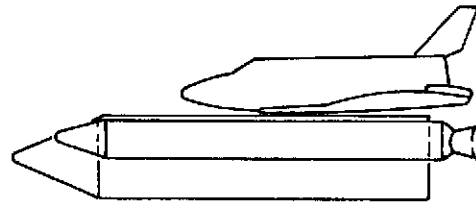
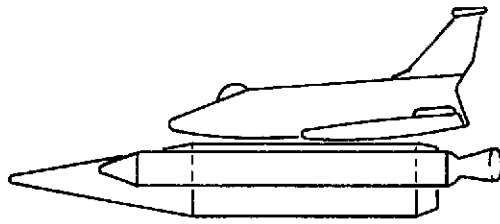
Estimation of the dynamic effects of the interference flow field from static data requires a good understanding of the origins of the various aerodynamic load components on the vehicle. Specifically, one must know what portion of the aerodynamic load at each station on the vehicle is the result of local flow conditions and what portion is dependent on flow conditions elsewhere. Furthermore, in order to estimate the convection speed and resulting time lag, one must understand how the load at a given body station is influenced by conditions elsewhere. This information can only be determined experimentally for a configuration as complicated as the shuttle lift-off configuration. Unfortunately, detailed load distribution results are not yet available for the current lift-off configuration. In fact, there is not sufficient information available for any one shuttle boost configuration to supply the input for a detailed aeroelastic analysis.

The general layout of the shuttle lift-off configuration has not changed drastically within the past year and a half. That is, the booster has consisted of a delta-wing orbiter, external hydrogen-oxygen (HO) tank, and two solid rocket motors (SRMs) in a parallel-stage configuration. Figure 1 shows some representative configurations including the original (040A) and the current. Obviously, these configurations are similar enough that the salient features of the interference flow field will be preserved. Data from three of these configurations (a, b, c, in Fig. 1) have been used as the basis for some insight into the aerodynamics of the interference flow field and for some preliminary judgments on how the various interference effects affect the elastic ascent-vehicle dynamics.

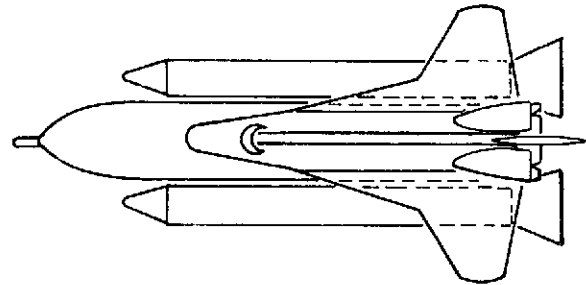
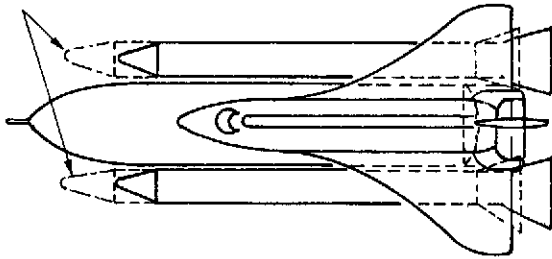


a) 040 A CONFIGURATION

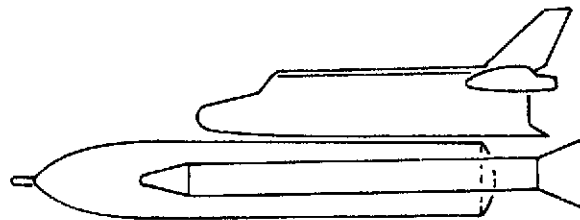
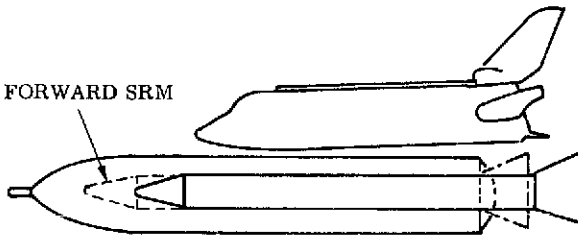
b) 049 CONFIGURATION



FORWARD SRM



FORWARD SRM



c) ATP CONFIGURATION

d) CURRENT CONFIGURATION

Figure 1. Space Shuttle Liftoff Configurations

Section 2 ORBITER LOADS

In March of 1973, a special static-wind tunnel test was run in the Marshall Space Flight Center (MSFC) 14-inch wind tunnel to investigate the interference flow field. It was originally intended to measure forces and moments on all body components as each component was pitched and yawed separately. This was intended to supply the interference derivatives needed for a preliminary aeroelastic analysis. The force data were to be supplemented with detailed flow-visualization results which would define the major interference effects responsible for the measured interference derivatives. Unfortunately, the configuration was undergoing redesign at this time, making it difficult to define a test configuration. Also, there were great demands on the facility for wind tunnel time. As a result, it was decided to conduct a flow visualization test on an updated ATP boost configuration (Fig. 1c). Loads were also measured on the orbiter because it was expected that the delta wing would constitute the dominant load-carrying surface. Fortunately, these results, along with data on the orbiter alone (Ref. 1, 2) and pressure distribution results for the 049 vehicle (Ref. 3), furnish much information about the various flow interference effects that have a dominating influence on the orbiter loads.

2.1 ORBITER LOADS AT $\alpha = 0$

The loads on the orbiter at $\alpha = 0$ are difficult to generalize. Whereas C_{A_o} is generally reduced by interference effects (Fig. 2a), C_{N_o} and C_{m_o} are dependent upon the booster configuration in a more complicated manner (Figs. 2b, 2c).^{*} Pressure distribution results on the 049 orbiter (Ref. 3) give valuable information about

^{*}Note that although the orbiter is at a 1.5-degree attitude relative to the booster, C_{m_o} and C_{N_o} are presented for orbiter $\alpha = 0$, that is, with the orbiter axis aligned with the free stream velocity vector.

the booster interference effects. The presence of the booster constricts the flow under the orbiter nose. The result is a channel-like flow condition where the reduction in the effective channel area accelerates the subsonic ($M = 0.9$) stream, causing a drop in pressure under the nose (Fig. 3a), with resulting decreases of both C_{A_0} and C_{N_0} (Fig. 2). At low supersonic speeds (e.g., $M = 1.2$), the flow approaching the contracting channel under the orbiter nose is also subsonic owing to the strong detached normal shock forward of the orbiter (Fig. 4b). Thus, the pressure under the nose is similarly decreased (Fig. 3b). At slightly higher supersonic speed, $M = 1.46$, the bow shock becomes oblique (Fig. 4c) and the flow behind it is supersonic. However, the flow is eventually decelerated to subsonic speeds by the ensuing shock reflections (Fig. 4c). The pressures under the nose do not vary smoothly because of these multiple shock reflections (Figs. 3c and 3d). At $M = 1.96$, a reflected shock raises the pressures near the nose. Downstream the flow is subsonic, and the pressure distribution resembles the $M = 1.2$ distributions. (Compare Fig. 3b and 3c.) Thus, the drag reduction due to interference effects, which was large at low Mach numbers, is diminished at $M = 1.96$ and nearly vanishes at $M = 4.96$, when more positive pressures exist under the nose (Figs. 2a, 3d). Of course, in addition to alteration of the nose pressure, the loss in total pressure through the multiple bow shock system of the booster will contribute to the orbiter drag loss. This effect evidently is greater than the increased nose pressures at $M = 4.96$, and some net drag reduction still results.

Actually, the flow between the orbiter and booster resembles inlet flow more than simple channel flow. For example, the pressure distribution results for the 049 configuration (Fig. 3) and the shadowgraph for both the ATP (Fig. 4) and the current booster configurations (Fig. 5) indicate that under the orbiter nose the flow is decelerated to subsonic speeds by a shock that stands generally just forward of where the wing leading edge joins the fuselage. In the case of the 049 orbiter, this is also just forward of the minimum cross-sectional area point between the orbiter and the HO tank. The mass flow under the nose is too great to be accommodated further downstream because of the added restriction of the wing. The shock decelerates the flow to subsonic speeds and spills the excess mass flow laterally. The downstream inlet flow then reexpands,

producing negative pressure under the rest of the fuselage. This model is probably somewhat oversimplified, considering the complicated geometry of the channel or inlet between the stages, (exemplified by the multiple shocks that appear between the stages of the current configuration, see Fig. 5). However, it does explain the salient features of the 049 configuration pressure distributions and the shadowgraph results for the modified ATP booster.

A similar inlet effect may also occur between the SRMs and the orbiter wing. This may cause one of the downstream shocks visible in the shadowgraph of the current booster (Fig. 5), and it explains why the pressures on the bottom of the orbiter wing are reduced substantially (compared with orbiter alone) at transonic speeds (Figs. 3a, 3b) and only slightly at higher speeds (Figs. 3c, 3d). This contributes to the reduced C_{N_o} due to booster interference for the normal SRM position. The orbiter nose load tends to dominate C_{m_o} because of its longer lever arm. The orbiter static stability data show that the interference effect on C_{m_o} is stabilizing (less positive) at transonic speeds when the load on the bottom of the nose is negative, and it is destabilizing (more positive) at supersonic speeds when the nose load is positive (Fig. 2c). The correlation is surprisingly good when one considers that only windward side effects are included and that the pressure and force data from two different configurations are used. These findings suggest that at low angles of attack, where the major interference effects occur on the windward side of the orbiter, the flow fields are not drastically different for the various configurations analyzed (Fig. 1).

Oilflow results indicate that there are sizable interference effects on the bottom of the orbiter near the trailing edge. When the SRMs are in the normal position, the dominant interference effect on the ATP configuration is generated by the HO tank (Fig. 6). * At supersonic speeds a normal shock, similar to a lip shock (Ref. 4),

*These oilflow results on the orbiter were obtained with the orbiter in the vicinity of the booster, as in Fig. 7. The configuration was disassembled to photograph the flow patterns between the stages.

stands on the HO tank base. This is not visible in all the shadowgraphs (most visible in Fig. 5) but its trace in the oilflow at the orbiter base is usually visible (Fig. 6). There also appears to be a minor interaction between the wing trailing edge and the SRM flare shock. This is most apparent for the current configuration (Fig. 6b). When the SRMs are forward, the SRM flare exerts a sizable interaction on the orbiter. This can be seen as divergent oil streaks at $M = 0.9$ and as a region of flow separation for $M > 1.0$ (Fig. 6a). The resulting high pressure field under the wing trailing edges causes the higher C_{N_o} and more negative (stabilizing) C_{m_o} for the forward SRM position (Figs. 2b, 2c).

2.2 ORBITER α -DERIVATIVES

The orbiter α -derivatives are the result of rather complicated flow interactions. In this section the interference flow field is examined first by use of oilflow and pressure data. These results are then used to postulate reasons for the measured interference effects on the orbiter α -derivatives.

Essentially four different types of interference flow fields exist: (1) subsonic for the normal boost configuration, (2) subsonic with SRMs forward, (3) supersonic for the normal boost configuration, and (4) supersonic with SRMs forward. These flows are illustrated in Fig. 7 by oilflow photographs (Figs. 7a-7e) and interpretive flow sketches (Figs. 7g-7j). Oilflow photographs of the current configuration show that the interference flow field is qualitatively similar to the ATP flow field (Fig. 7k, 7l). A photograph of the leeward side of the orbiter at $\alpha = 10^\circ$ shows the large degree of interference between booster and orbiter at high α (Fig. 7f). This is discussed in more detail later in this report.

The effect of the SRM nose cone on the HO tank flow field is very apparent in the oilflow photographs (Fig. 7b-7e). The flow opposite the cone diverges as a result of the high pressure region generated by the cone. It then converges aft of the shoulder as it is affected by the SRM shoulder expansion. At $M = 0.9$, the channel-like flow between the SRM and the HO tank tends to make the cone shoulder pressures more negative, thus increasing the adverse pressure gradient aft of the shoulder. As a result, flow separation occurs at the shoulder of the 17° SRM nose cone (compare the

oilflows of Figs. 7b and 8), which ordinarily would not experience nose-induced separation (Ref. 6). The adverse SRM pressure-gradient is shared by the HO tank, resulting in a separation bubble on the HO tank opposite the SRM* (illustrated in more detail in Fig. 9). The separation pockets are vented via pairs of counter-rotating vortices (Ref. 5) as depicted in the flow sketches (Figs. 7g and 7h).

At $M = 1.46$, the SRM bow shock causes flow separation where it impinges aft of the HO tank shoulder (Figs. 7d and 7i). The shock impinges in an area where the boundary layer is already weakened by the adverse pressure gradient aft of the shoulder. Separation occurs as long as the shock is nearly normal to the local flow. However, as the impingement region moves around the HO tank, it becomes more oblique until at some point it no longer separates the flow. At this point, the separation sheds a pair of vortices on top and bottom of the HO tank. However, the shock impingements continue around the body; and another region of separation is formed where the oblique SRM shocks interact with the impinging orbiter bow shock in a manner similar to Edney's type D interaction (Ref. 7), causing separation of the boundary layer forward of the orbiter. This separation is also vented by a pair of vortices.

When the SRMs are in the forward position, their bow shocks impinge on a portion of the HO tank with high pressures and favorable pressure gradients. Thus, no separation occurs on top of the HO tank until the orbiter shock is encountered (Figs. 7e, 7j). This separation is now further aft, under the orbiter nose, because the orbiter bow shock is no longer assisted by the converging SRM shocks, as it was when the SRMs were in the normal position. A separation, vented by a pair of vortices, also occurs in the gap between the HO tank and the SRM opposite the SRM shoulder. A region of flow separation is also generated on the top of the SRM by the lateral extension of the orbiter bow shock; this is relatively independent of SRM position (Figs. 7d, 7e).

*The red oil on the left SRM furnishes evidence of the common separated-flow recirculation region between the HO tank and the SRM. Red oil is picked up from the stagnation region on the HO tank and recirculated forward and around the SRM via the nose-induced separation there.

A region of flow separation also occurs on the retrorocket housing. This spike-induced separation is caused by the back pressure of the HO tank nose on the relatively small retrorocket. Detailed examination of the oilflow results indicates that the flow resembles that of nose-induced separation (compare Figs. 10 and 8). At angle of attack, the separation is vented via a pair of counter-rotating vortices.* These vortices are shed upward over the nose of the HO tank and ultimately impinge on the orbiter nose. They carry red oil with them from the retrorocket, thus accounting for the red oil on the orbiter nose at $\alpha > 0$ (Figs. 7b-7e). The influence of these vortices is probably responsible for the discontinuity in the orbiter bow shock seen in Fig. 11.

To complete the interpretation of the oilflow photographs, the leeside orbiter flow field is also shown in the flow sketches shown in Fig. 7g-7j. Wing leading edge vortices and vortices venting local separation bubbles on top of the canopy and on the side of the orbiter fuselage are evident. The flow field appears essentially unaffected by the booster interaction (Fig. 7) except, perhaps, for some delay of formation of the leading edge vortex at the wing root (Figs. 7g-7j). This may be due to a local reduction of the angle of attack because of the flow-straightening effect of the HO tank. Whatever the case, the flow field is similar to that on the 040A orbiter (see Ref. 8 for a detailed discussion of the leeside flow effects on the orbiter aerodynamics).

The foregoing discussion demonstrates that the flow field over the shuttle lift-off configuration is dominated by multiple regions of separated flow that have the potential of influencing the downstream flow field via shed vortices that vent the separated flow regions. These effects and the associated alterations in the orbiter loads are described in the following discussion.

The oilflow results at $M = 0.9$ (Figs. 7b & 7c) illustrate the reason for the differences in orbiter C_A between forward and normal SRM positions (Fig. 2a). The flow turns outboard on the HO tank well ahead of the orbiter when the SRMs are in the forward

*At $\alpha = 0$, two or more separated flow cells exist, each vented by a pair of vortices (Ref. 5).

position, because of the effect of the SRM separation. Thus, the subsonic stream is decelerating. However, for the normal SRM position, the streamlines are converging because the SRMs impose an effective restriction on the flow. Therefore, the flow is accelerated and the pressures are relatively lower under the nose, giving the smaller C_{A_0} at $M = 0.9$. At supersonic speeds, the shock configuration forward of the orbiter dominates C_{A_0} . When the SRMs are in the normal position, the strong normal shock emanating from the separation on the HO tank gives a higher static pressure under the orbiter nose than does the oblique shock that occurs when the SRMs are forward (Fig. 4c). Thus, C_{A_0} is greater for the normal SRM position at supersonic speeds (Fig. 2a).

The orbiter α -derivatives (Fig. 12) are generally reduced by interference effects. That is, C_{N_α} is reduced and C_{m_α} is less stable (less negative). The center-of-pressure movements are relatively small (Fig. 12c), indicating that no large force couples are involved in the interference effects. Pressure distribution results on the 049 orbiter show a large reduction of the wing lift at angle of attack because of the presence of HO tank and SRMs (Fig. 13). The lift reduction is caused by pressure changes (of about the same degree) on both the top and bottom of the wing. The booster seems to act as a flow straightener, reducing the angle of attack of the orbiter. That is, the freestream flow is turned more or less parallel with the booster by the time it encounters the orbiter. Thus, the effective orbiter angle of attack is decreased and, therefore, C_{N_α} and C_{m_α} are also decreased. This decrease, of course, represents only an overall or effective reduction in α . At certain locations, e.g., above the gap between the SRM and HO tank, the angle of attack on the orbiter may be locally greater than that of freestream flow.

Comparison between SRM positions shows that the forward position gives the highest C_{N_α} and the most stable C_{m_α} . This is because in the forward position the SRM flare shock induces flow separation on the orbiter wing. The differences between the derivatives for the SRM positions are greatest at low supersonic speeds (Figs. 12a, 12b). These data are consistent with the experience on the Apollo-Saturn V

launch vehicle where the shock-induced separation was found to be most significant in the Mach number range $1.0 \leq M \leq 2.0$ for a slightly less steep flare $[16^\circ 44'$ SII-S4B interstage flare (Ref. 9) as compared to the 17° SRM flare]. The standard explanation for the increased orbiter $C_{N\alpha}$ based on the Apollo-Saturn experience would be that the leeside boundary layer on the SRM is thickened via forebody cross-flow effects and, as a consequence, the shock-induced separation forward of the SRM flare grows with angle of attack (Ref. 10). As the separation grows forward of the flare, the shock-impingement point on the bottom of the orbiter likewise moved forward, giving a greater $C_{N\alpha}$ and a more stable $C_{m\alpha}$, all in agreement with the experimental results in Figs. 12a and 12b. However, this explanation does not agree with the flow visualization results.

Oilflow results at $M = 1.46$ (Fig. 14) show that the separation point on the orbiter wing directly above the SRM does not move when α is increased from 0 to 5 degrees; and it tends to move back near the wing root, which is located directly above the gap between the SRM and the HO tank (compare Figs. 4a and 14b). At $\alpha = 10^\circ$, the separation on the bottom of the orbiter wing has vanished (Fig. 14c). However, as the normal force and pitching moment still are greater than for the normal SRM position (Fig. 15), some influence from the SRM flare remains. This is also indicated by the more divergent streamlines on the wings at $\alpha = 10^\circ$ with the SRM forward (compare Figs. 14 and 16). Evidently the shock still impinges on the orbiter wing but does not separate the boundary layer.

The oilflow results indicate that the shock-induced separation does not grow with angle of attack on the leeside of the SRM for either the forward or the normal SRM position. A strong reattachment zone down the leeward meridian energizes the boundary layer, thus precluding the separation growth (Fig. 17); this finding is also verified by shadowgraph photographs for the normal SRM position (Fig. 18).* The reattachment results from the downwash between the adjacent vortices which vent the SRM separation

*Shadowgraphs for the normal SRM are used to illustrate the constant SRM flare shock position with α , since the shadow of the HO tank does not obscure the point of origin of the SRM flare shock as it does for the SRM forward configuration.

caused by the orbiter bow shock and the HO separation caused by the SRM bow shock (Figs. 7d, 7e). Crossflow raises both vortices from their $\alpha = 0$ positions near the lateral medians, causing them to dominate the leeside flow on the SRM. Crossflow, particularly that ahead of the vortex shedding point, determines the strength as well as the path of the vortex; this is similar to the situation for the leading edge vortices on delta wings (Ref. 11). Thus, the retarding of the SRM shock-induced separation is dependent upon flow conditions at the SRM shoulder.

The suppression of this shock-induced separation growth is not the only factor in the elimination of the separation growth on the windward side of the orbiter wing. The wing boundary layer is also energized by flow jetting through the slot between the SRM and HO tanks. This is due to the local cross-flow effects and to flow entrainment between the inboard SRM vortex and the outboard HO tank vortex that is shed from the interaction of the SRM bow shock with the HO tank. [It is difficult to determine to what extent the effect of the outboard HO tank vortex will be negated by the counter rotating inboard HO tank vortex that is shed from the separation forward of or under the orbiter (depending on SRM configuration).]

The question of the greater stability and normal force for the forward SRM position (Fig. 15) is still unanswered because the shock-induced separation forward of the flare does not grow with α . The shadowgraphs for the normal SRM position show that the flare shock steepens with angle of attack (Figs. 4a, 18a, 18b). This implies a static pressure rise aft of the shock as α increases. Possibly, the same shock steepening for the forward SRM position would give the pressure rise over a larger area, explaining the greater $C_{N\alpha}$.

2.3 ORBITER β -DERIVATIVES

The effects of booster interferences on the orbiter lateral-directional stability characteristics at $\alpha = 0$ are summarized in Fig. 19. The booster reduces the directional stability derivative $(C_{n\beta})$ but increases the roll stability $(-C_{\ell\beta})$. The side-force derivative $(C_{Y\beta})$ is slightly more negative. It is well known that the crossflow on a body

of revolution reaches maximum near the lateral meridian. This explains the observed alteration of the orbiter directional characteristics by the booster. The increased sidewash over the booster, particularly the HO tank nose, causes the observed changes. The oilflow results in Fig. 20 illustrate this. The sidewash over the HO tank nose is roughly twice the freestream value. Compare the oil streaks with the freestream velocity vector which is accurately drawn to indicate $\beta = 5^\circ$. Thus, the orbiter nose experiences an increased effective sideslip angle β , which results in a more negative $C_{Y\beta}$ at the nose, with corresponding negative increment of $C_{n\beta}$. Thus, $C_{Y\beta}$ is more negative and $C_{n\beta}$ is less stable due to booster interference; these findings agree with the experimental results (Figs. 19a and 19b).

The roll derivative $C_{l\beta}$ reflects the effects of the booster-induced sidewash on the delta wing flow (Fig. 20). The increased effective sideslip β naturally increases the roll stability (Refs. 1, 2, and 11). Examination of the oilflow photographs on the bottom of the orbiter shows strong crossflow over the inboard portions of the windward wing while the flow over the corresponding portions of the leeward wing is aligned axially. Comparison of the oil patterns on top of the booster with those on the bottom of the orbiter suggests the reason for this asymmetry in sidewash. The sidewashing flow over the booster and between the stages is shed via the left or leeward vortex that vents the flow separation ahead of or under the orbiter nose (depending on SRM position). This vortex also rotates in a direction such that the entrained flow will oppose the sidewash (Figs 7i-7j). Thus, the sidewash is effectively killed over the leeward wing and SRM. Conversely, the sidewash on the windward wing is highly amplified by this vortex interaction, which explains the more than two-fold increase of local β over the freestream value. The net result is a more unstable $C_{l\beta}$ because the sidewash and, thus, the lift on the windward wing is increased while that on the leeward wing is decreased.

Sidewash also tends to sweep the top HO tank vortex leeward. This interacts with the flare-induced separation on the left (or leeward) SRM, causing the separation to shrink relative to the windward wing (Fig. 20b). This asymmetry in the regions of shock-induced separation on the wing gives a greater lift on the windward wing, which explains why $C_{l\beta}$ is more negative for the forward SRM position (Fig. 19b).

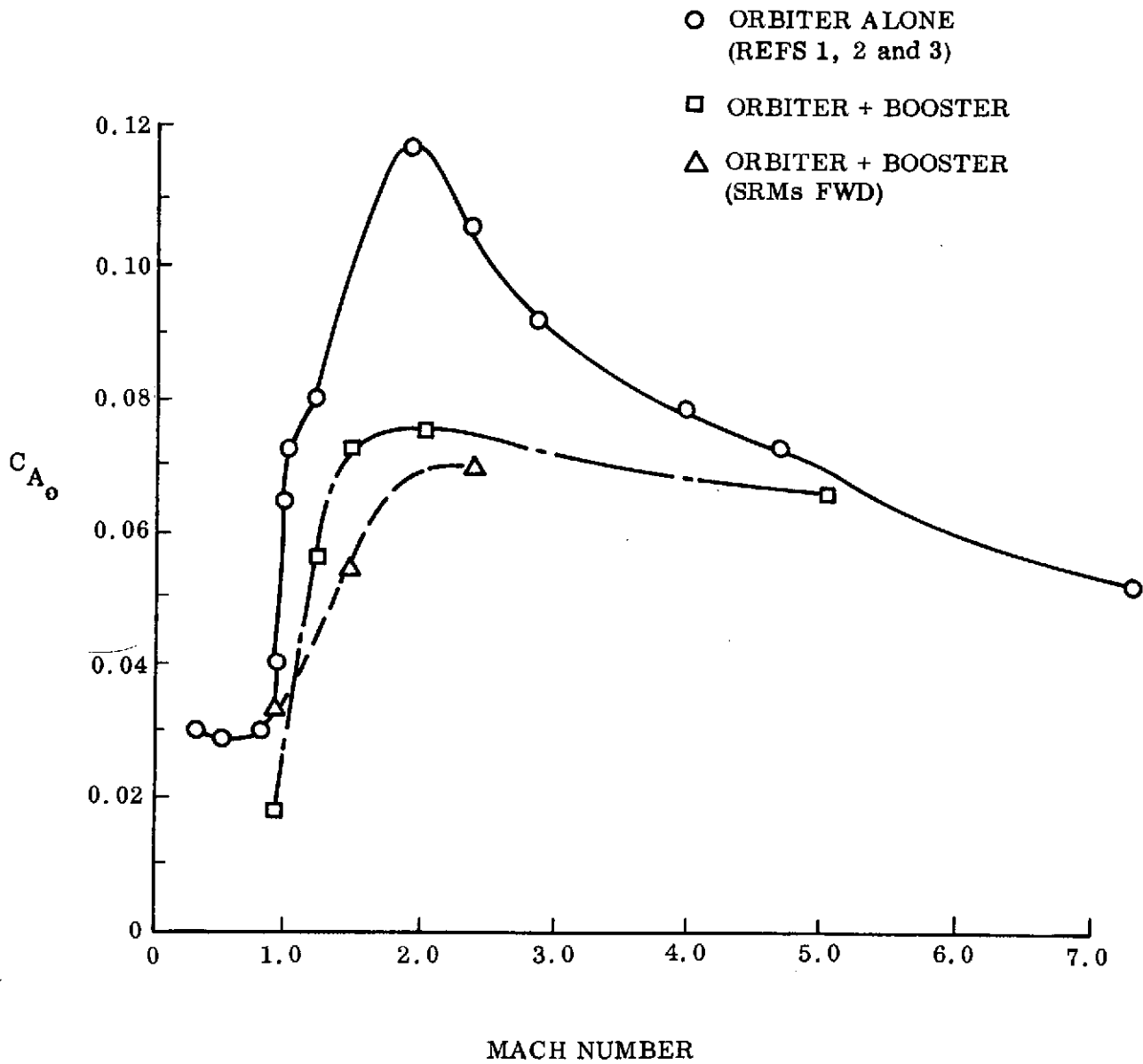
Finally, a close examination of the oilflow patterns on the leeward side of the HO tank show an asymmetry in the SRM shock traces on the HO tank just forward of the orbiter for the normal SRM position. The leeward SRM shock is steeper, suggesting higher static pressures aft of the shock on the leeward orbiter nose, thus producing positive $C_{Y\beta}$ and $C_{n\beta}$ increments. The shock from the SRM on the leeward side of the HO tank is steeper because it comes from the windward side of that SRM nose cone. Conversely, the SRM shock on the windward side of the HO tank is weaker because it comes from the lee side of that SRM nose. These asymmetric shock formations tend to further affect the orbiter loads. For the forward SRM position, the shock impingement occurs in an already high pressure region, causing only a limited local flow separation far forward of the orbiter. As the HO tank shoulder expansion occurs before the flow encounters the orbiter, the orbiter is not affected much by the shock impingement and imposed separation. The result is that $C_{Y\beta}$ and $C_{n\beta}$ are greater for the normal SRM position (Fig. 19).

2.4 ORBITER LOADS $\alpha > 0$

The preceding discussion involves zero-angle-of-attack characteristics almost exclusively. Also, only bottom (windward) side interference effects on the orbiter were considered in the discussion of measured interference effects. Because these windward side effects have been used with success in accounting for the measured orbiter characteristics, it is felt that they probably dominate the orbiter stability at $\alpha = 0$. However, this certainly is not conclusive; at $\alpha > 0$ this assumption becomes even more tenuous. The oilflow photograph of the orbiter at $\alpha = 10^\circ$ (Fig. 7f) shows that the booster flow also influences the top side orbiter flow. It is not difficult to see how the various vortices that vent the separated flow regions on the booster could be swept over the top of the orbiter at $\alpha > 0$. Furthermore, one can see the possibility of some dire consequences from such interactions. It is conceivable that vortices from the booster could interact with the leading edge vortex on the delta wing,

possibly resulting in sudden, discontinuous changes of the loading on the orbiter. This is not likely to happen symmetrically on both wings, because perfectly symmetric flow conditions are difficult to achieve in practice. Thus, the stability about all three axes would be affected.

To determine the complete effects of booster interference, both windward and leeward, one must ultimately obtain detailed load distributions. On the basis of the knowledge of unsteady flow phenomena gained from the described simple oilflow result, it is tempting to conclude that oilflow results of this type and orbiter pressure distribution results could make it possible to define the interference flow field well enough to be able to perform a meaningful aeroelastic analysis.



a. Axial Force

Figure 2. Effect of Booster Interference on Orbiter Loads at $\alpha = 0$, ATP Configuration (Sheet 1 of 2)

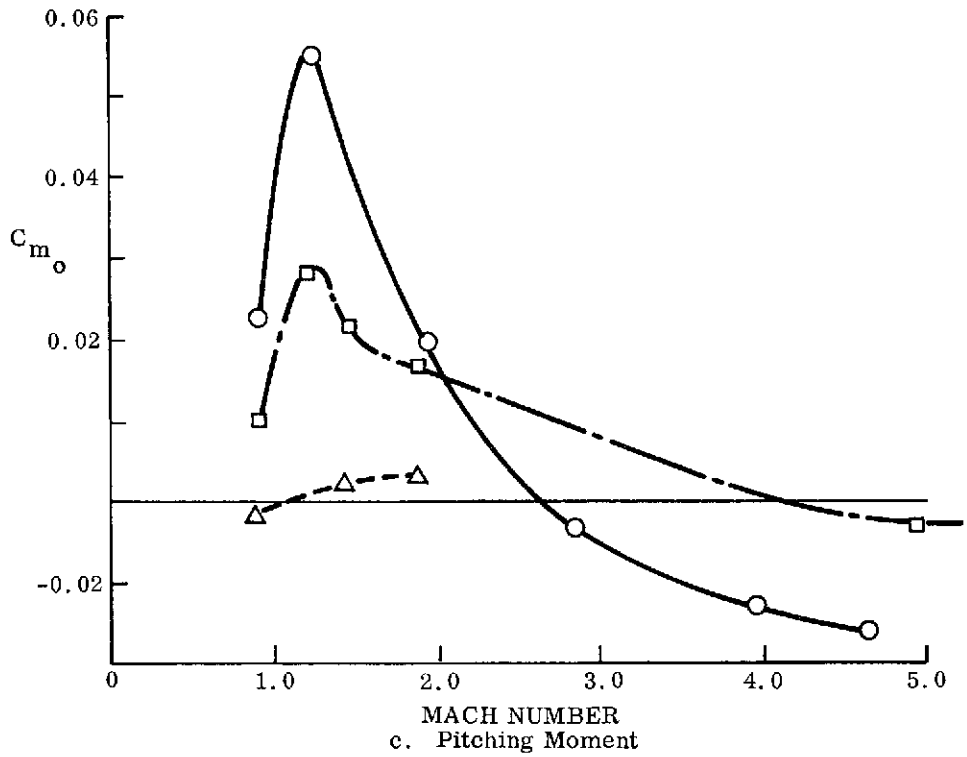
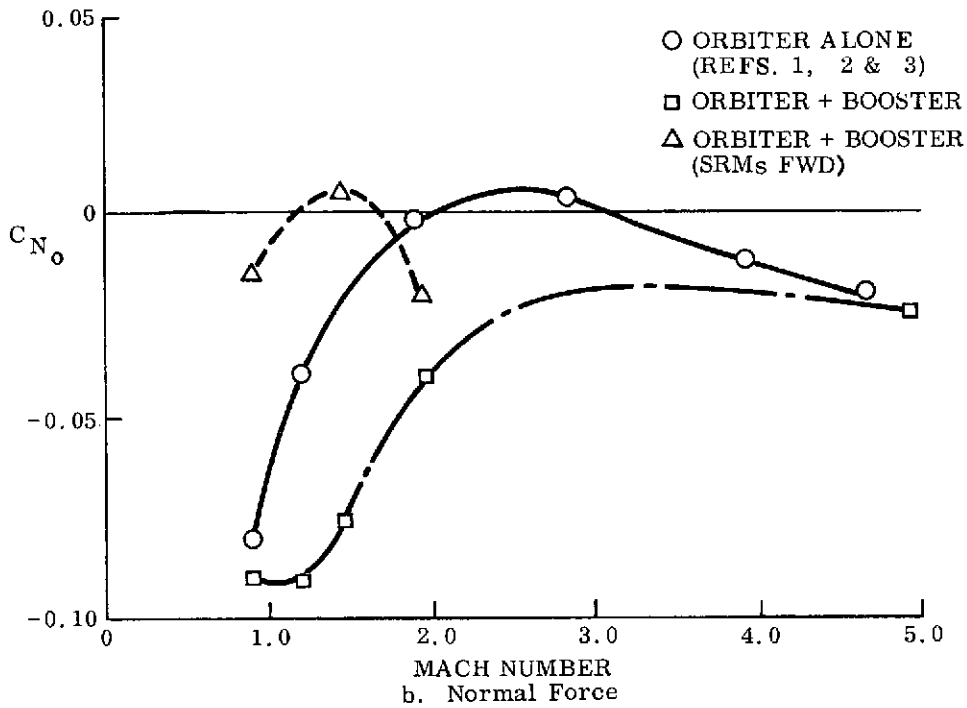


Figure 2. Effect of Booster Inteferece on Orbiter Loads at $\alpha = 0$, ATP Configuration (Sheet 2 of 2)

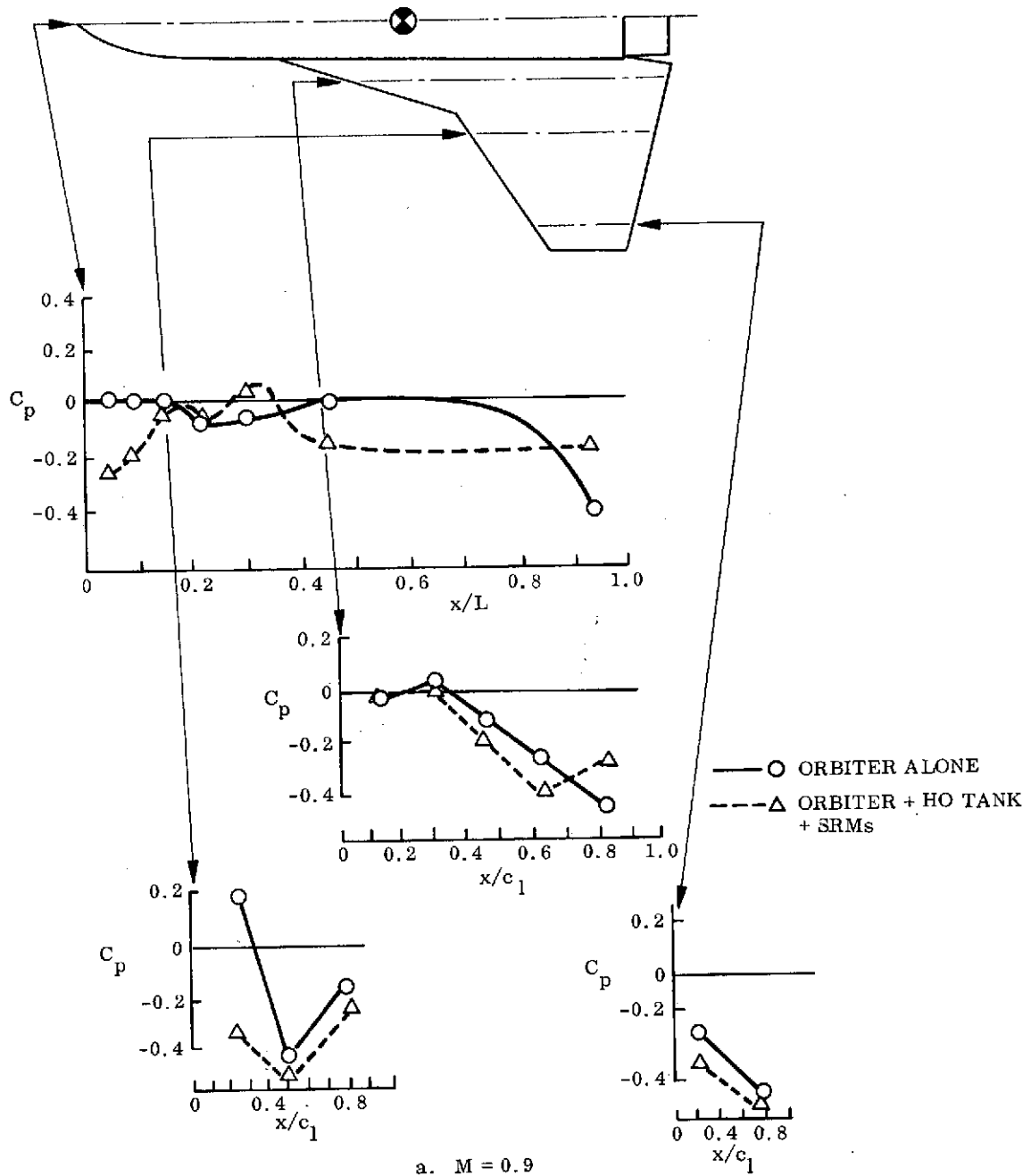


Figure 3. Effect of Booster Interference on 049 Orbiter Bottom-side Pressures (Ref. 3) (Sheet 1 of 4)

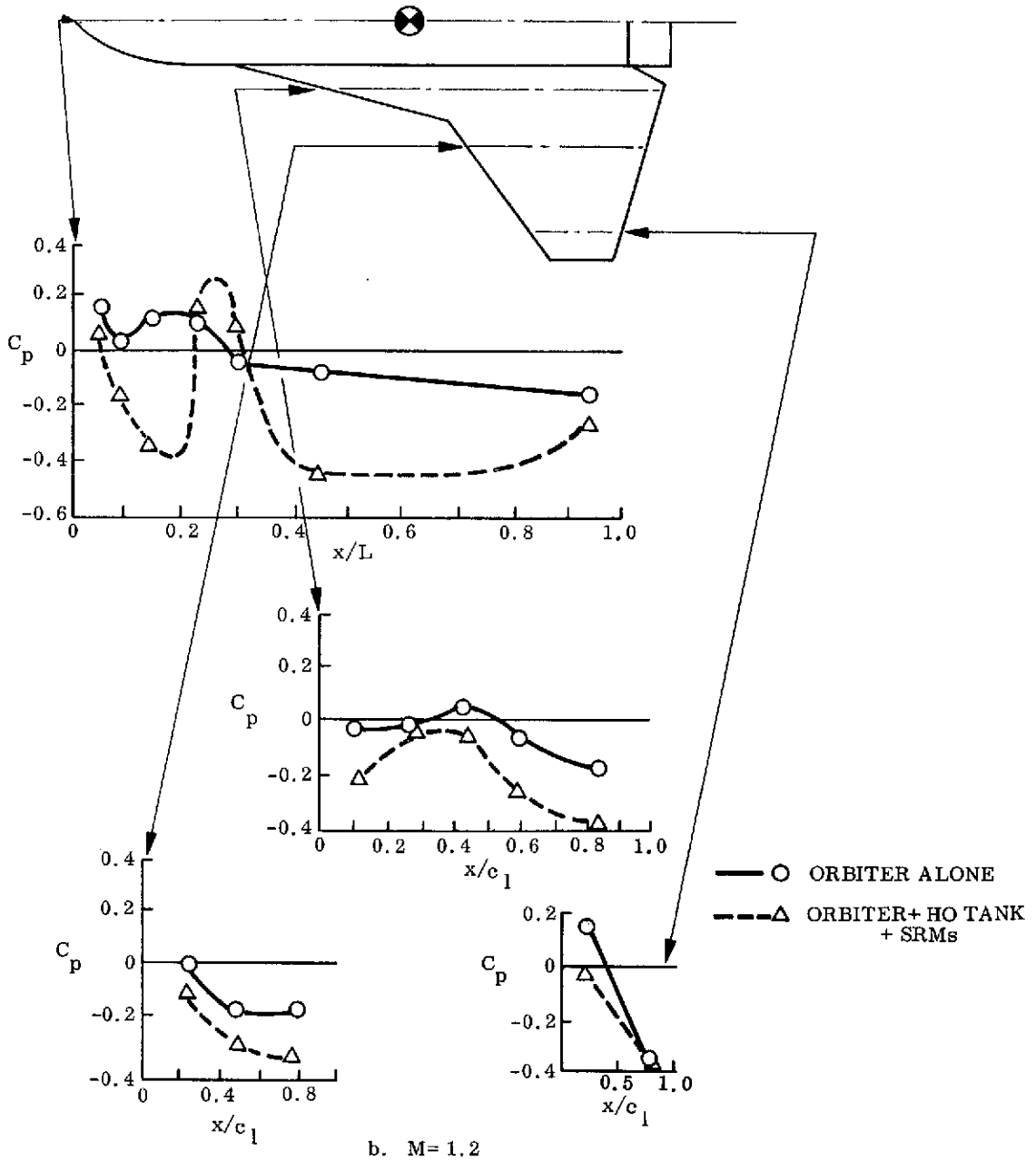
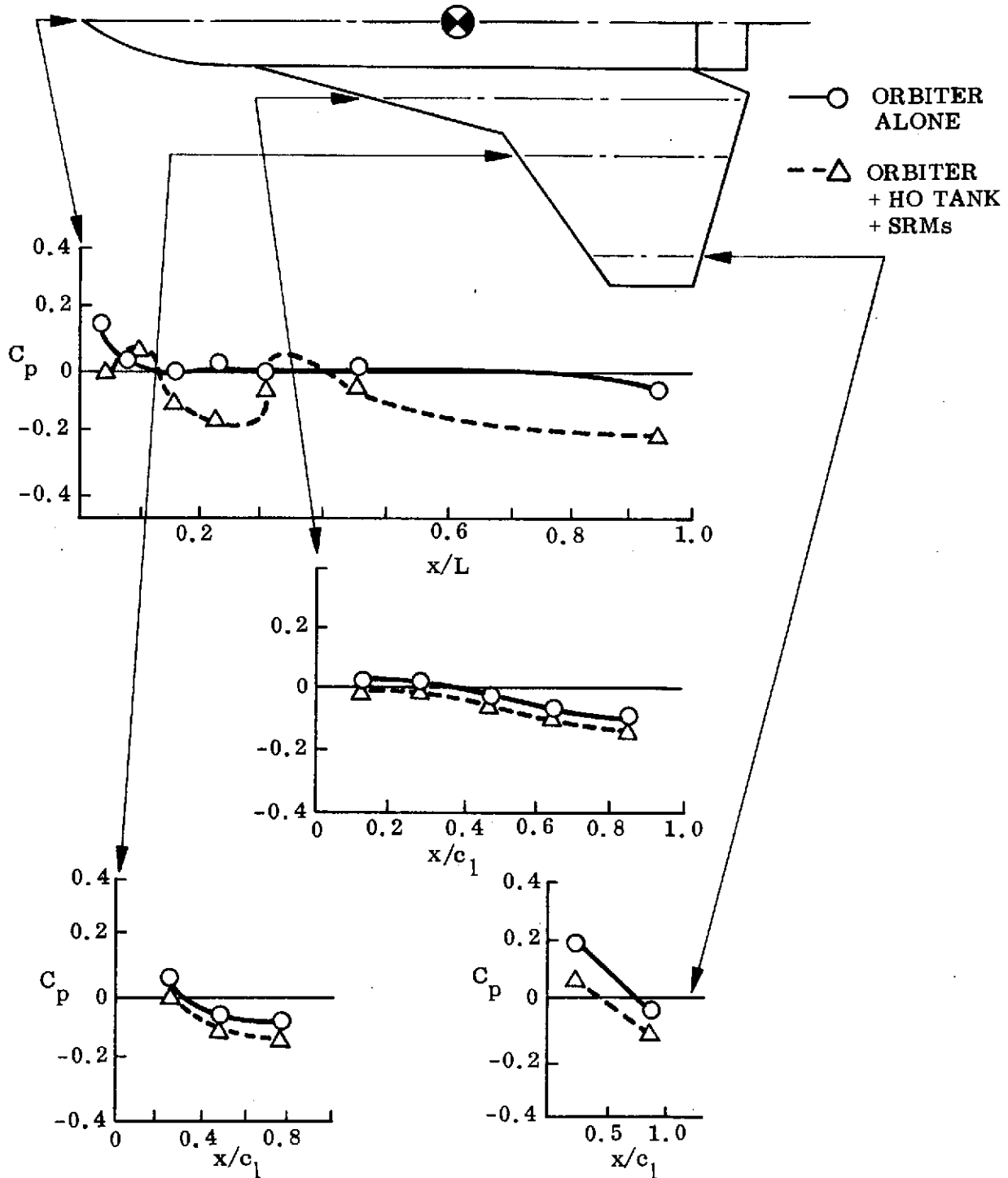
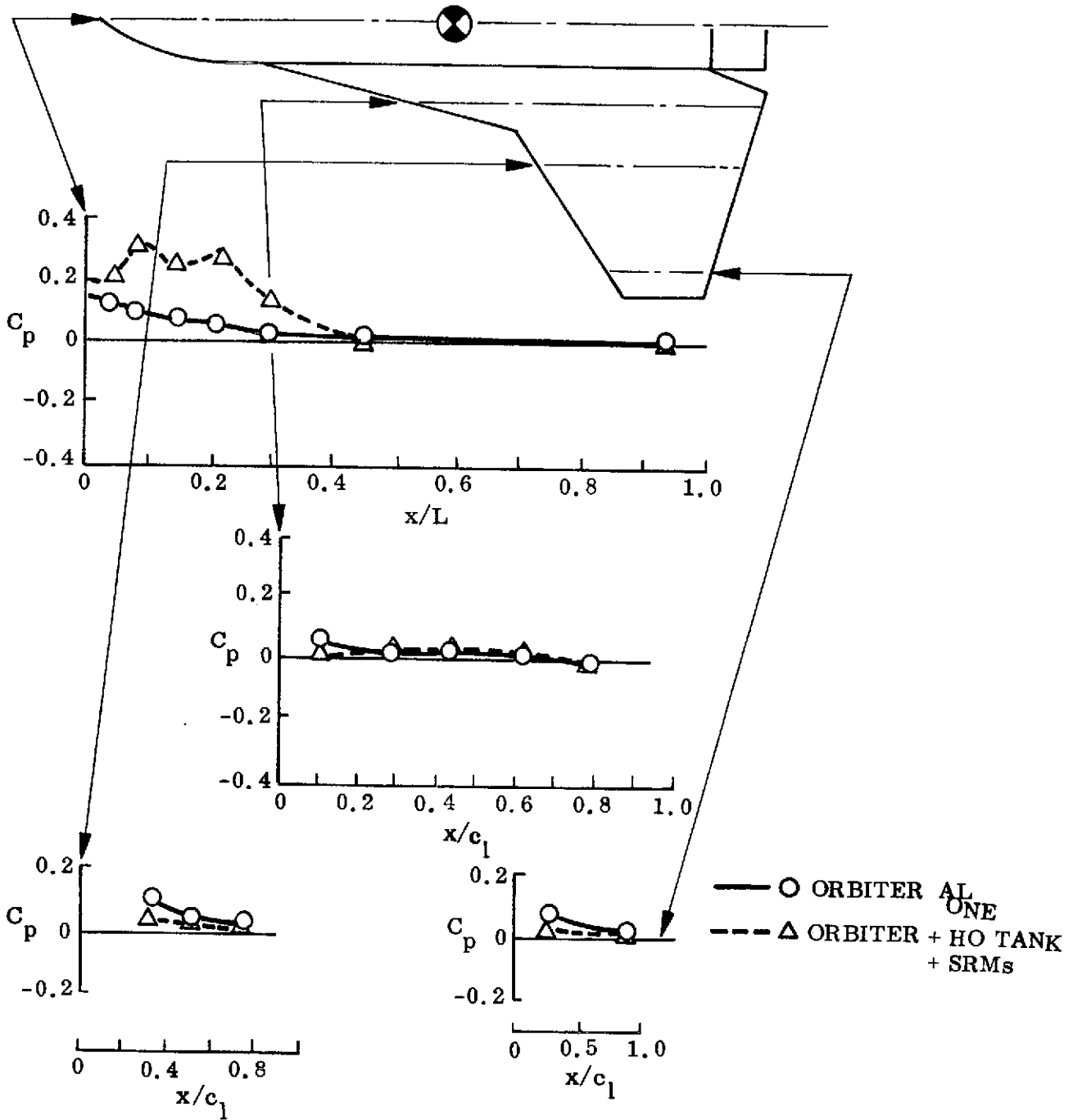


Figure 3. Effect of Booster Interference on 049 Orbiter Bottom-side Pressures (Ref. 3) (Sheet 2 of 4)



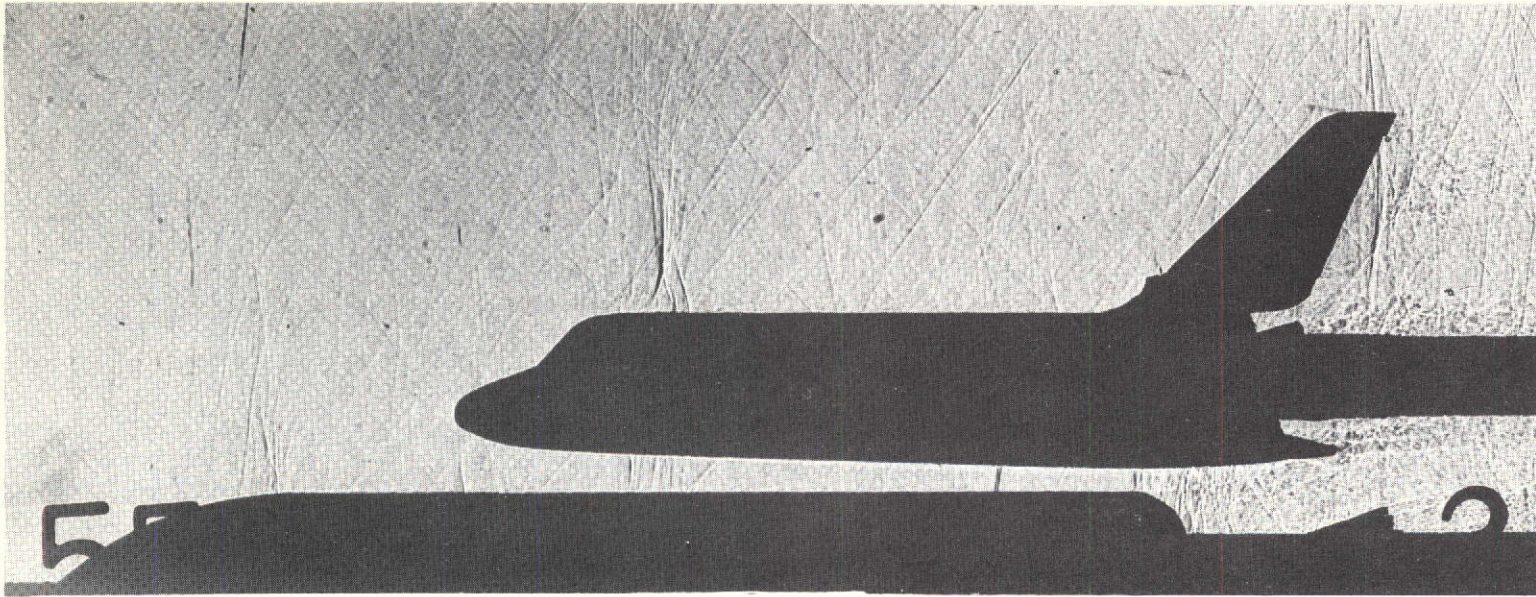
c. $M = 1.96$

Figure 3. Effect of Booster Interference on 049 Orbiter Bottom-side Pressures (Ref. 3) (Sheet 3 of 4)

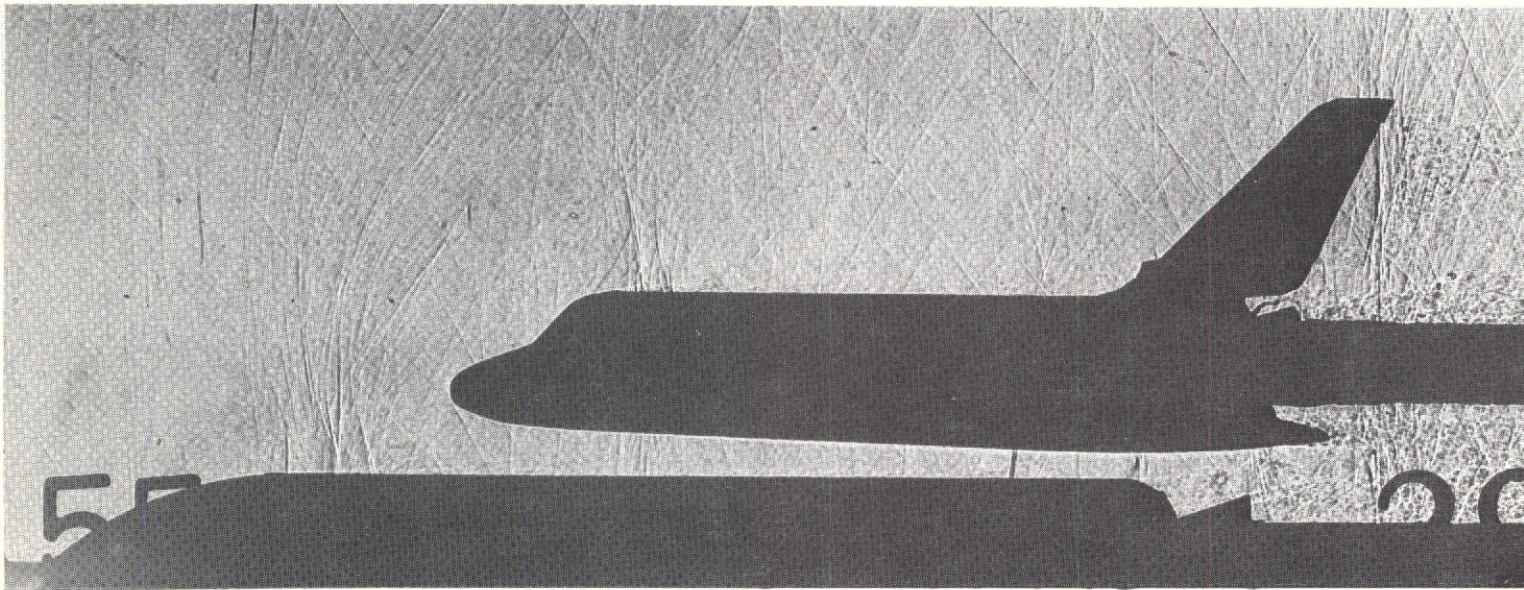


d. $M = 4.96$

Figure 3. Effect of Booster Interference on 049 Orbiter Bottom-side Pressures (Ref. 3) (Sheet 4 of 4)



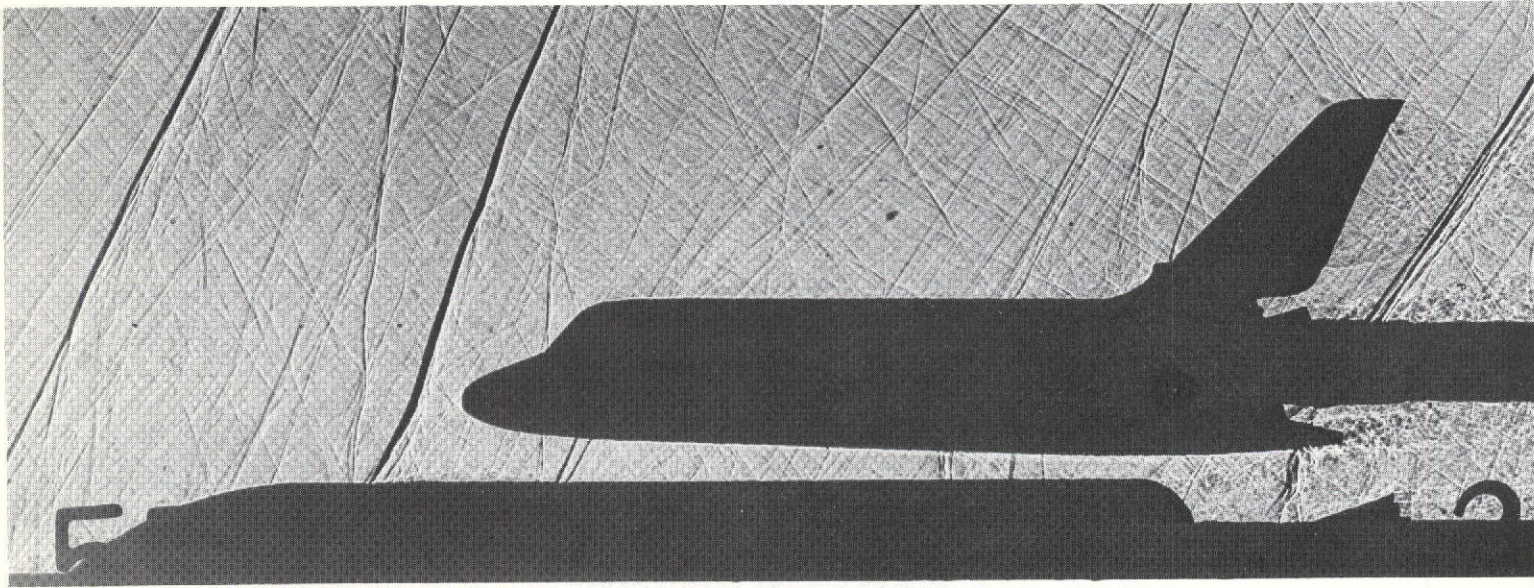
NORMAL SRM POSITION



FORWARD SRM POSITION

a. $M = 0.9$

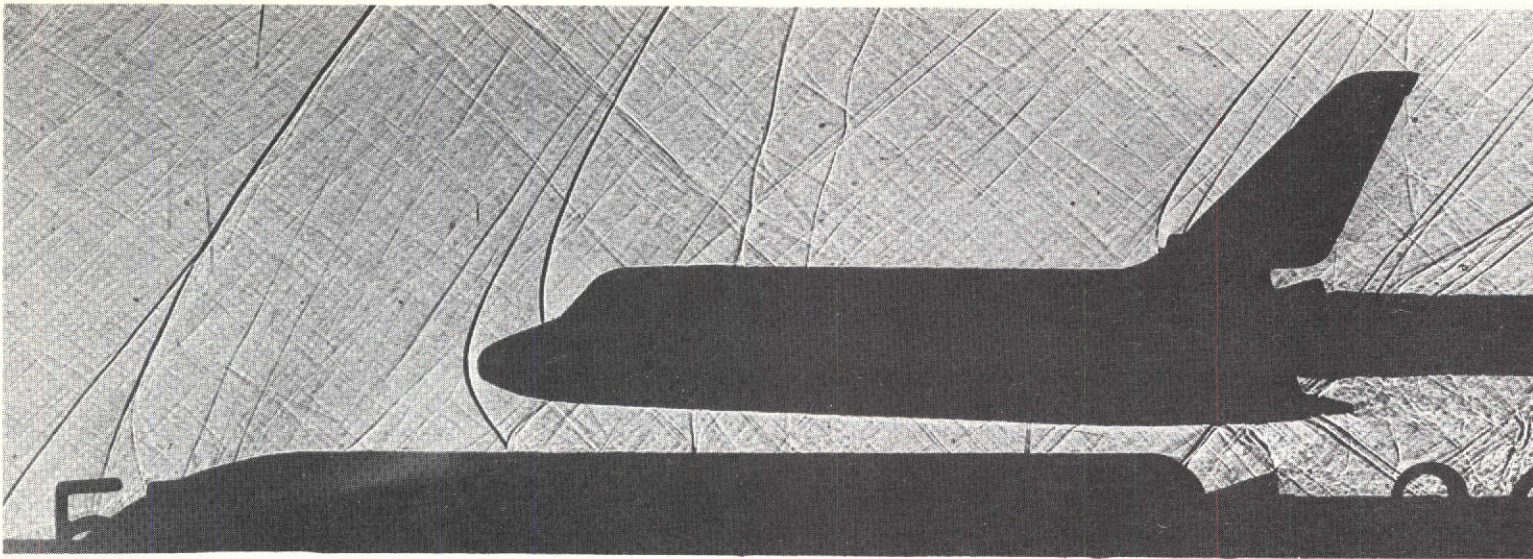
Figure 4. Shadowgraph Photographs of the ATP Booster at $\alpha = 0$
(Sheet 1 of 3)



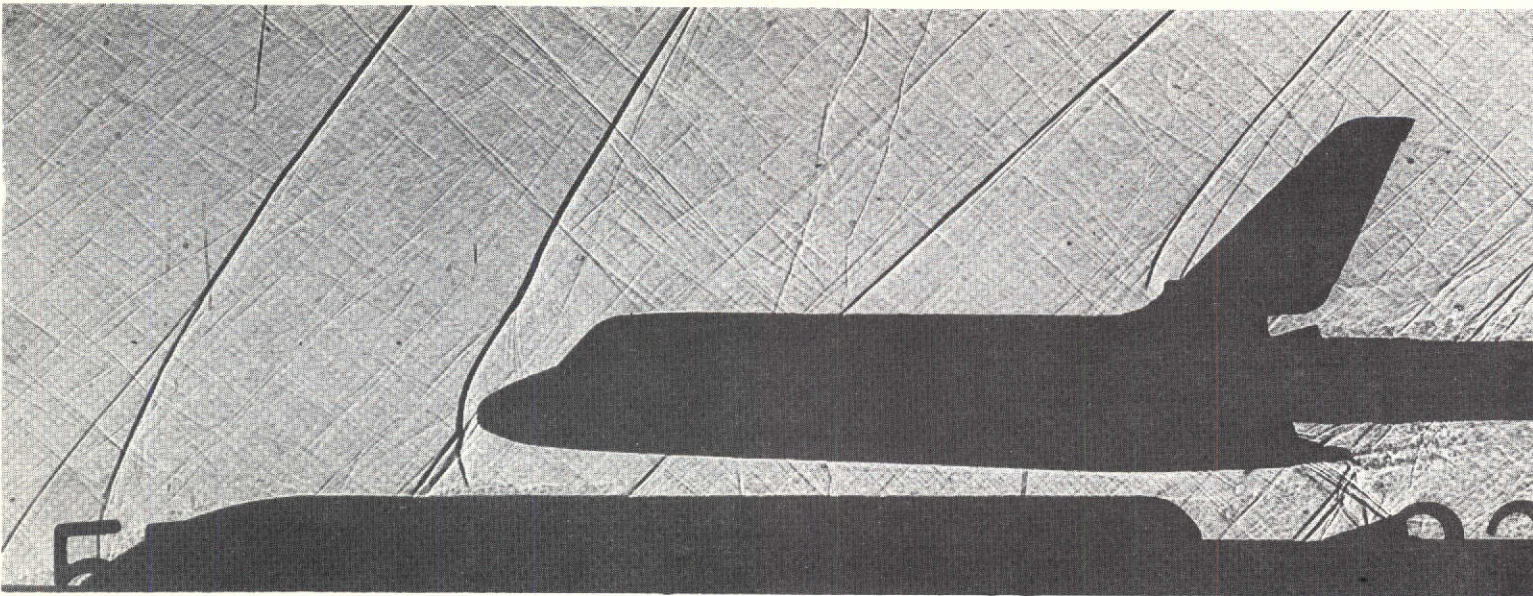
NORMAL SRM POSITION

b. $M = 1.2$

Figure 4. Shadowgraph Photographs of the ATP Booster at $\alpha = 0$
(Sheet 2 of 3)



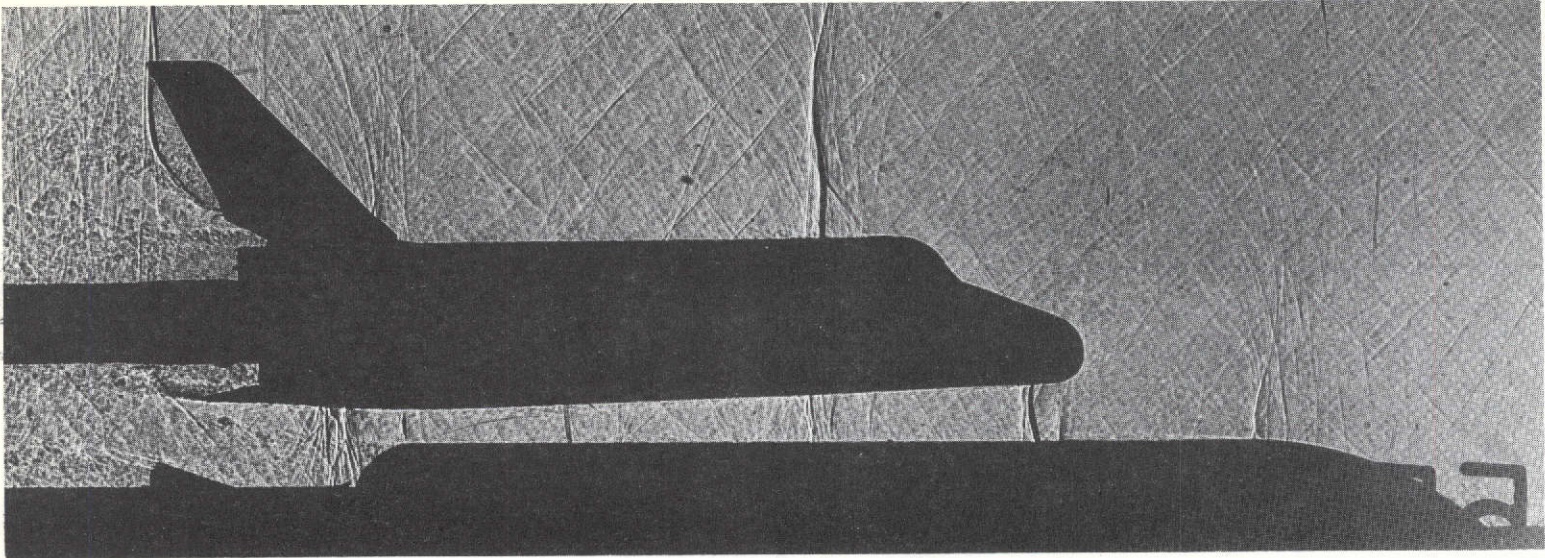
NORMAL SRM POSITION



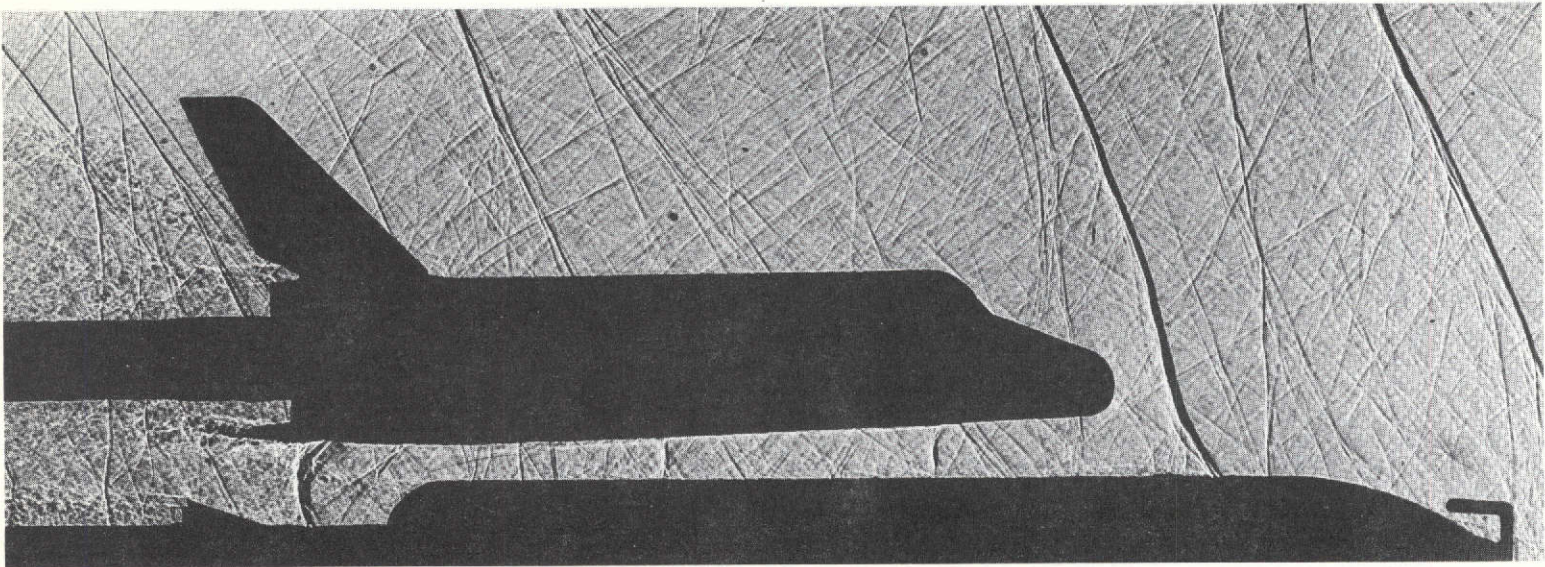
FORWARD SRM POSITION

c. $M = 1.46$

Figure 4. Shadowgraph Photographs of the ATP Booster at $\alpha = 0$
(Sheet 3 of 3)

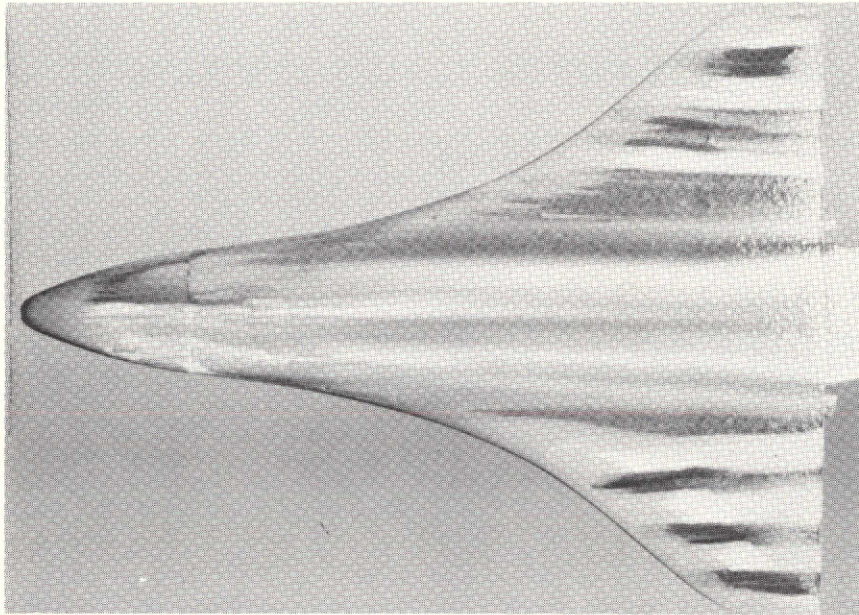


M = 0.9

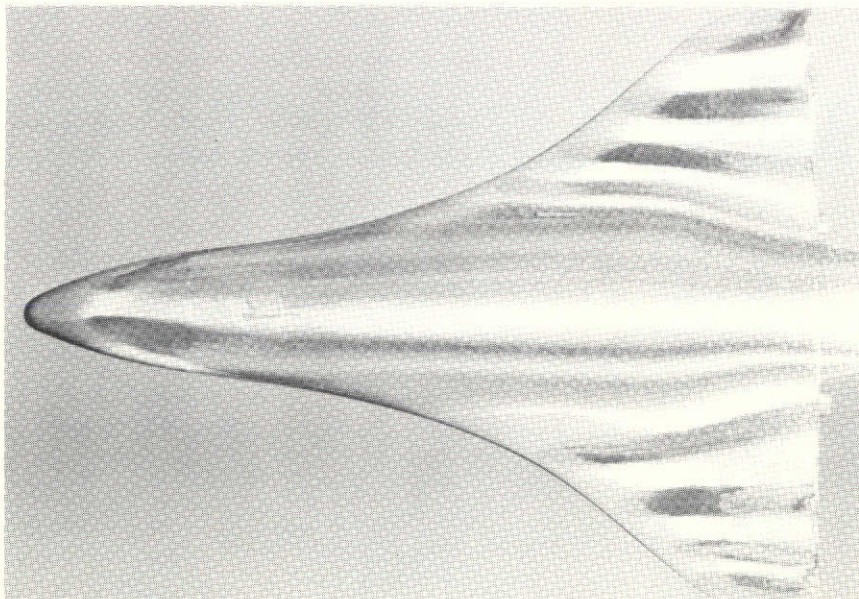


M = 1.2

Figure 5. Shadowgraph Photographs of the Current Boost Configuration at $\alpha = 0$



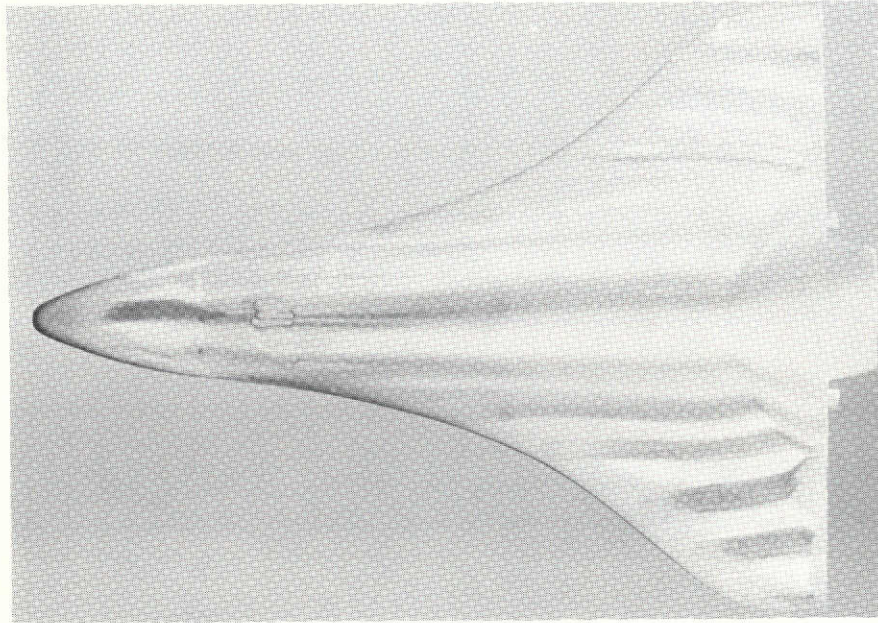
NORMAL SRM; $M = 0.9$



FORWARD SRM; $M = 0.9$

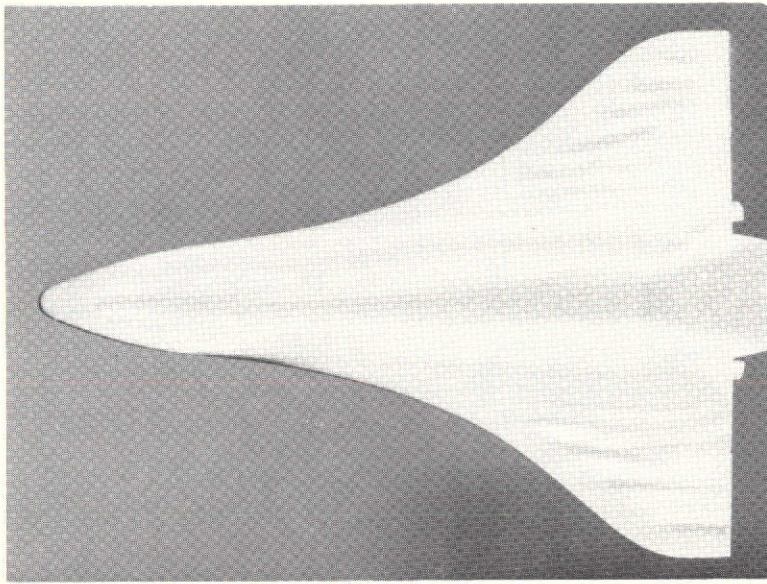
a. ATP CONFIGURATION

Figure 6. Effect of Booster Interference on Oilflow Patterns on the Bottom of the Orbiter, $\alpha = 0$, $\beta = 0$
(Sheet 1 of 4)

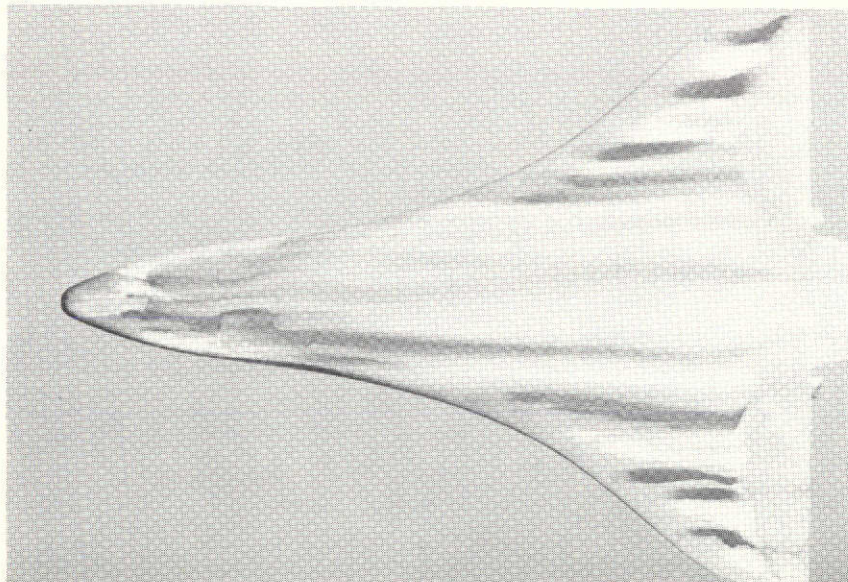


a. ATP CONFIGURATION (Continued)

Figure 6. Effect of Booster Interference on Oilflow Patterns on the Bottom
of the Orbiter, $\alpha = 0$, $\beta = 0$
(Sheet 2 of 4)



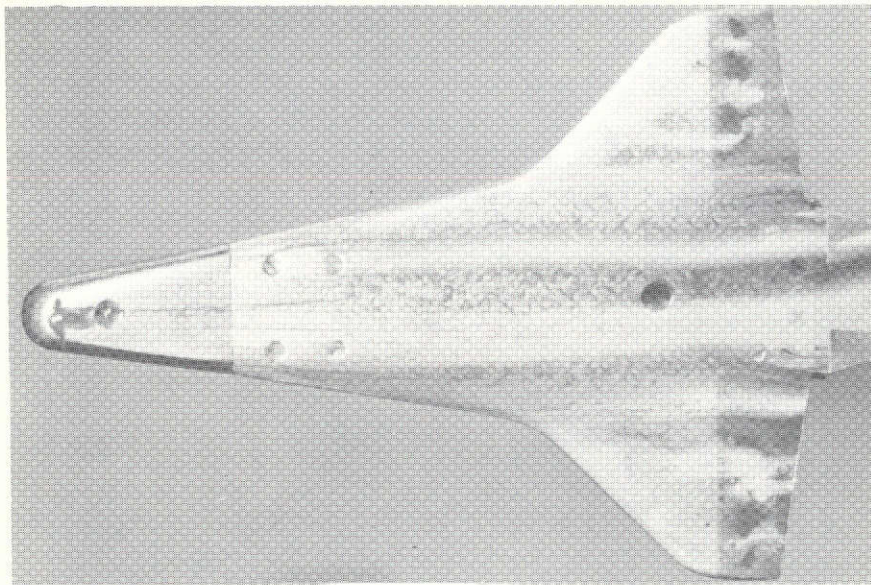
NORMAL SRM; $M = 1.46$



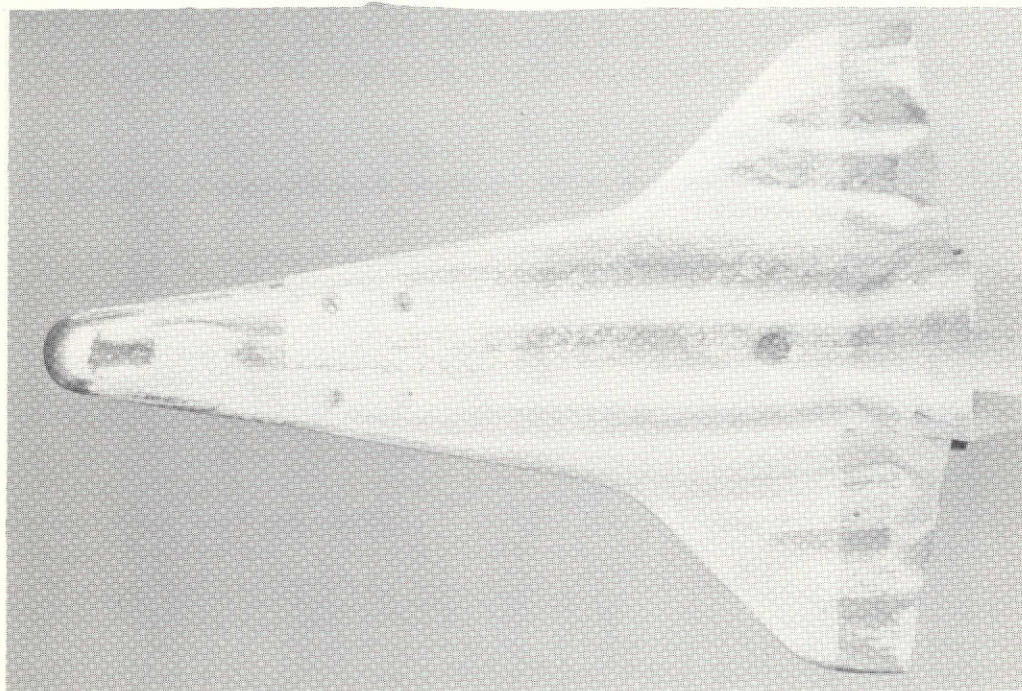
FORWARD SRM; $M = 1.46$

a. ATP CONFIGURATION (Continued)

Figure 6. Effect of Booster Interference on Oilflow Patterns on the Bottom of the Orbiter, $\alpha = 0$, $\beta = 0$
(Sheet 3 of 4)



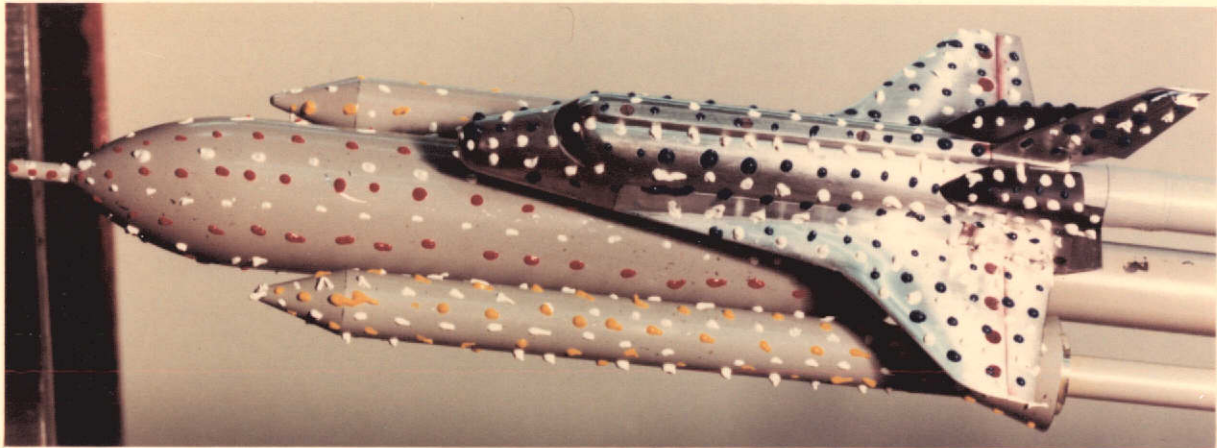
NORMAL SRM; $M = 0.9$



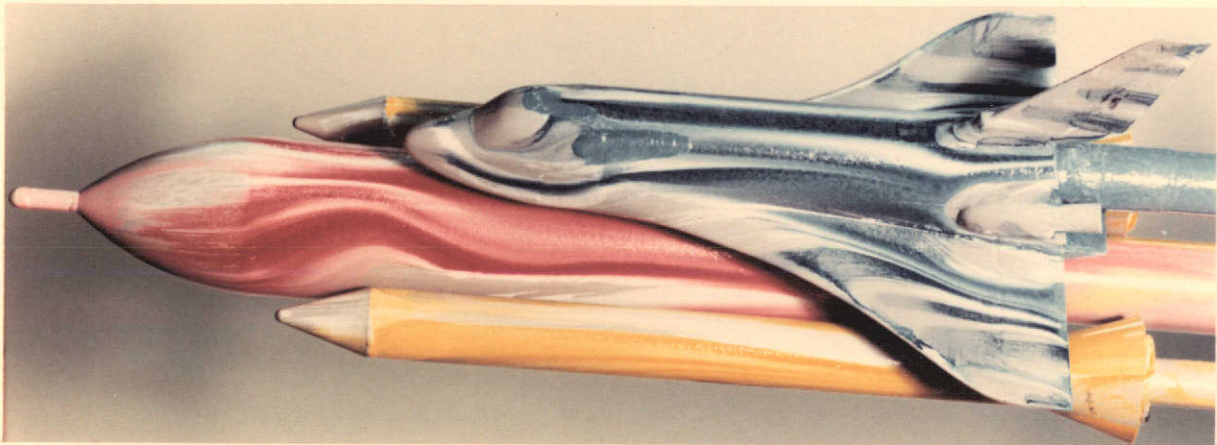
NORMAL SRM; $M = 1.2$

b. CURRENT CONFIGURATION

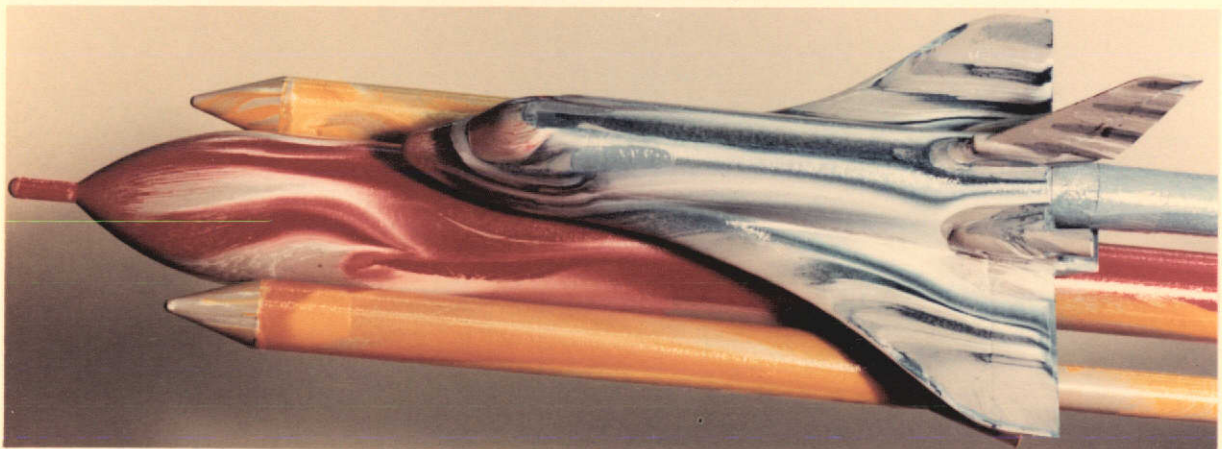
Figure 6. Effect of Booster Interference on Oilflow Patterns on the Bottom of the Orbiter, $\alpha = 0$, $\beta = 0$
(Sheet 4 of 4)



a. INITIAL OIL PATTERN

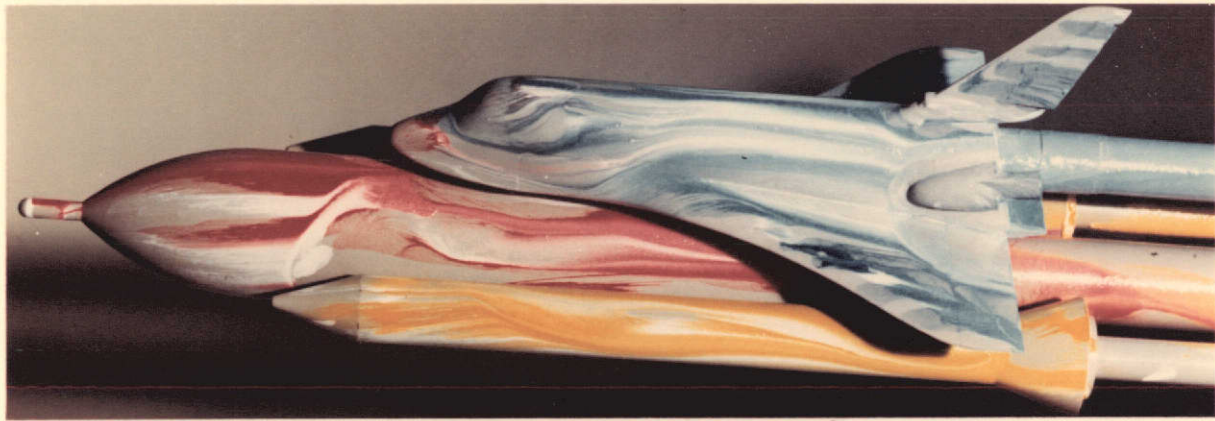


b. NORMAL SRM, $M = 0.9$, $\alpha = 5^\circ$

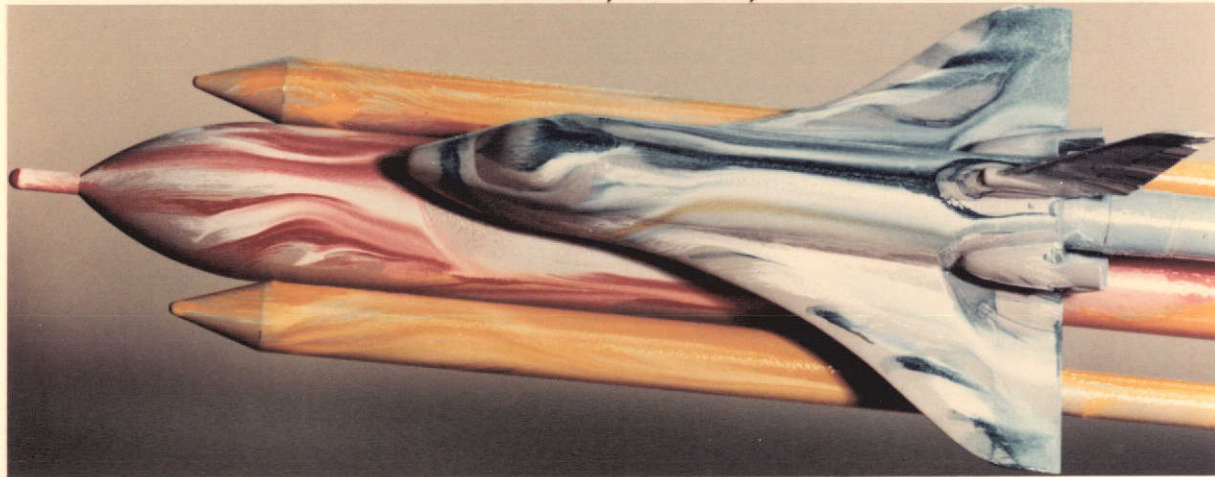


c. FORWARD SRM, $M = 0.9$, $\alpha = 5^\circ$

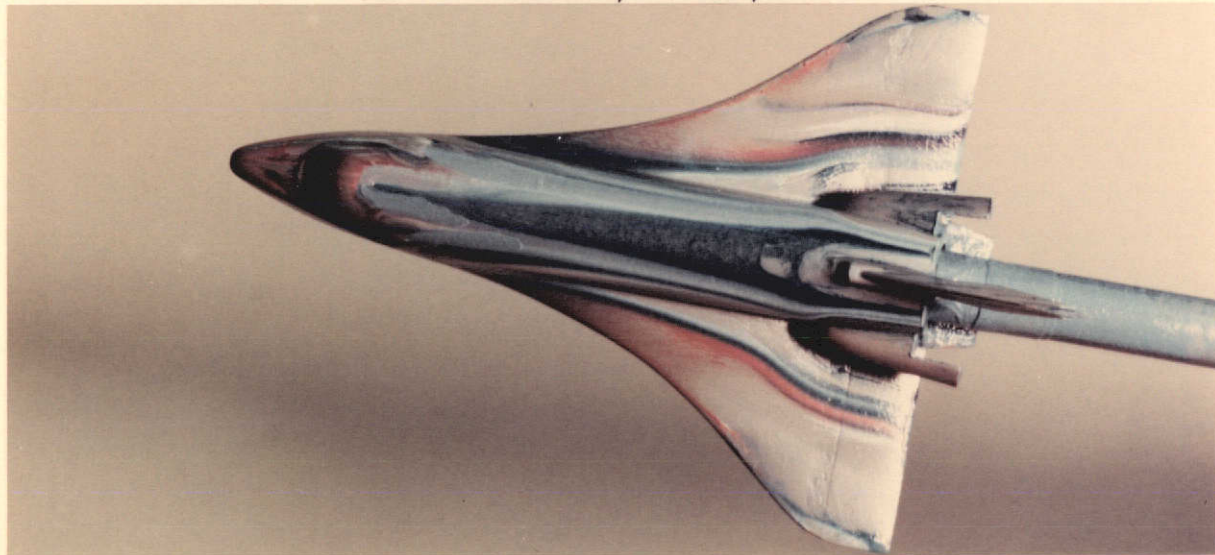
Figure 7. Interference Flow Field (Sheet 1 of 4)



d. NORMAL SRM, $M = 1.46$, $\alpha = 5^\circ$

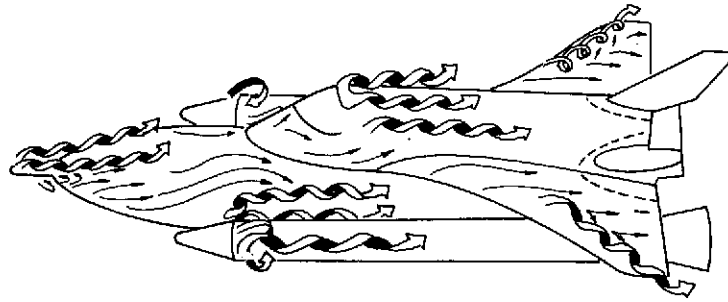


e. FORWARD SRM, $M = 1.46$, $\alpha = 5^\circ$

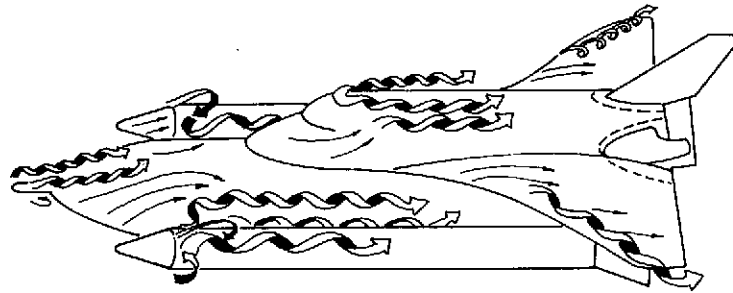


f. ORBITER TOP; FORWARD SRM, $M = 1.46$, $\alpha = 10^\circ$

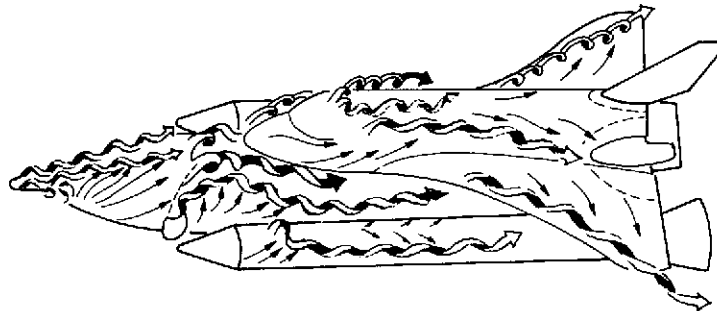
Figure 7. Interference Flow Field (Sheet 2 of 4)



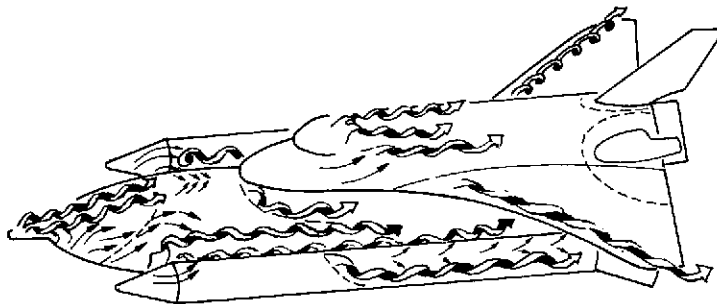
g. NORMAL SRM, $M = 0.9$



h. FORWARD SRM, $M = 0.9$

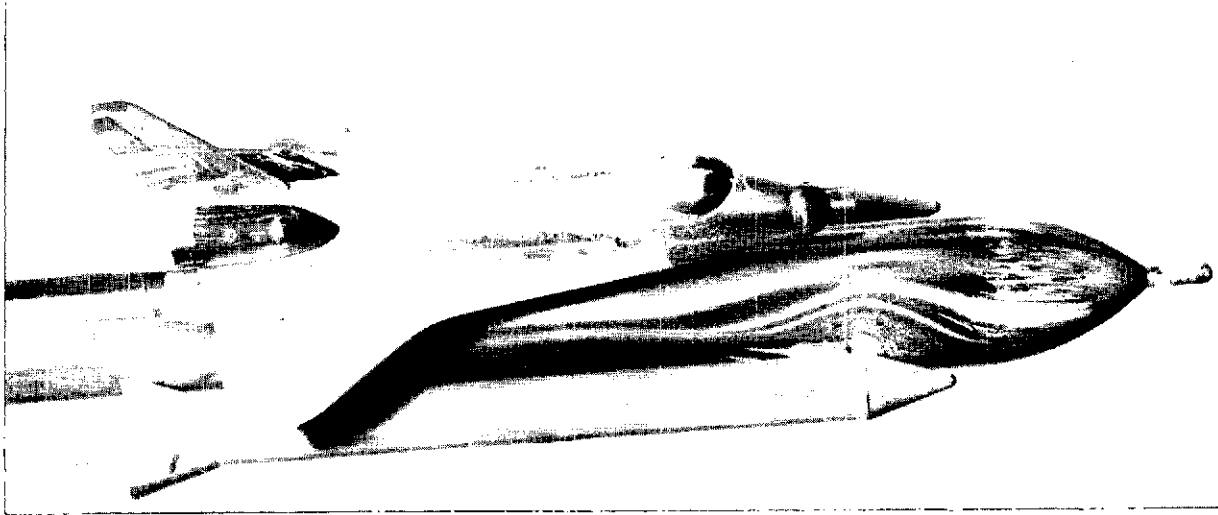


i. NORMAL SRM, $M = 1.46$



j. FORWARD SRM, $M = 1.46$

Figure 7. Interference Flow Field (Sheet 3 of 4)



k. $M = 0.9, \alpha = 0$



l. $M = 1.46, \alpha = 0$

Oilflow Results for Current Configuration

Figure 7. Interference Flow Field (Sheet 4 of 4)

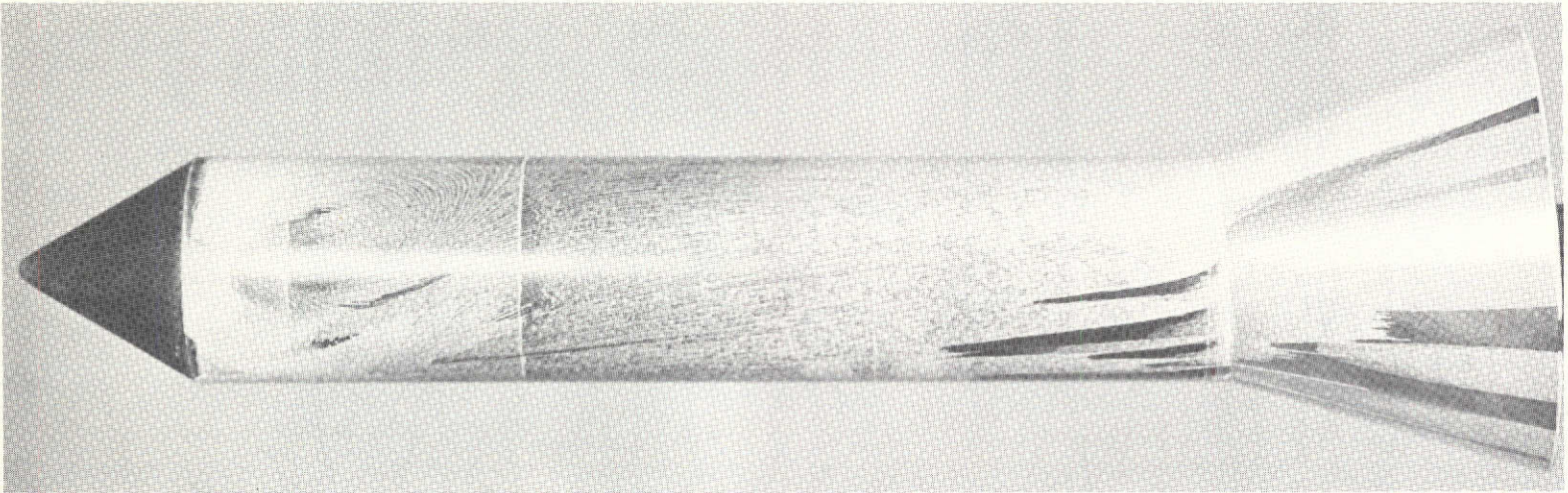


Figure 8. Typical Nose Induced Separation Flow Field $M = 0.9$ (Ref. 5)

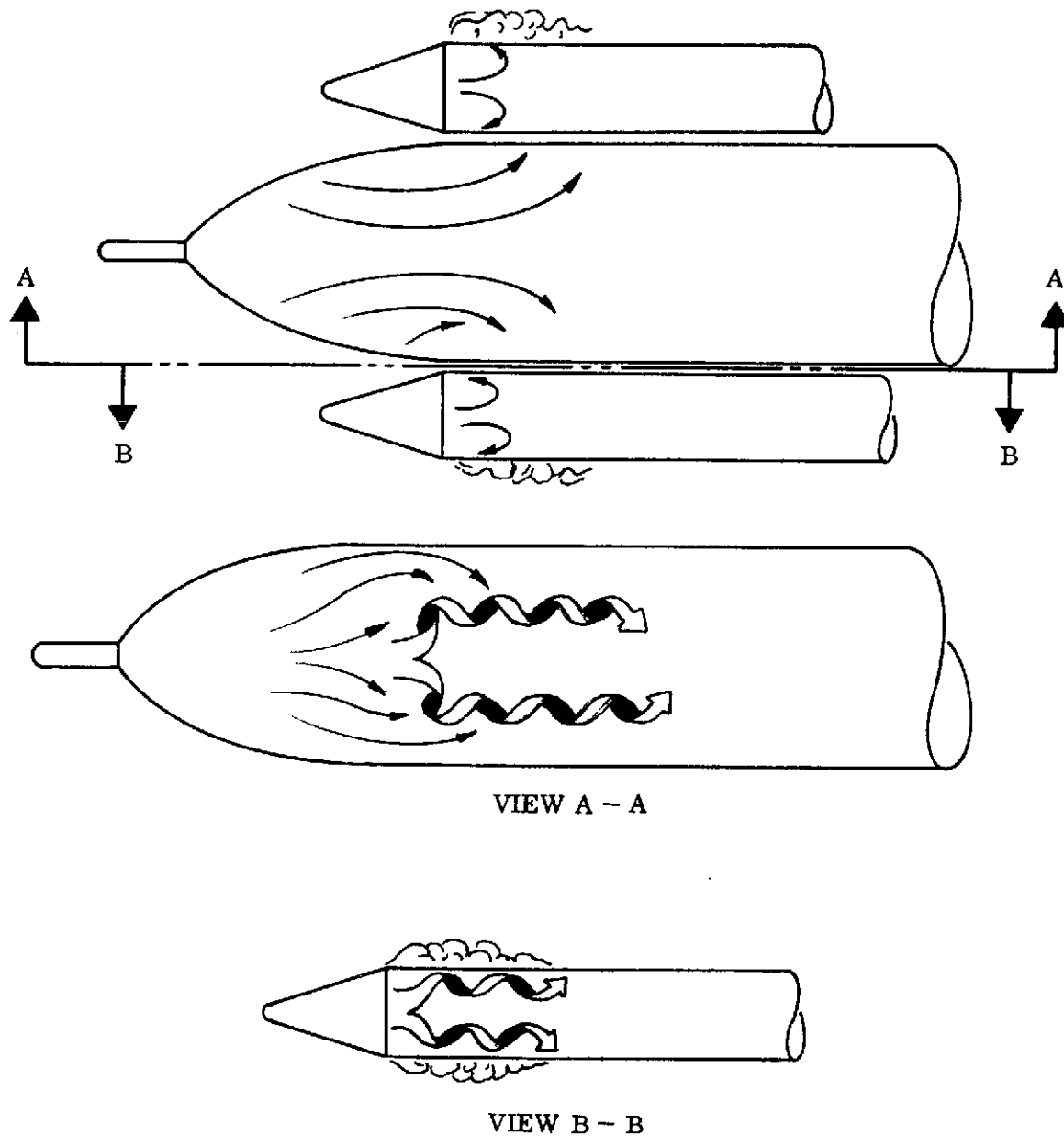
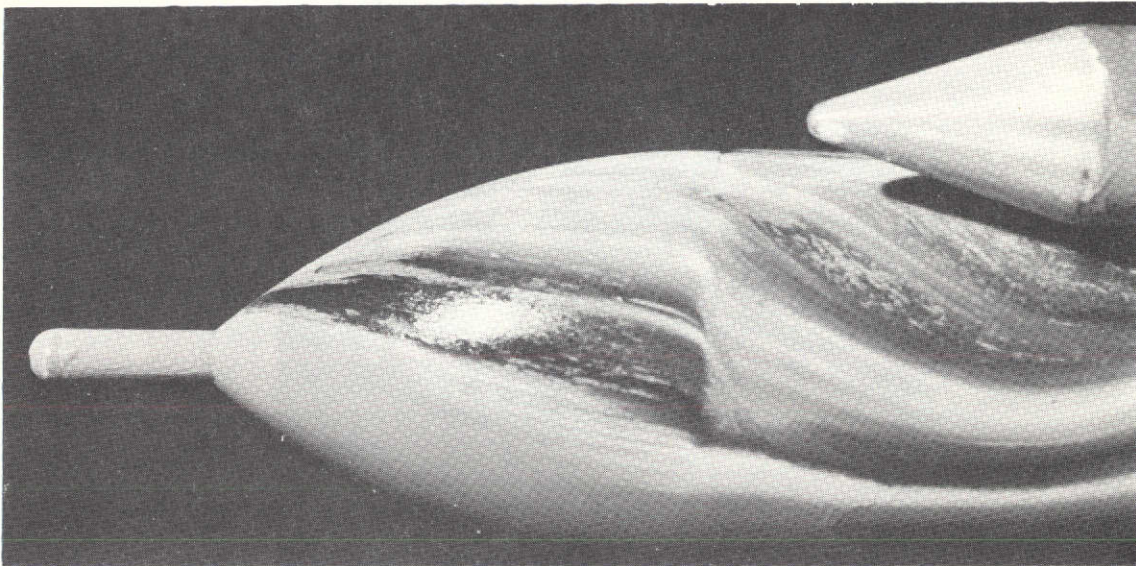
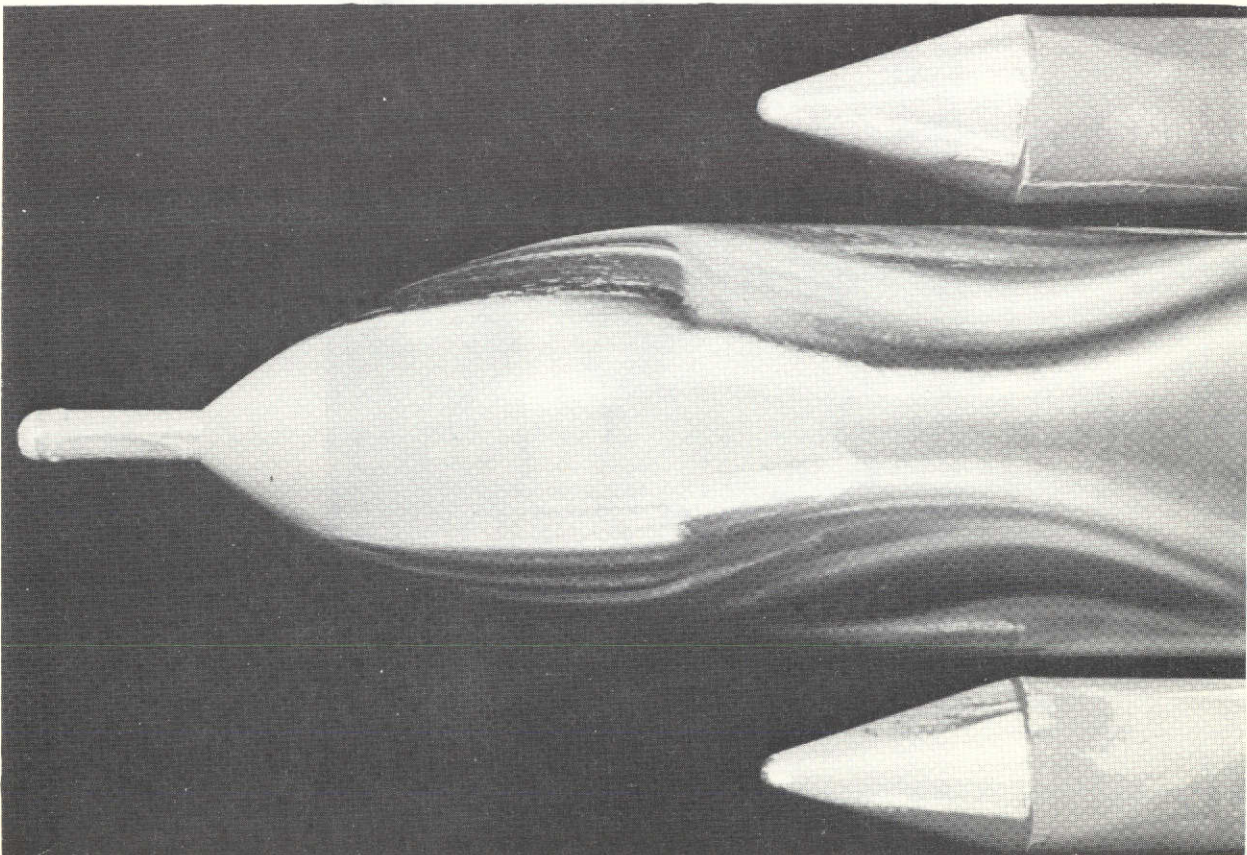


Figure 9. Flow Field Due to SRM-HO Tank Interference



THREE-QUARTER SIDE VIEW



TOP VIEW

Figure 10. Detail of Retro-rocket, Spike-induced, Separated Flow Region
 $M = 0.9, \alpha = 10^\circ$

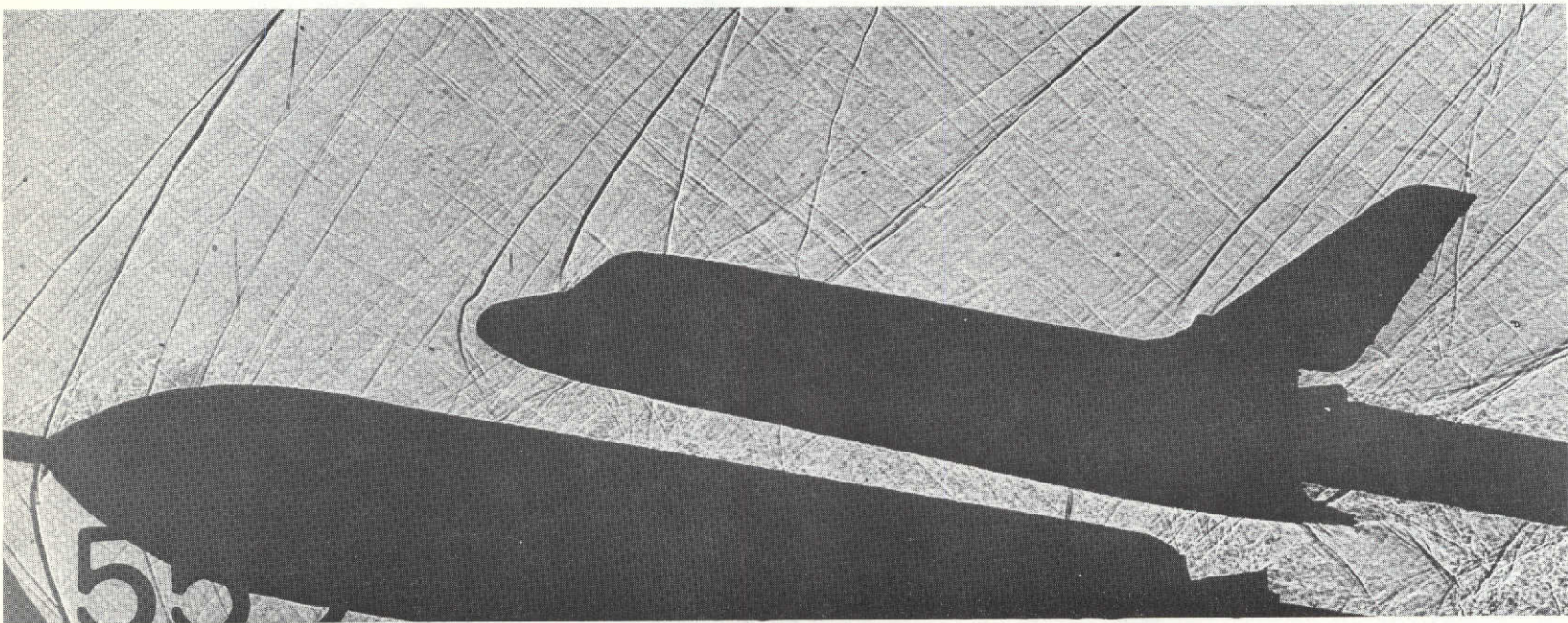
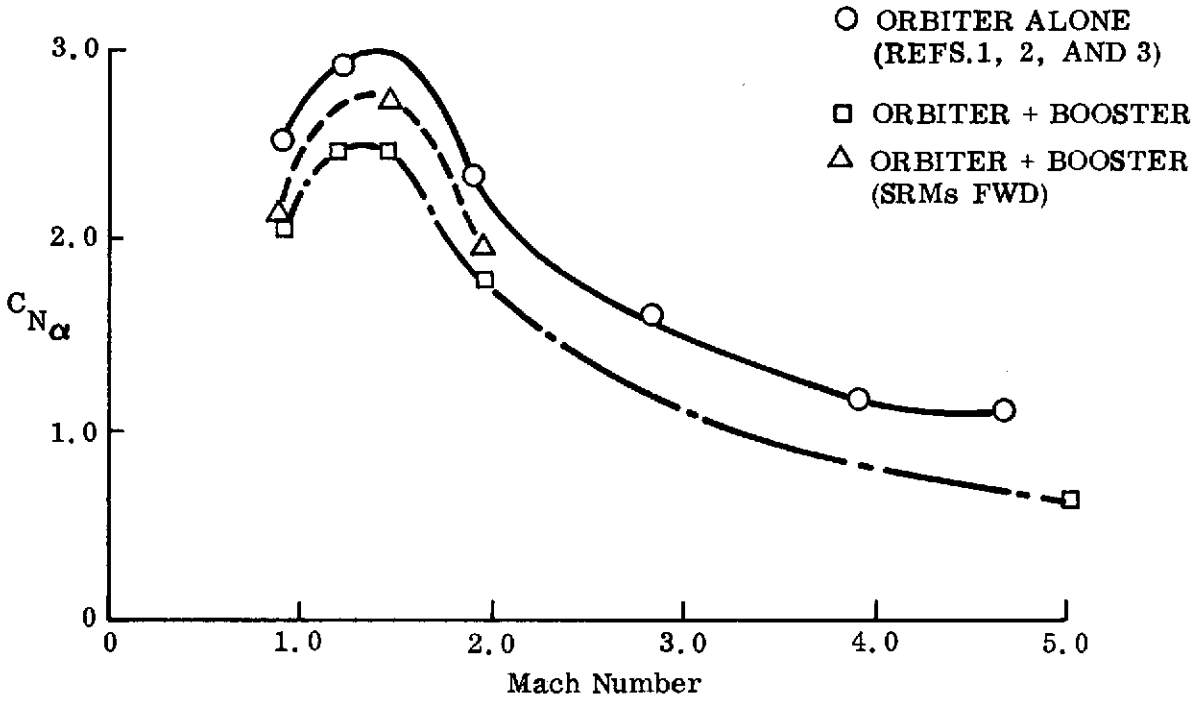
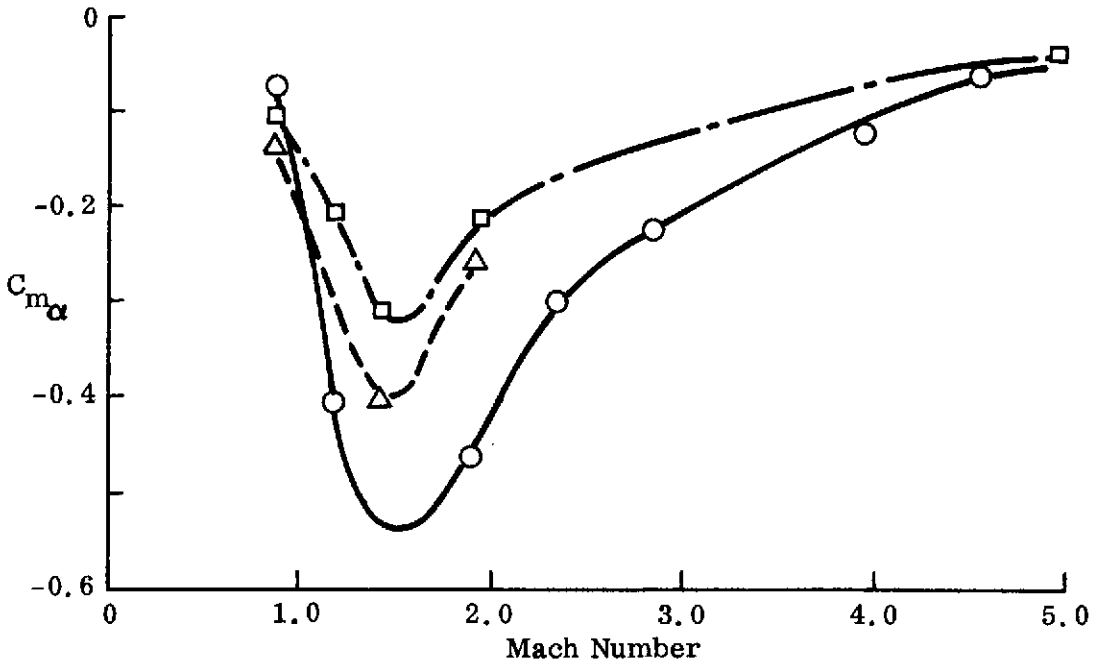


Figure 11. Effect of Retro-rocket Spike-induced Separation on Orbiter Bow Shock, $M = 1.46$, $\alpha = 10^\circ$

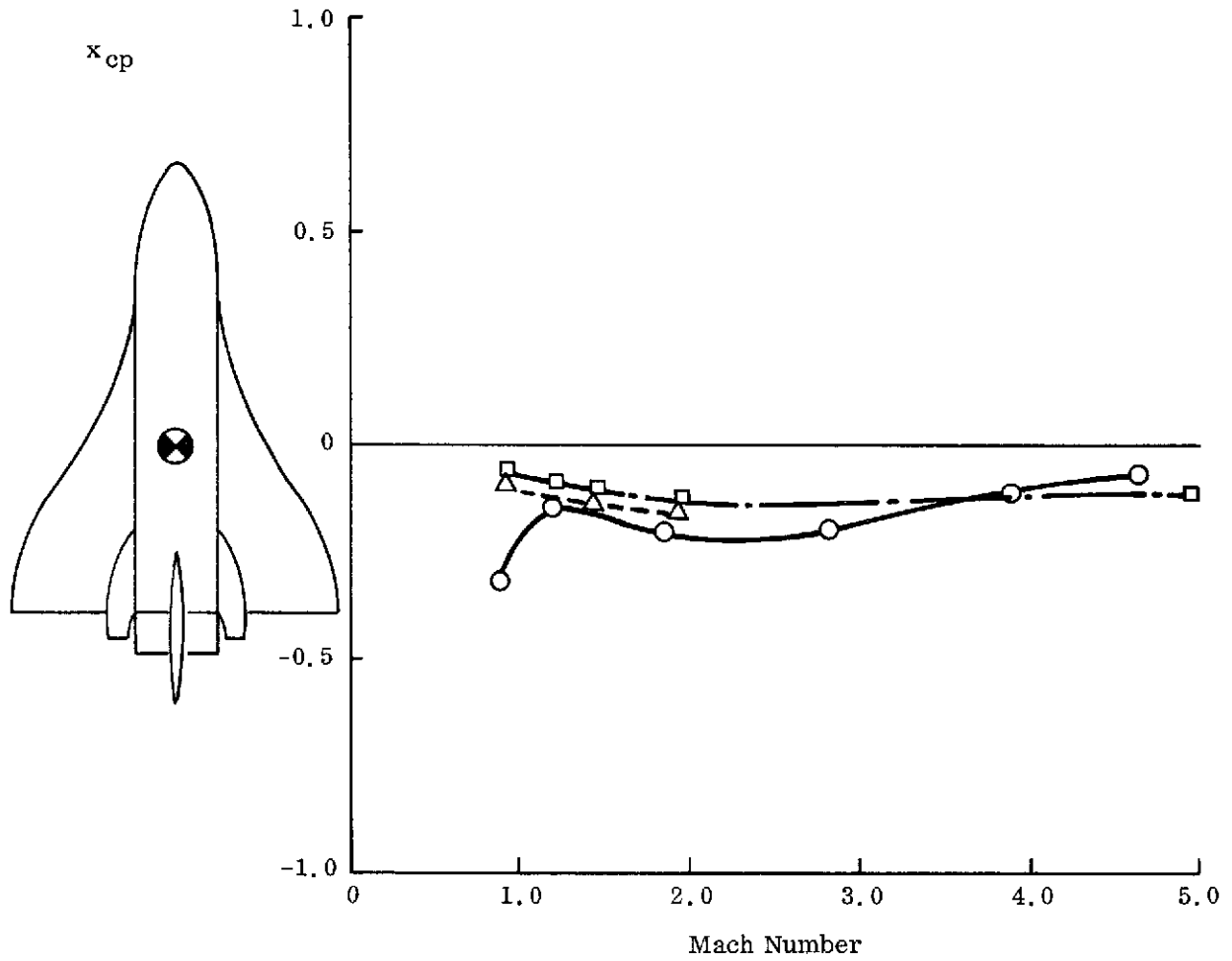


a. Normal Force Derivative



b. Pitching Moment Derivative

Figure 12. Effect of Booster Interference on Orbiter Stability at $\alpha = 0$, ATP Configuration (Sheet 1 of 2)



c. Center of Pressure

Figure 12. Effect of Booster Interference on Orbiter Stability at $\alpha = 0$, ATP Configuration (Sheet 2 of 2)

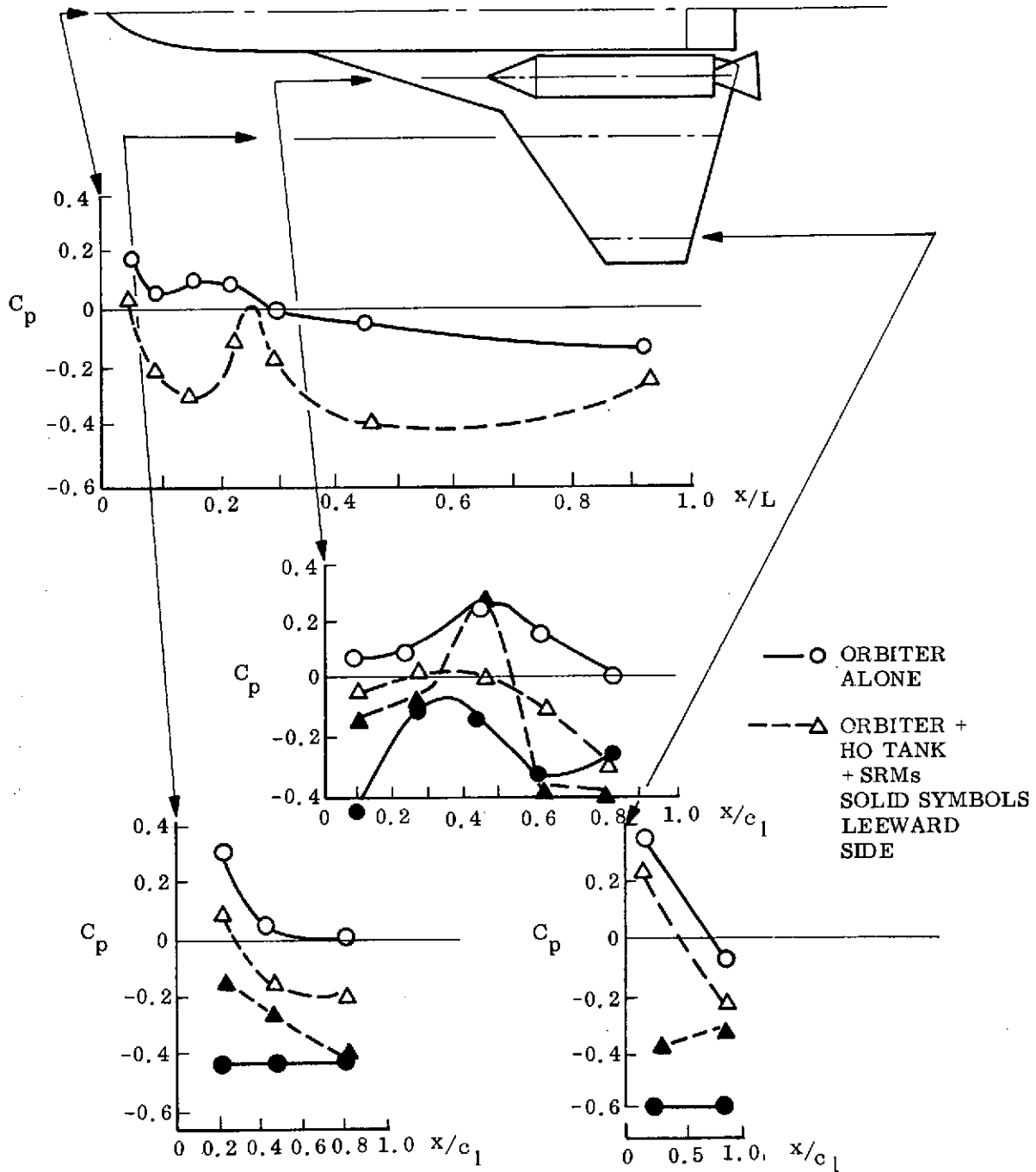
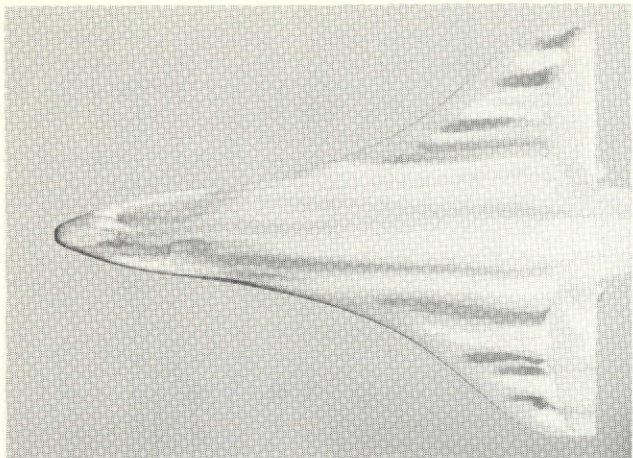
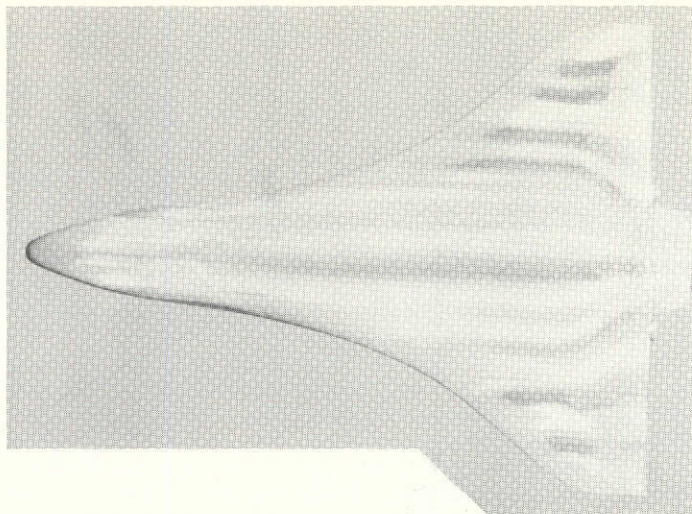


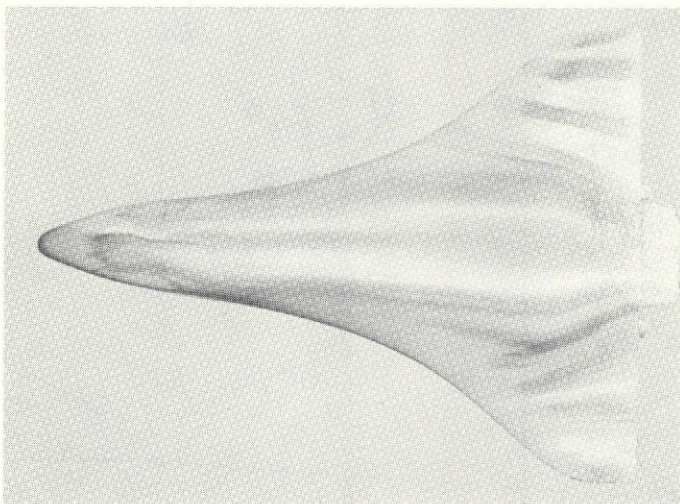
Figure 13. Effect of Booster Interference on Orbiter Bottom-Side Pressures at $\alpha = 6^\circ$, 049 Configuration (Ref. 3)



a. $\alpha = 0$



b. $\alpha = 5^\circ$



c. $\alpha = 10^\circ$

Figure 14. Effect of Angle of Attack on Interference Flow Field, ATP Booster with Forward SRMs, $M = 1.46$

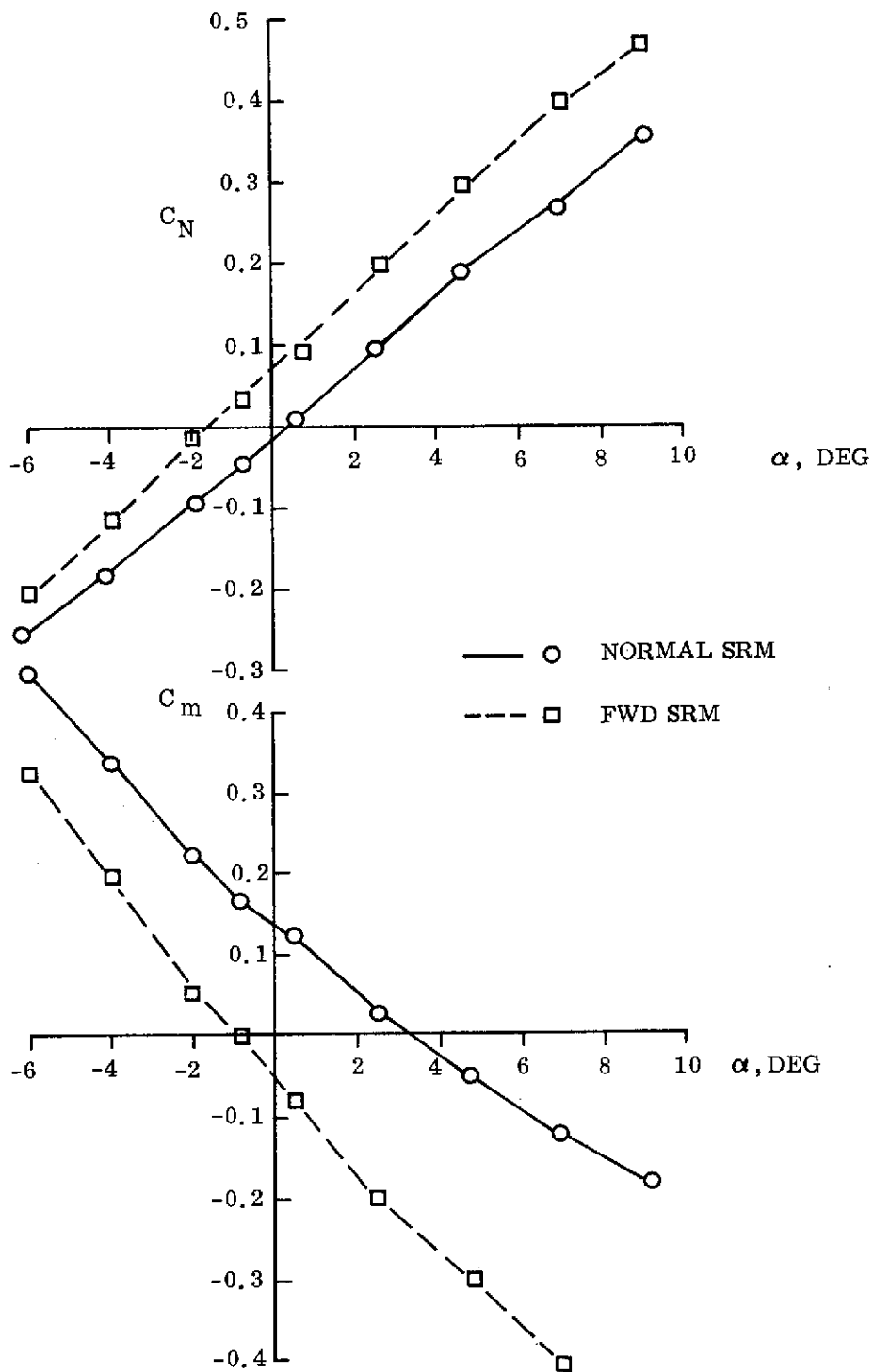
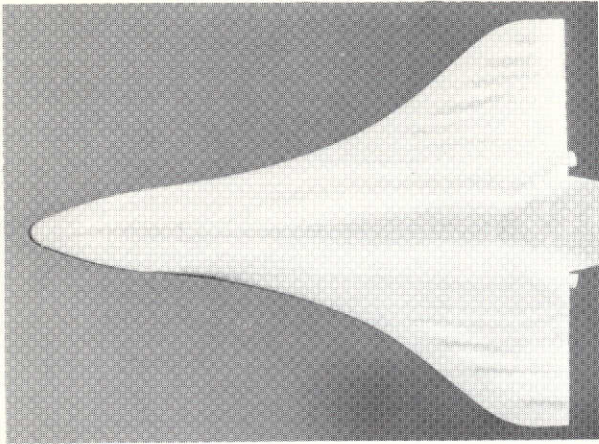
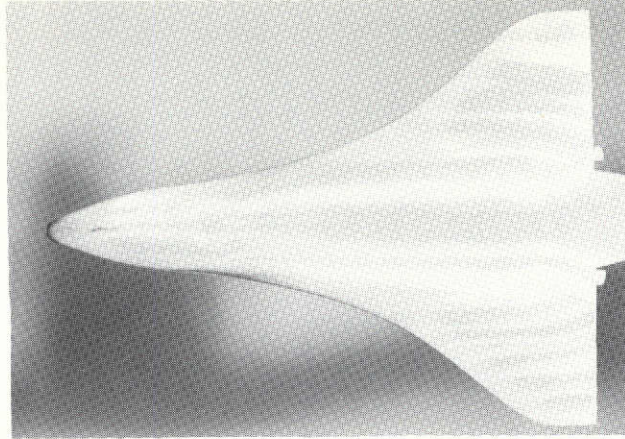


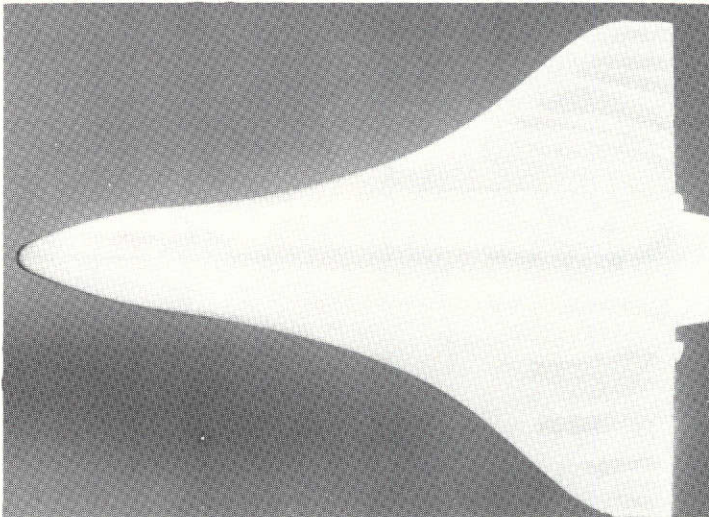
Figure 15. Comparison of Orbiter Pitch Characteristics for Two SRM Positions, ATP Booster, M = 1.46



a. $\alpha = 0$

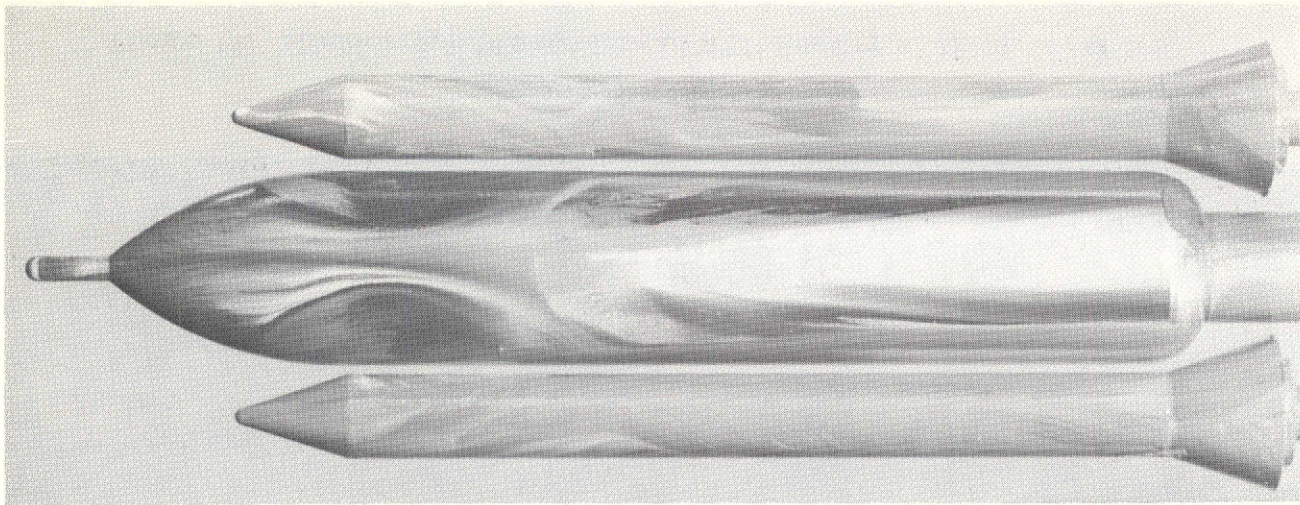


b. $\alpha = 5^\circ$

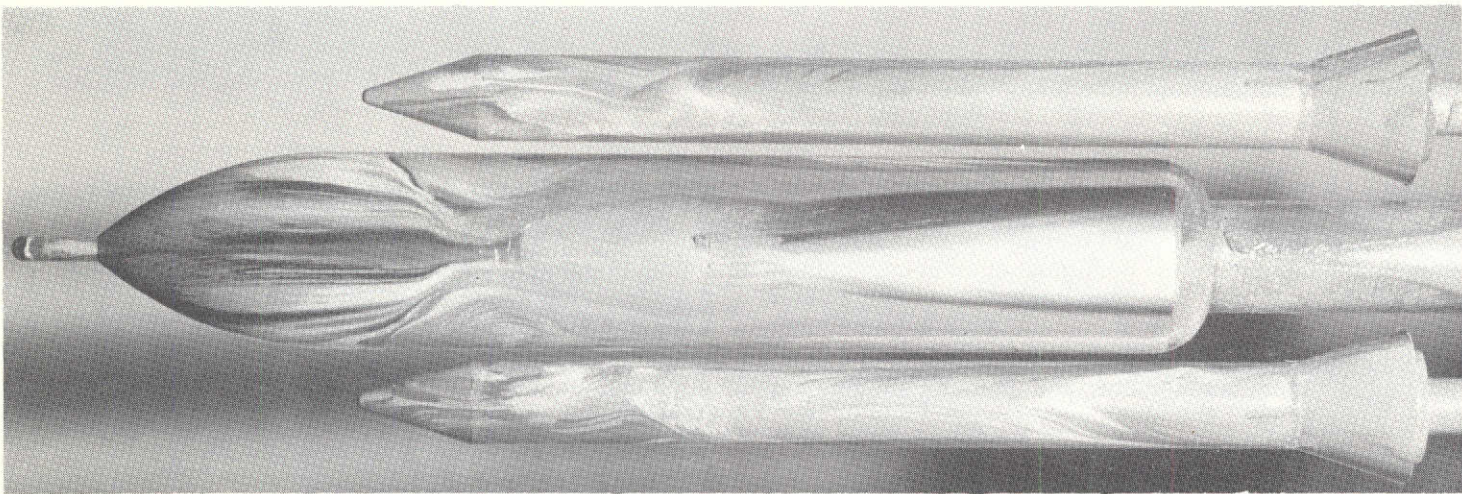


c. $\alpha = 10^\circ$

Figure 16. Effect of Angle of Attack on the Orbiter Bottom-side Oilflow Patterns, ATP Configuration with Normal SRM Position, $M = 1.46$

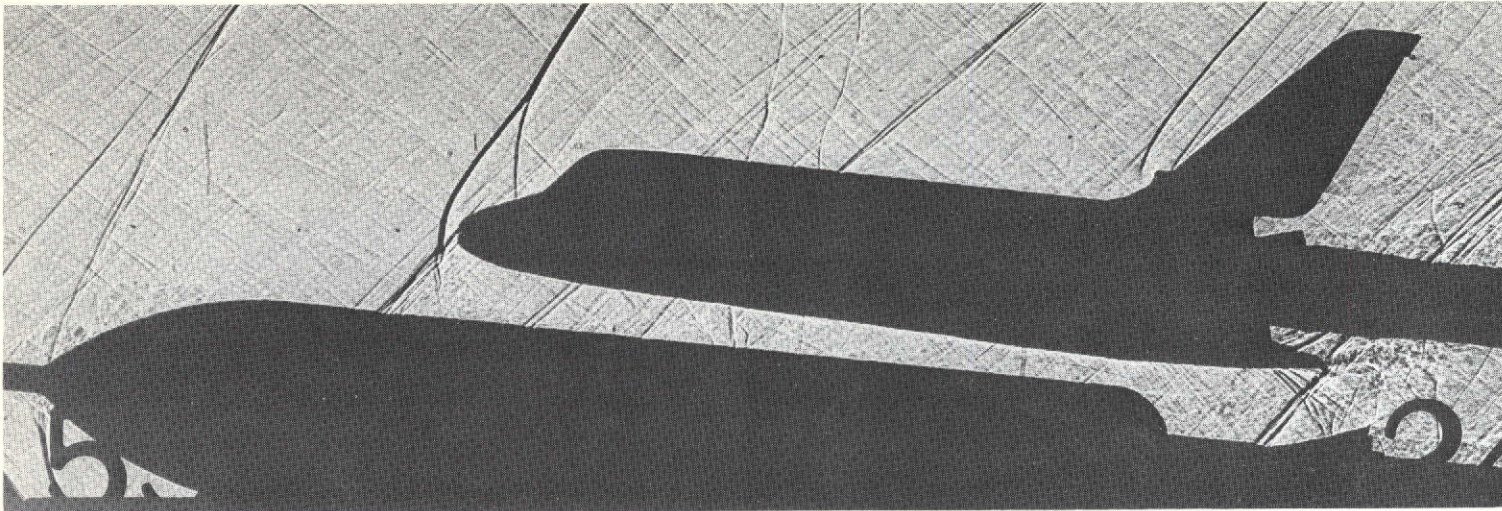


a. FORWARD SRM

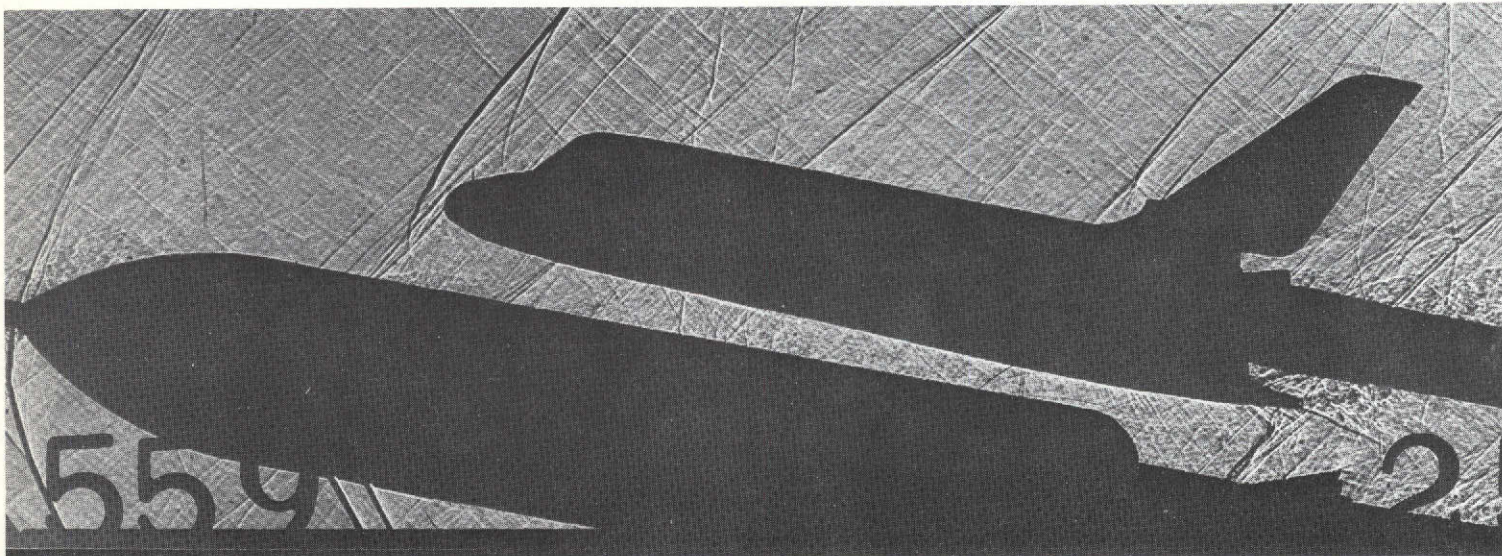


b. NORMAL SRM

Figure 17. Leeside Interference Flow Patterns on the ATP Booster at $M = 1.46$, $\alpha = 10^\circ$

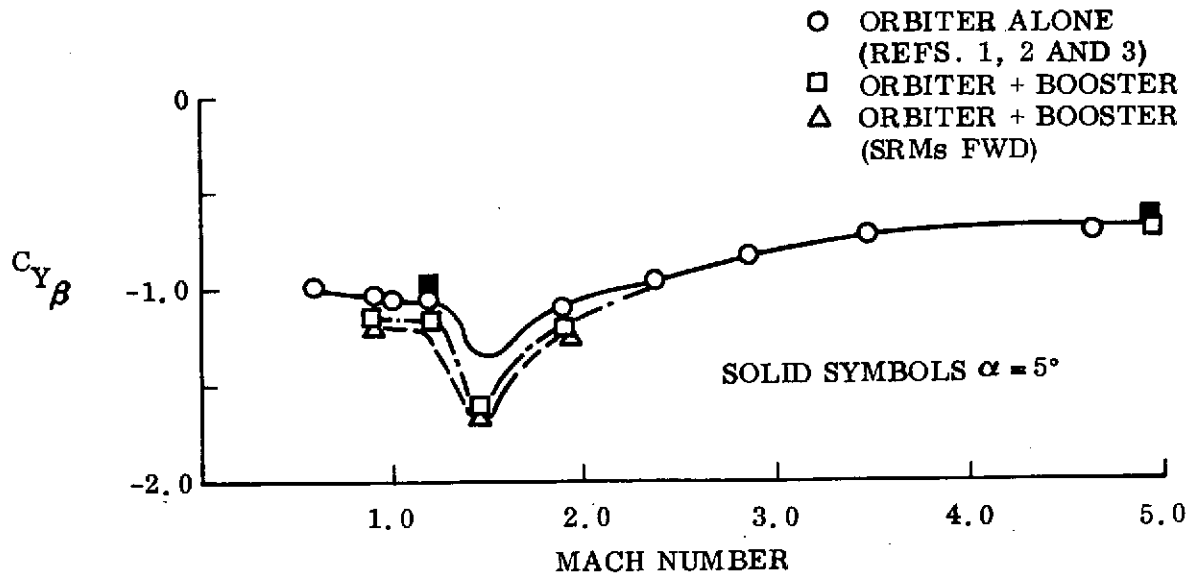


a. $\alpha = 5^\circ$

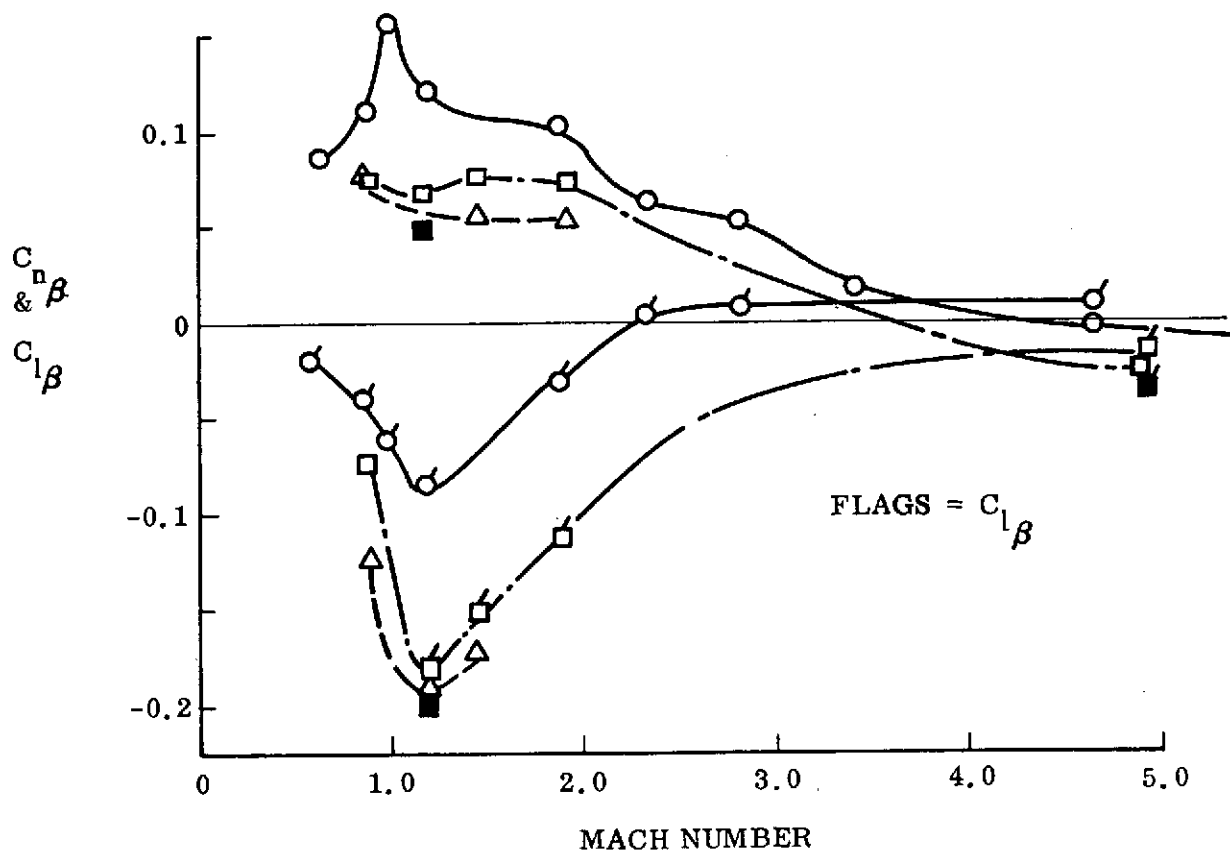


b. $\alpha = 10^\circ$

Figure 18. Shadowgraph Photographs of ATP Booster at $M = 1.46$, $\alpha > 0$

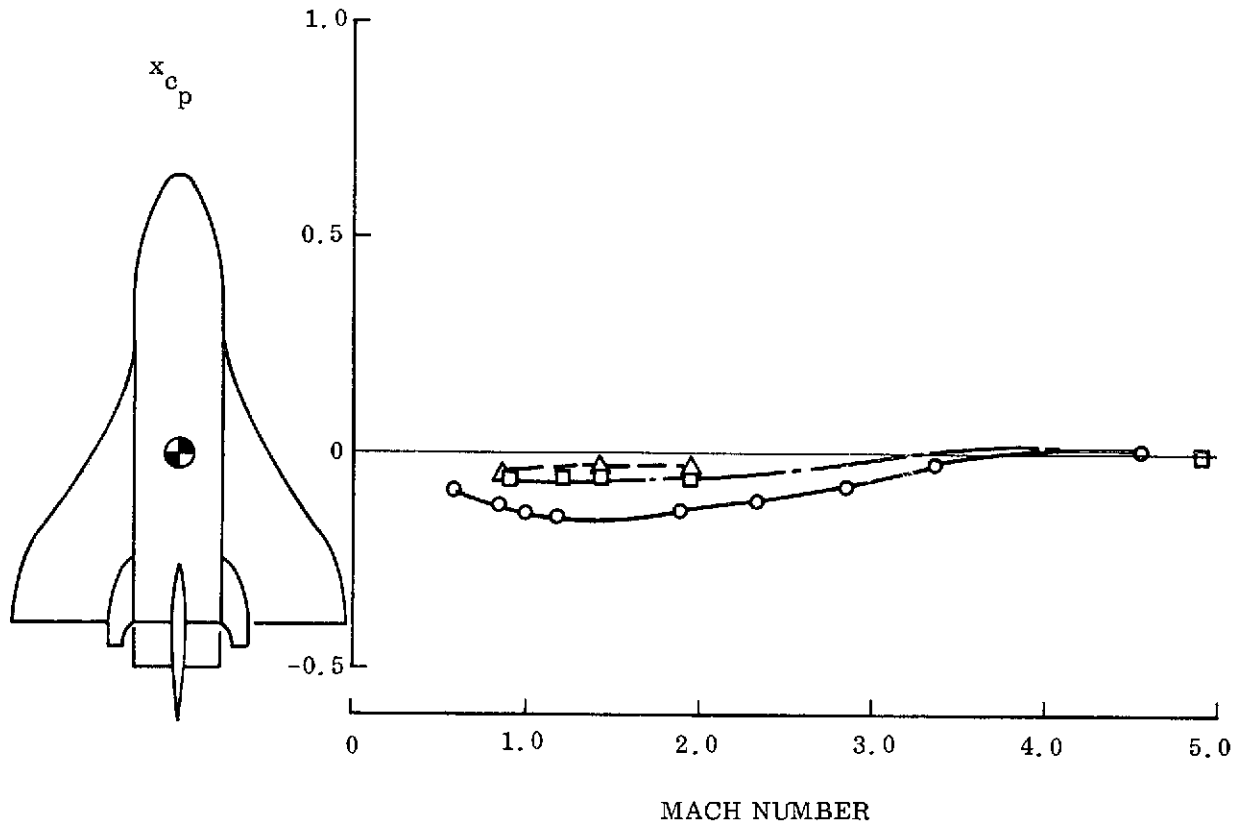


a. Side Force Derivative



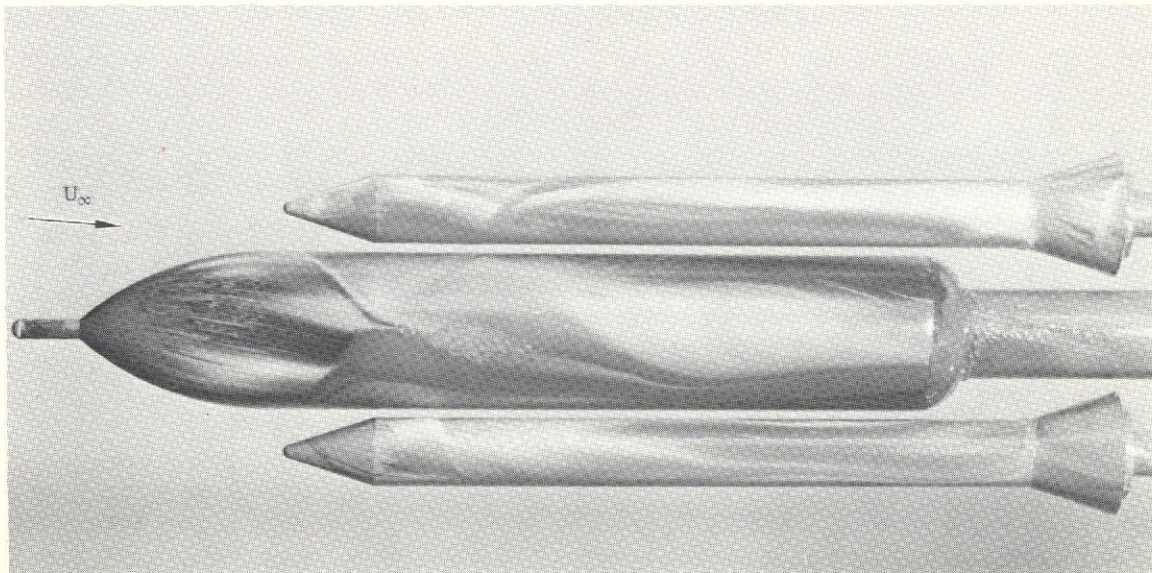
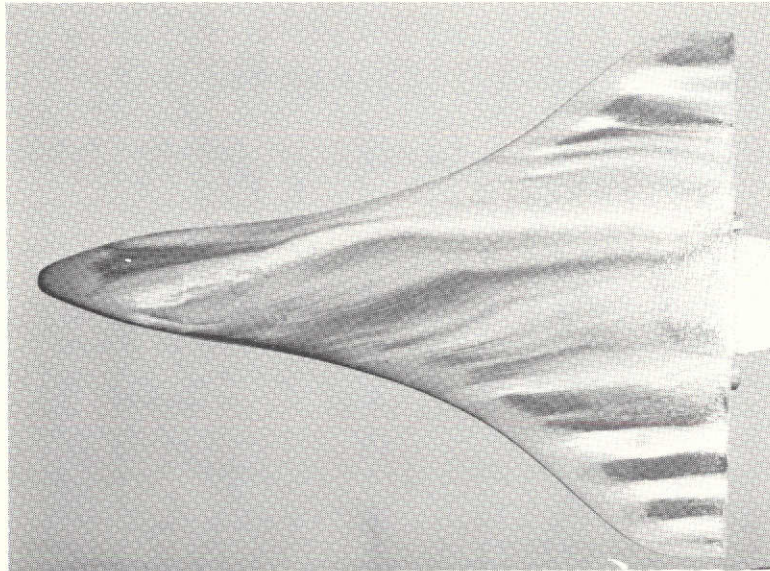
b. Yawing and Rolling Moment Derivatives

Figure 19. Effect of Booster Interference on Orbiter Lateral-Directional Stability at $\alpha = 0$, ATP Configuration (Sheet 1 of 2)



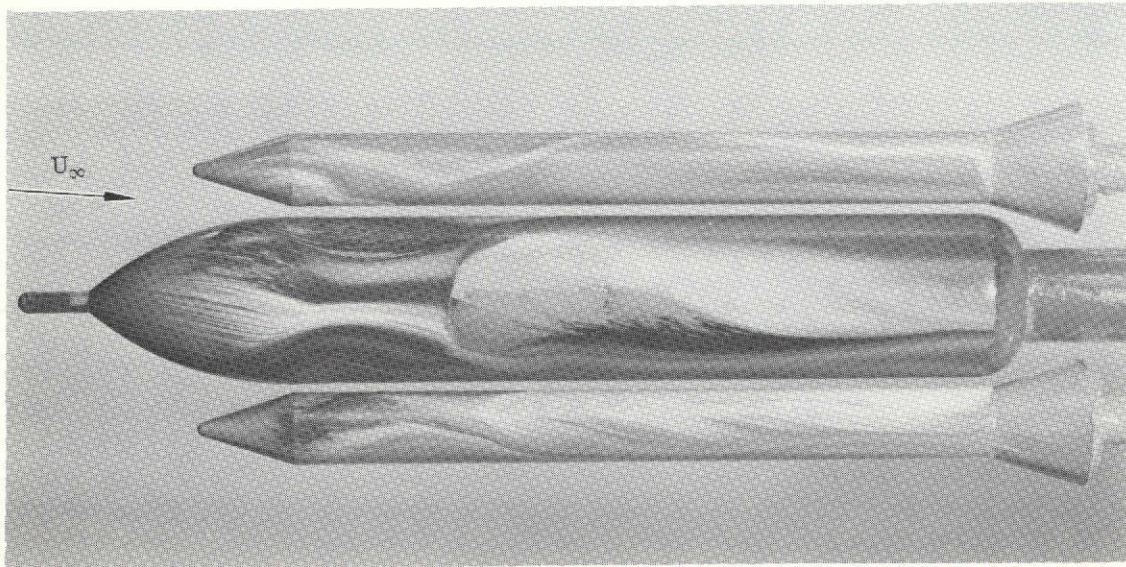
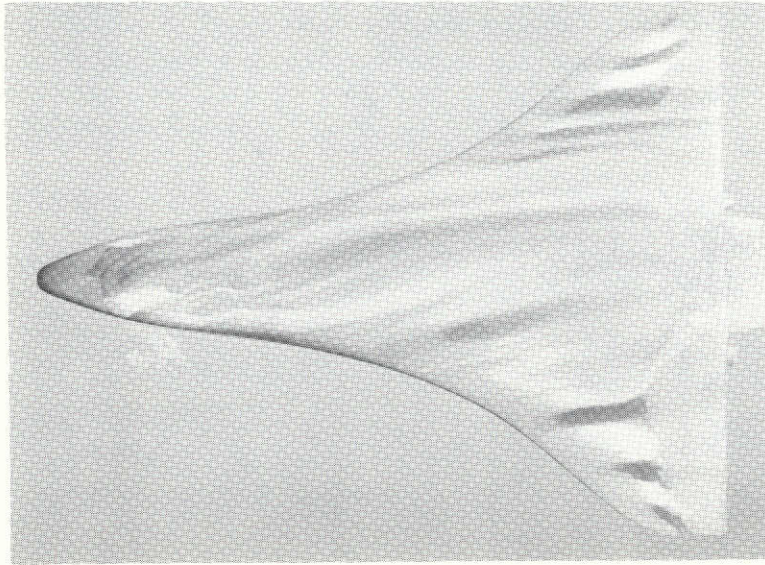
c. Center of Pressure

Figure 19. Effect of Booster Interference on Orbiter Lateral-Directional Stability at $\alpha = 0$, ATP Configuration (Sheet 2 of 2)



a. NORMAL SRM; $M = 1.46$, $\beta = 5^\circ$

Figure 20. Effect of Sideslip Angle on the Interference Flow Field, ATP Configuration, $\alpha = 0$ (Sheet 1 of 2)



b. FORWARD SRM; $M = 1.46$, $\beta = 5^\circ$

Figure 20. Effect of Sideslip Angle on the Interference Flow Field, ATP Configuration, $\alpha = 0$ (Sheet 2 of 2)

Section 3 BOOSTER LOADS

In this section, pressure distribution results for the 049 boost configuration from Ref. 12 are examined to gain further insight into the interference effects on the booster itself. The results tend to support the assertion that the flow fields are similar for the various shuttle-booster configurations.

Previous experimental results (Ref. 13) have determined that the presence of separated flow on cone-cylinder bodies is revealed by the magnitude of the shoulder pressure. In Fig. 21, corner pressure results for the 049 SRM and the HO tank are compared to cone-cylinder data from the literature (Refs. 13, 14)* for $\alpha = 0$. These data indicate that the SRM corner flow is separated at subsonic speeds and attached at supersonic speeds. The flow over the upper meridian on the HO tank is always attached; but adjacent to the SRM, the flow is separated throughout the Mach number range, owing to the interference from the SRM shoulder. The anomaly at $M = 1.96$ results from the SRM shock reflecting almost directly on the shoulder, affecting the shoulder pressures.

Comparison of pressure distribution results for the HO tank at $M = 0.95$ with cylinder pressure distribution data shows that the pressures over the top meridian directly aft of the shoulder are typical of attached flow (Fig. 22a); however, adjacent to the SRM, the shoulder pressure distribution is similar to that for nose-induced separation. The presence of the SRM nose increases the upstream pressures on the HO tank nose (see $\phi = 60^\circ$ and $\phi = 75^\circ$ in Fig. 22a). The pressure distributions at nearly adjacent meridians on the SRM and HO tank are very similar as one would

*The small differences in configuration (2° in cone angle) between the data (Refs. 13, 14) and the 049 booster results (Ref. 12) are considered negligible for indicating the presence of separated flow.

expect (as long as no shocks or expansions are reflected from the nose or impinge from other body elements, e. g. , orbiter nose, wings, etc.).

Similar comparisons can be made at supersonic speeds, including the comparison between the pressures on the orbiter bottom and the HO tank top (Figs. 23 and 24). Note that the pressure distribution on the HO tank top has not been faired through three of the data points. Unpublished developmental oilflow results* show that the unscaled orbiter supports caused significant flow perturbations (Fig. 25). The oilflow indicates that bow shocks, wakes, and wake neck shocks were generated by the supports. Thus, the pressures in the vicinity of the supports are not to be believed. The fairing used in Figs. 23 and 24 is based on the orbiter pressures. The load distributions derived from the pressure data are likewise in error; and thus, the fairing of the data in Fig. 26 also ignores these data points. The fairing is, of course, somewhat subjective, but there is no reason to question the loads forward of the supports. The load distributions at $\alpha = 0$ show that the addition of the SRMs causes a download on the HO tank nose (and shoulder). If the integrated lumped-load components are plotted against α , it shows that the effect of the SRMs is simply to zero-shift the nose load and adjacent cylinder-shoulder load (Fig. 27). There is no alteration of the α -derivatives. Load components 1 and 2 are simply attached flow loads that have been displaced. The negative load component 3 induced by the orbiter bow shock is another matter, however. The impinging bow shock from the orbiter causes a local separation on the HO tank top. The situation is qualitatively the same as the flow field for the ATP booster with the SRMs in the forward position (Fig. 7). However, this negative shock-induced load tends to vanish with increasing α , which is opposite the usual trend of shock-induced loads (Refs. 9, 10, 15, 16). When the SRMs are added to the HO tank, there is a second suction peak in the pressure distribution at about $x/c = 2.0$ (Fig. 28). This is the effect of the shared expansions at the SRM shoulder, an effect that generates a favorable pressure gradient just forward of where the orbiter bow shock impinges for the complete booster configuration (Fig. 23). When the vehicle is pitched, the

*The oilflow results are termed developmental since the few runs that were made were aimed at developing technique (oil viscosity, run time, etc.). Unfortunately, the test was terminated before the technique was perfected or any significant data obtained.

greater expansion from the leeward side of the SRM gives a more favorable pressure gradient forward of the impinging orbiter bow shock. As a result, the region of shock-induced separation does not expand but decreases with increasing α . Thus, the negative load induced by the orbiter shock tends toward zero with increasing α when the SRMs are attached, rather than becoming more negative as it does for HO tank plus orbiter (compare Figs. 24a and 29). Consequently, a positive induced $C_{N\alpha}$ contribution that is dependent upon the crossflow at the SRM shoulder is generated in the region of orbiter shock impingement on the booster (Fig 30).

The aft load, component 4, on the HO tank (Fig. 27) appears to vary mainly as the result of the expansion with α of the forward separation region (load component 3) limiting the extent of load component 4 (Fig. 26). This load component 4 is considered to be a local load rather than an induced load, at least for small α where the vortices generated by the SRM-HO interaction are restricted to near the lateral meridian of the HO tank.

The loads over the SRM are somewhat similar to the HO tank loads (compare Figs. 27 and 31). The nose cone load (load 1 in Fig. 31) is local, of attached flow type. The negative shoulder load (load 2) is the result of the nose-induced separation (Refs. 15, 16). The large negative load with the positive α -slope (load 3) is the result of the orbiter bow shock impingement. The vortices from the SRM-HO tank separation bubble are being swept or skewed to the leeward side at angle of attack (Fig. 32). They tend to energize the boundary layer and retard the separation for increasing α , giving a positive α -slope to the negative load (load 3). Finally, the aft body load on the SRM (load 4) is the result of the channel flow under the orbiter just like its counterpart on the HO tank. Fig. 30 illustrates the strong similarity between the $C_{N\alpha}$ distribution on the SRM and the HO tank.

Load 3 on the HO tank (Fig. 27) and loads 2 and 3 on the SRM (Fig. 31) are considered to be induced because they depend upon conditions at the SRM shoulder. Dynamically they are treated exactly like the loads in a region of nose-induced separation (Ref. 16), which the interference flow field resembles. The induced loads on

each booster element (HO tank and SRM) significantly affect the aerodynamic damping of that element. The aerodynamic damping of each booster element was computed for the 3.64-Hz symmetric mode of the 049 booster (Fig. 33, Ref. 17) using the analytic method of Refs. 15 and 16. The shock-induced separation load contributes negative damping to the HO tank but is not sufficient to cause total undamping of the HO tank (Fig. 34). The negative HO tank load due to the shock-induced separation (load 3 in Fig. 27) is, of course, totally induced, but it is less clear to what extent the expansion-separation loads on the SRM (loads 2 and 3 in Fig. 31) are induced. Obviously, the attitude at the SRM shoulder sets the initial separation or vortex asymmetry, but the local crossflow may also play a part in determining the vortex asymmetry. Thus, the effective elastic damping derivative has been calculated, allowing for variations in the shoulder loads all the way from entirely induced to entirely local (Fig. 34). At $M = 1.2$, the entire booster is undamped when $\Delta^i C_{N_{\alpha_I}} / C_{N_{\alpha_I}} = 0.73$. The possibility of negative aerodynamic damping seems real enough to warrant further investigation, especially since it appears possible that negative damping can occur over a significant range of the supersonic Mach numbers investigated (Fig. 35).

It should be pointed out that whether or not a particular induced load is undamping depends on the mode shape. The general rule is that if an induced load is statically stabilizing, the time lag effect will cause it to be undamping. The shock-induced separation load is undamping for the investigated 3.64-Hz separation mode. It could easily be undamping for other modes also. Thus, more mode shapes need to be investigated. Finally, these results are for a configuration where SRM and HO tank shoulders are aligned, similar to the forward SRM configuration in Figs. 7c and 7e, which the oil flow studies showed to have a relatively minor orbiter-induced separation. With the SRMs in normal position, the separation on the HO tank is considerably greater (Figs 7b, 7d); and the separation-induced effects are much more likely to cause aero-elastic instability.

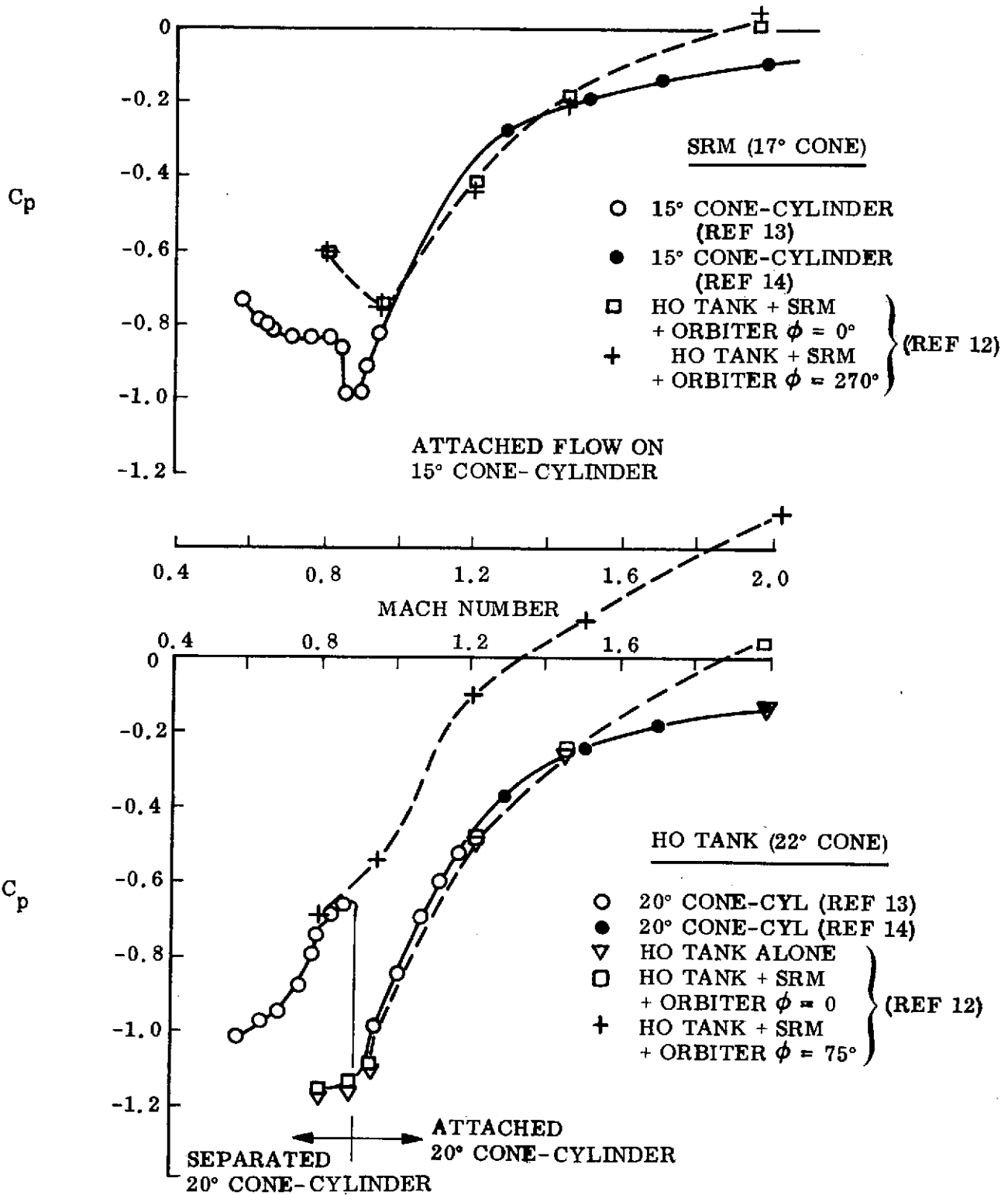


Figure 21. Comparison of Booster Element Shoulder Pressures, 049 Booster, $\alpha = 0$

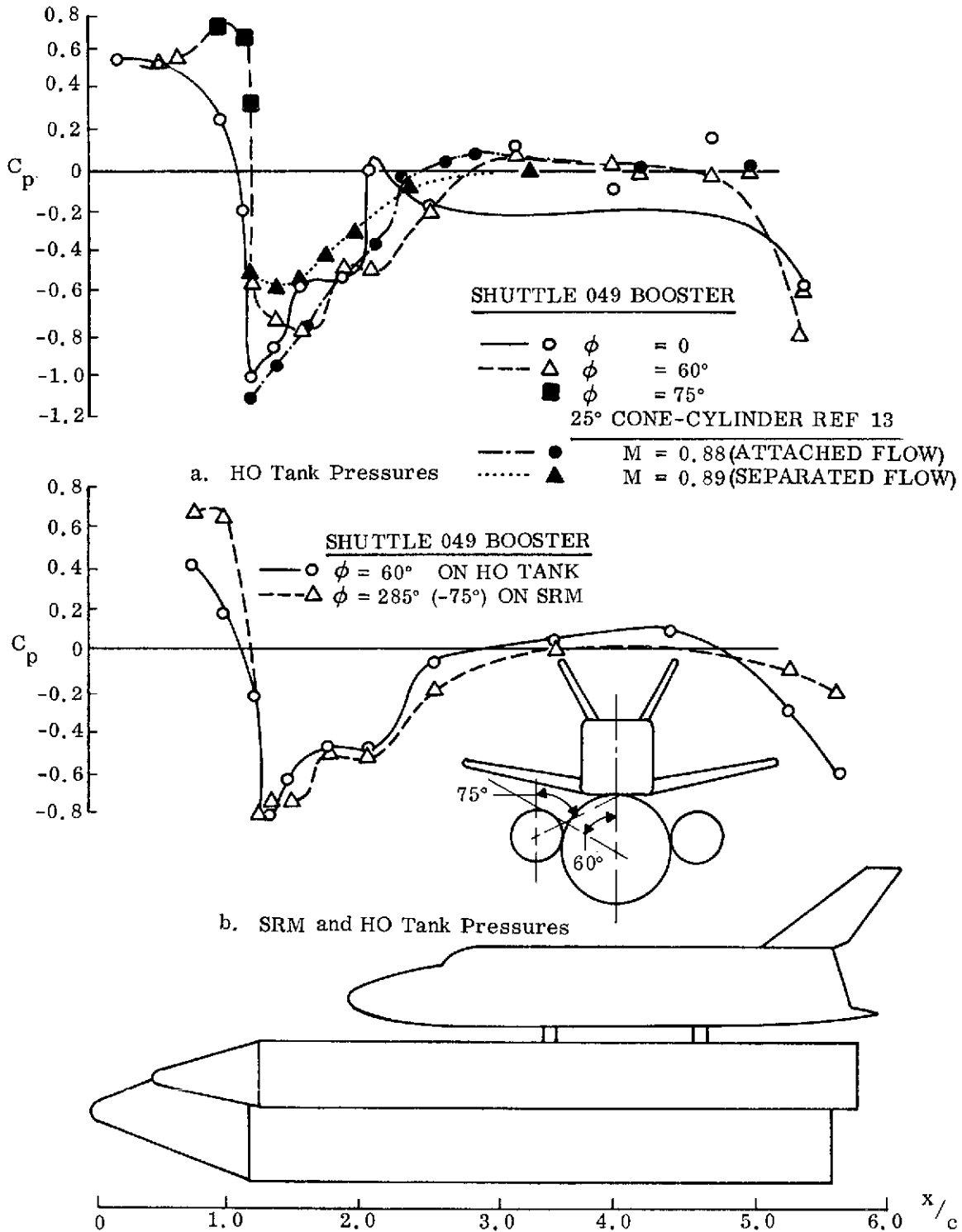


Figure 22. Comparison of HO Tank and SRM Pressures, 049 Booster, $M = 0.95$, $\alpha = 0$ (Ref. 12)

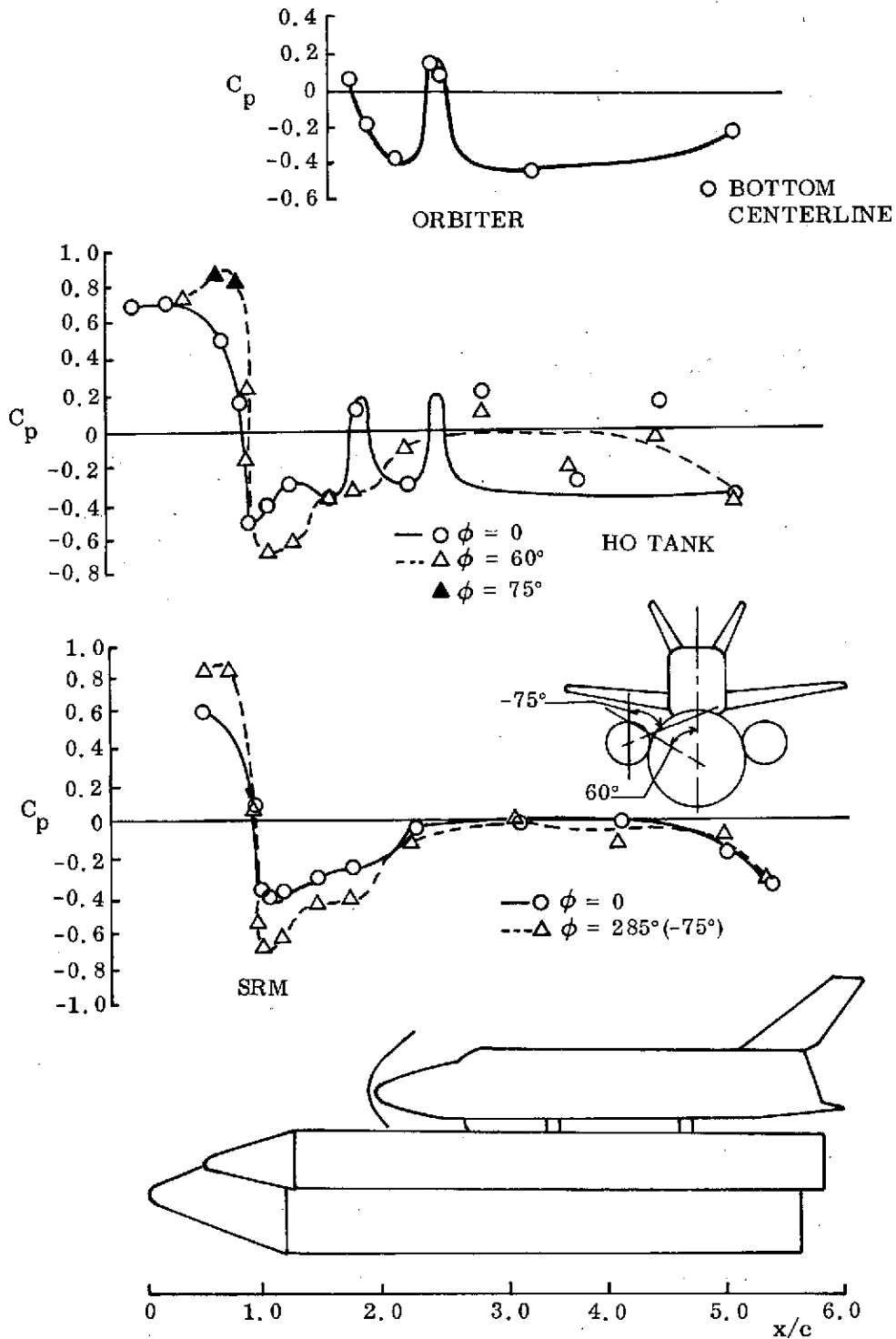


Figure 23. Comparison of Orbiter, HO Tank, and SRM Pressures, 049 Booster, $M = 1.2$, $\alpha = 0$ (Refs. 3 and 12)

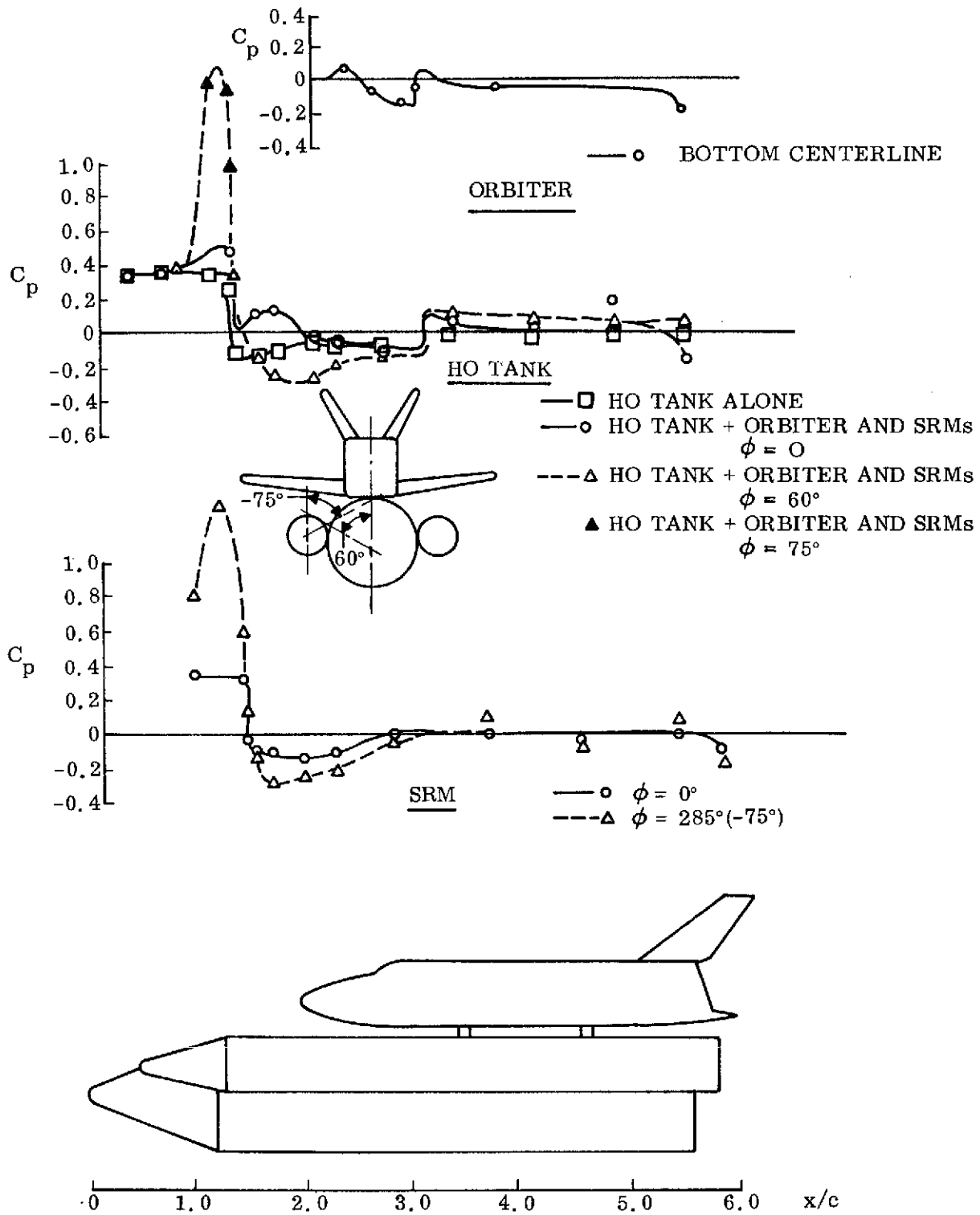


Figure 24. Comparison of Orbiter, HO Tank, and SRM Pressures, 049 Booster, $M = 1.96$, $\alpha = 0$ (Refs. 3 and 12)

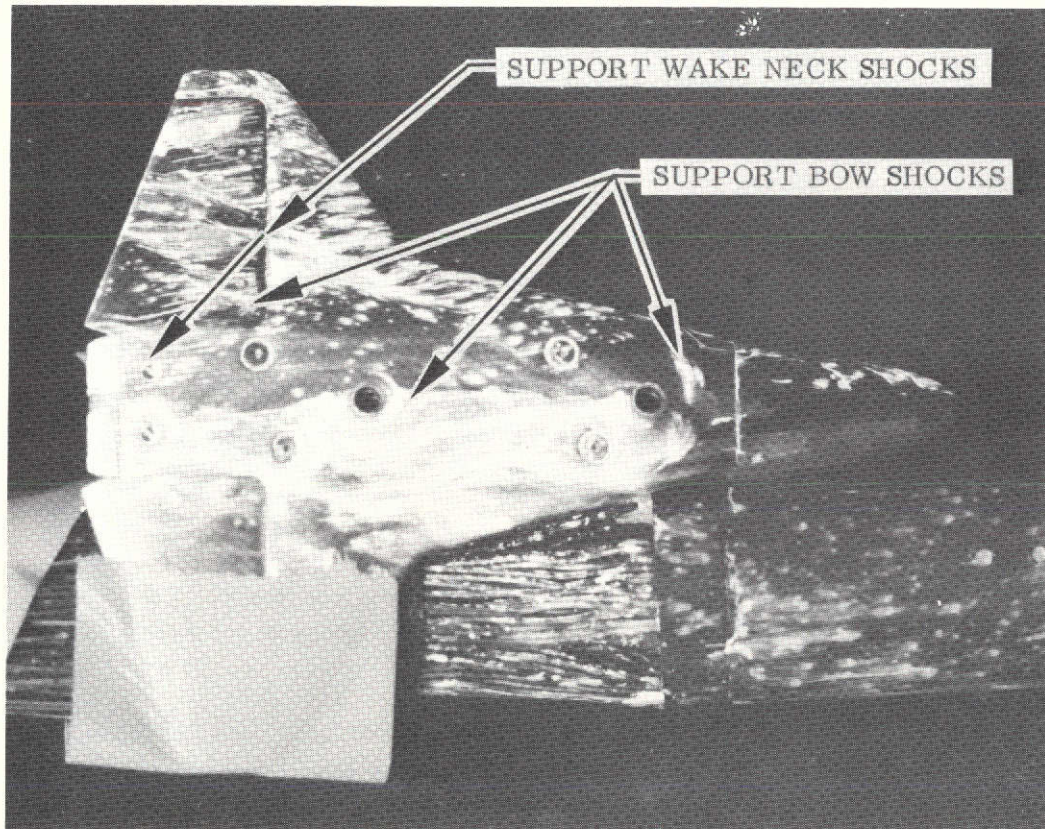


Figure 25. Effect of Orbiter Mounting Posts on the Interference Flow Field on the Bottom of the 049 Orbiter, $M = 1.96$

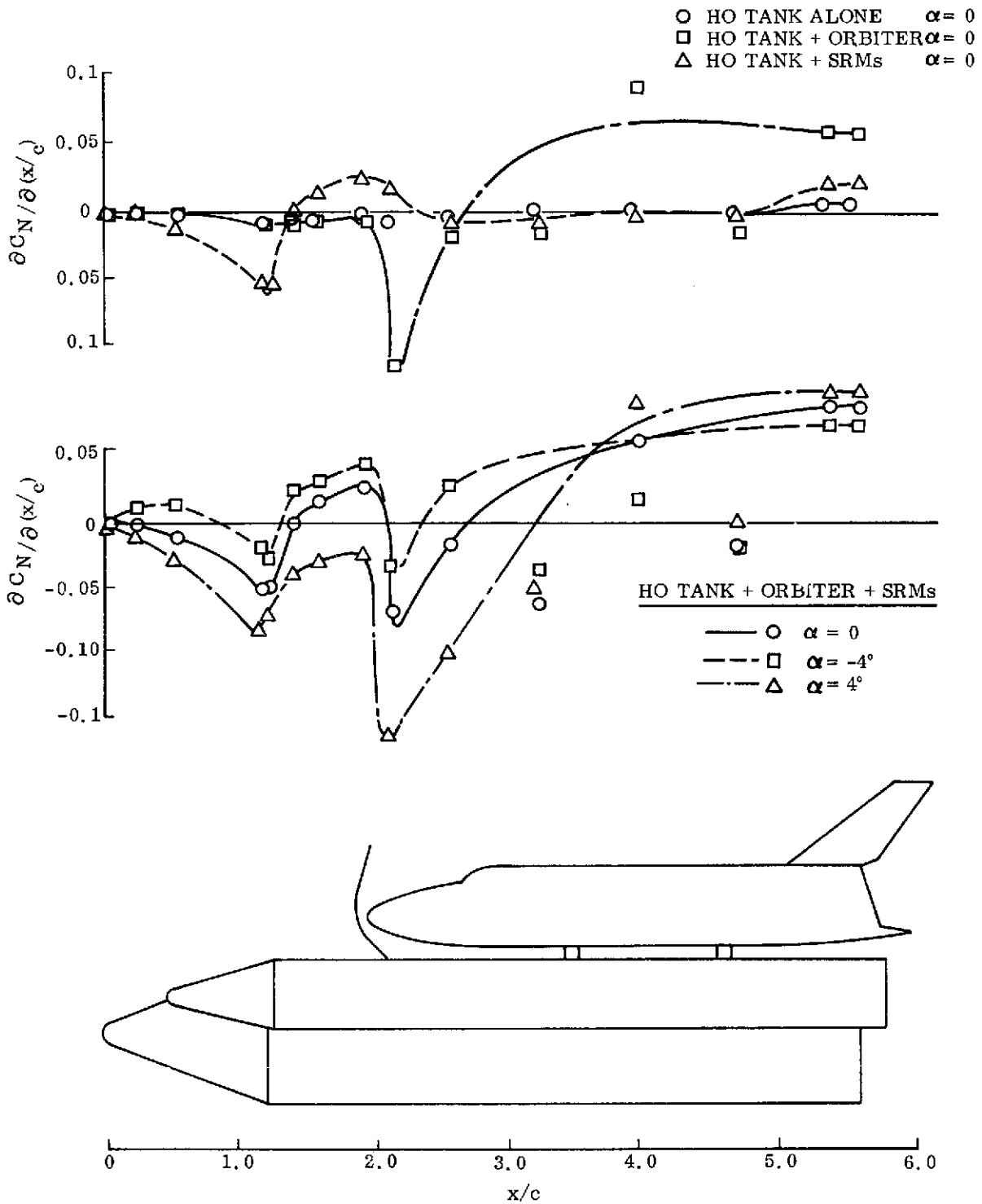


Figure 26. Interference Effects on HO Tank Load Distribution, 049 Booster, $M = 1.2$ (Ref. 12)

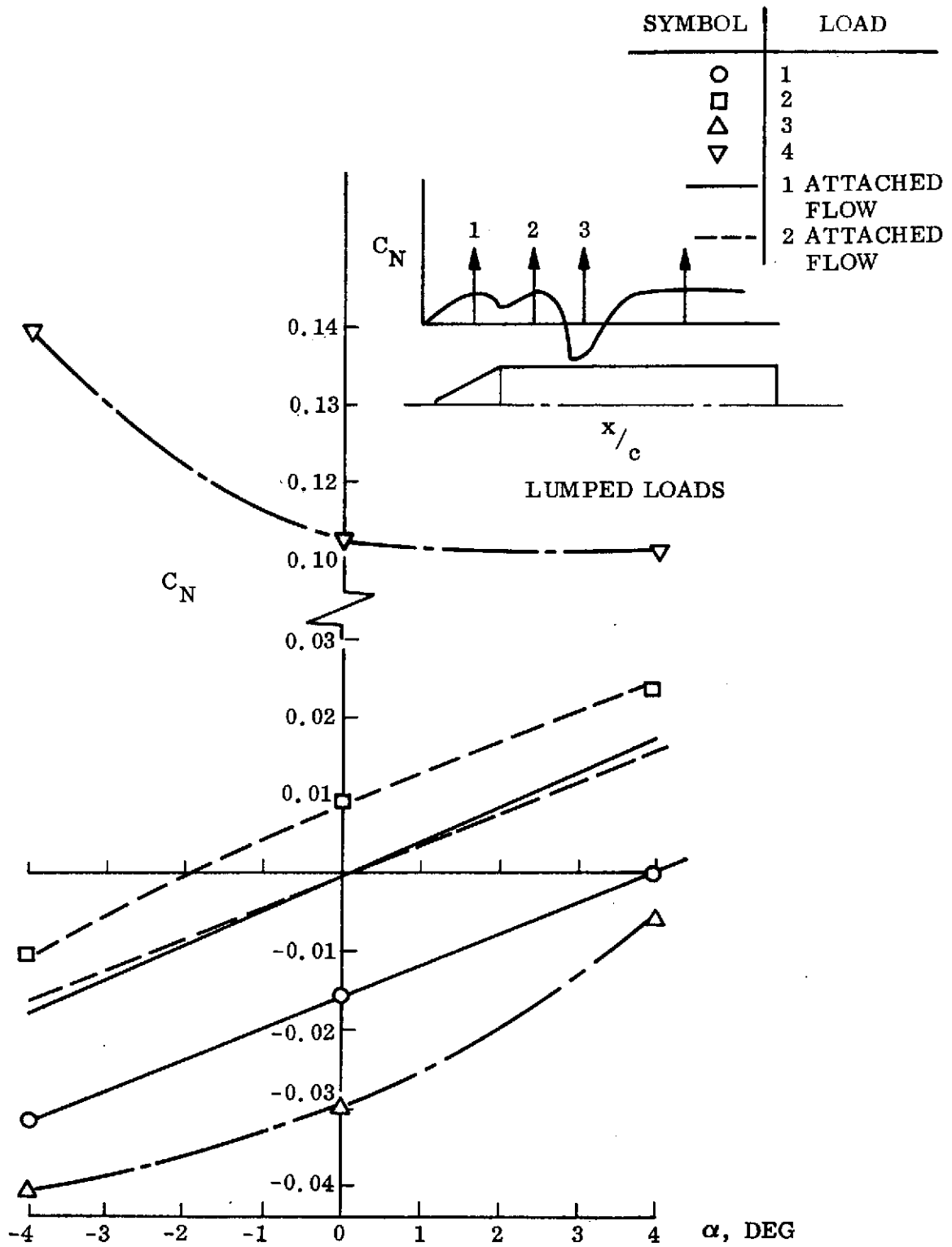


Figure 27. HO Tank Lumped Loads for 049 Booster, $M = 1.2$

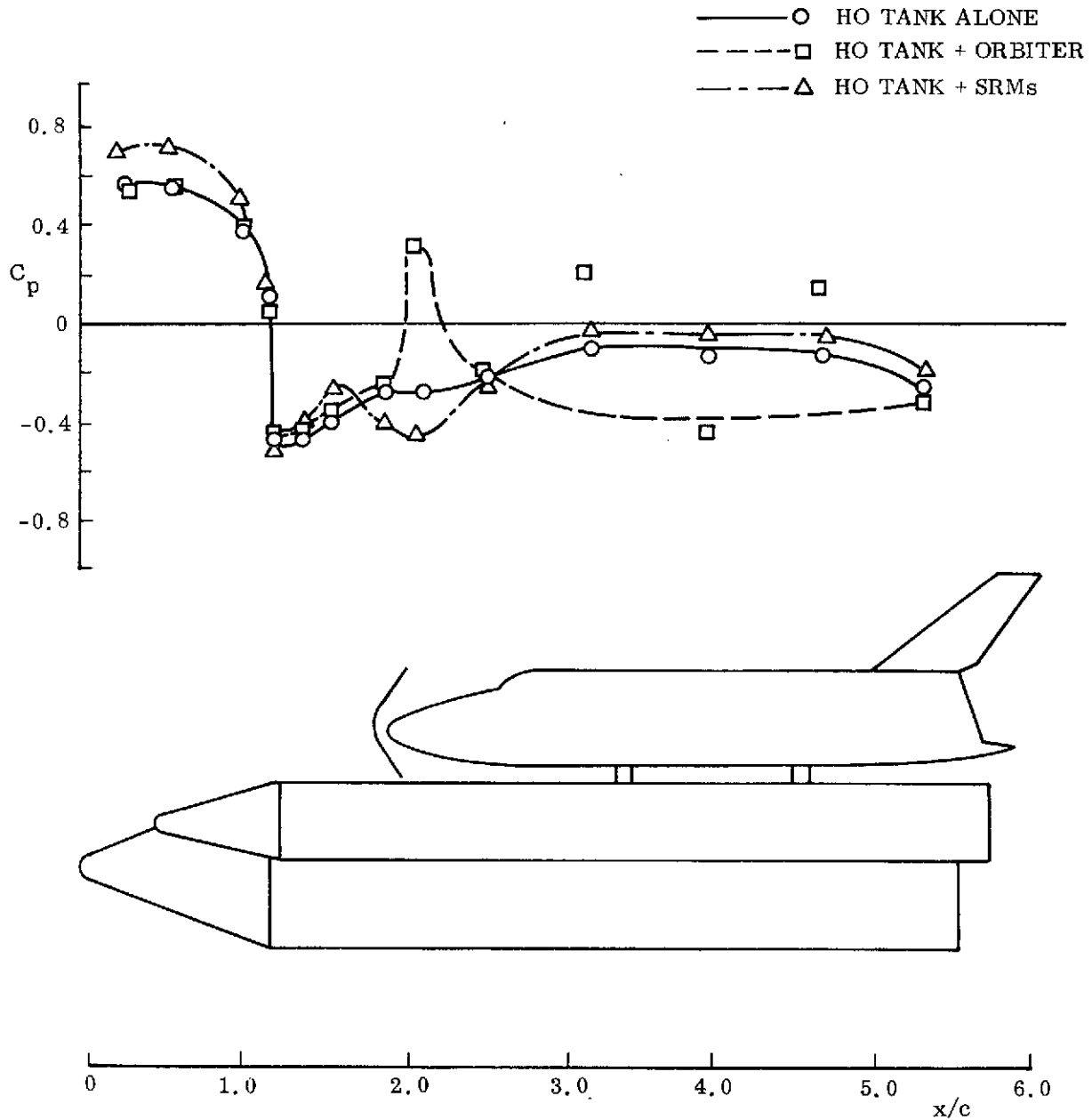


Figure 28. Comparison of Interference Effects on HO Tank $\phi = 0$ Pressures, 049 Booster, $M = 1.2$, $\alpha = 0$ (Ref. 12)

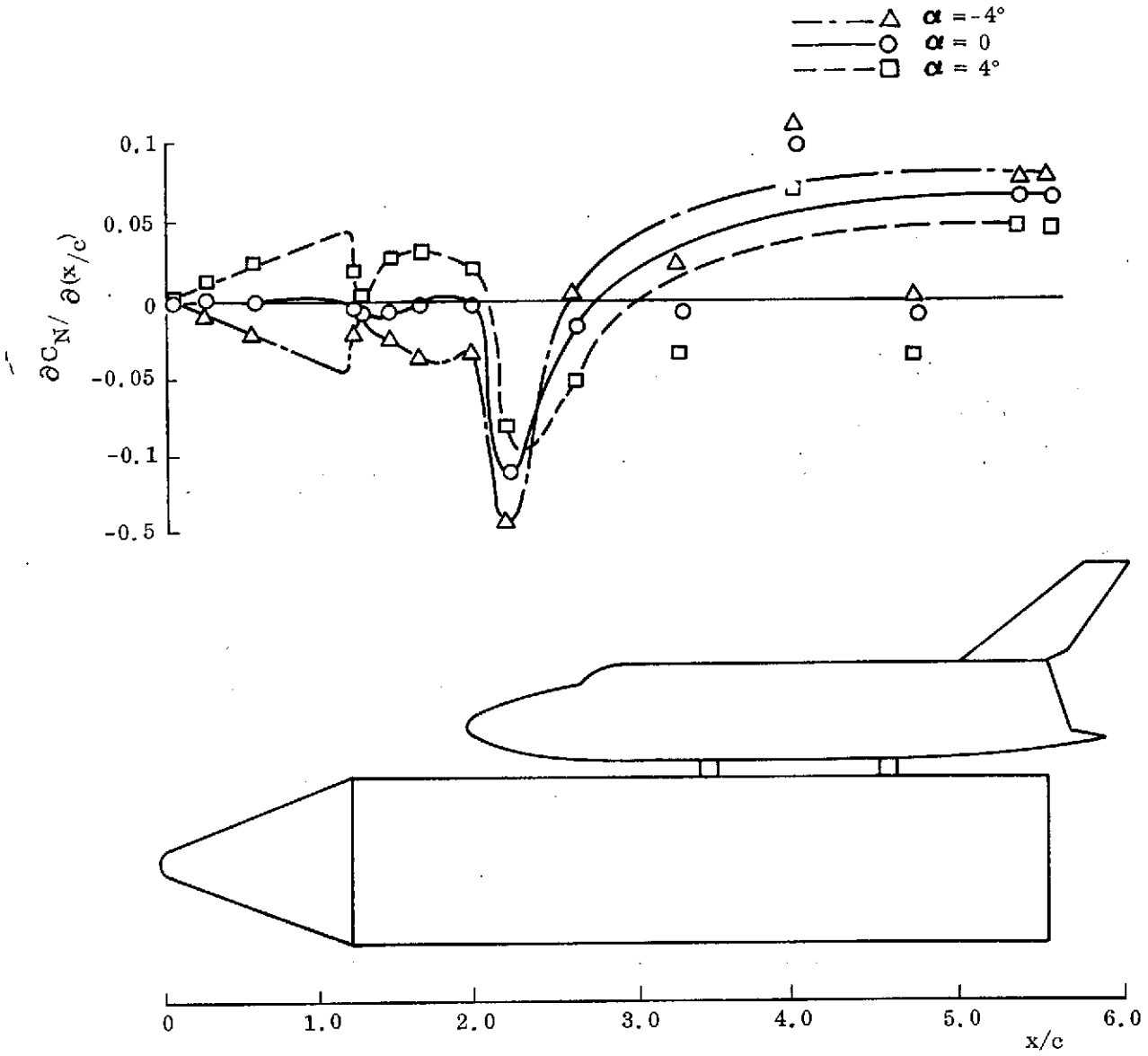


Figure 29. Effect of α on HO Tank Load Distribution for HO Tank and Orbiter, 049 Booster, $M = 1.2$ (Ref.12)

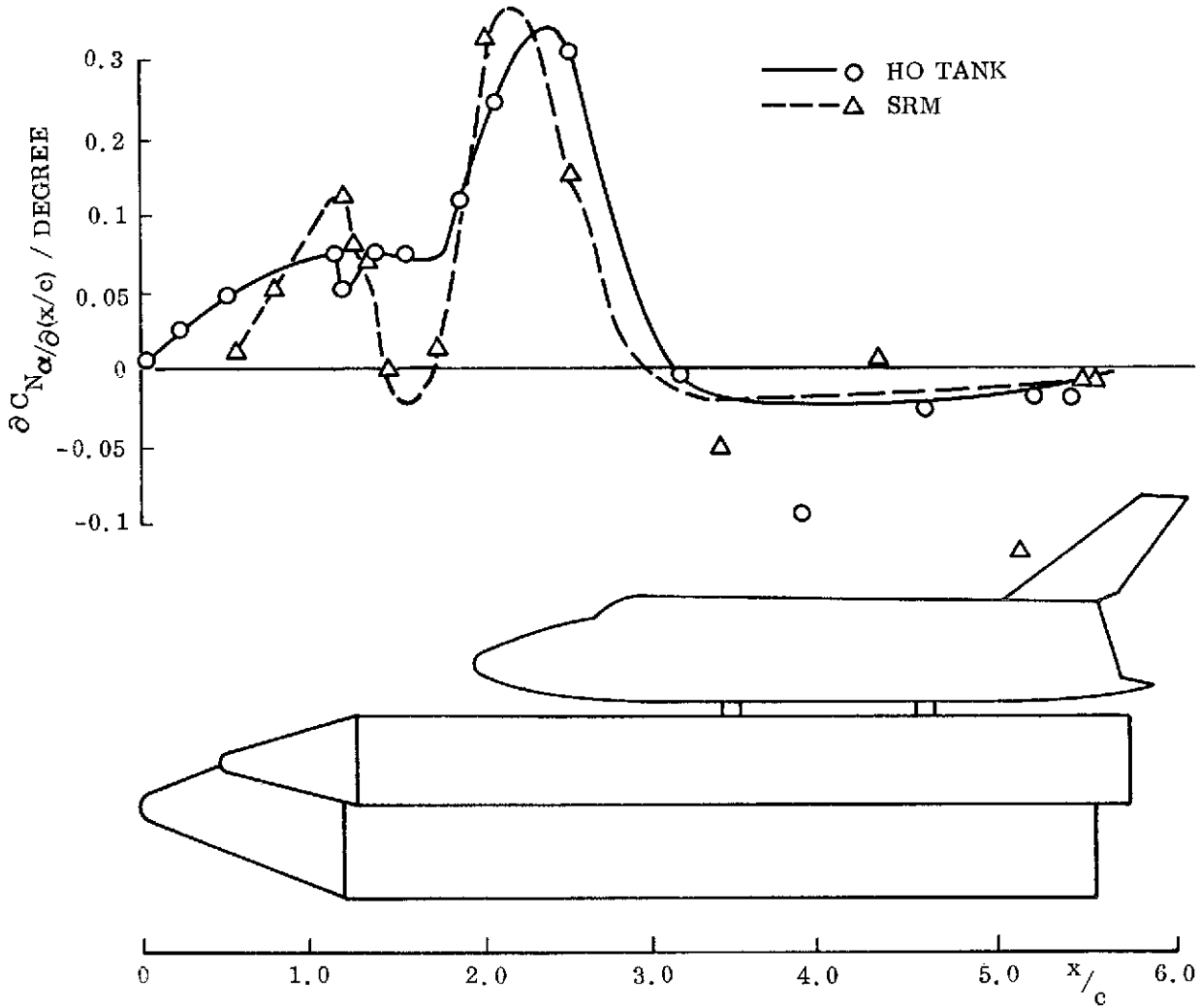


Figure 30. Comparison of HO Tank and SRM $C_{N\alpha}$ Distributions at $\alpha = 0$ for the 049 Booster, $M = 1.2$ (Ref. 12)

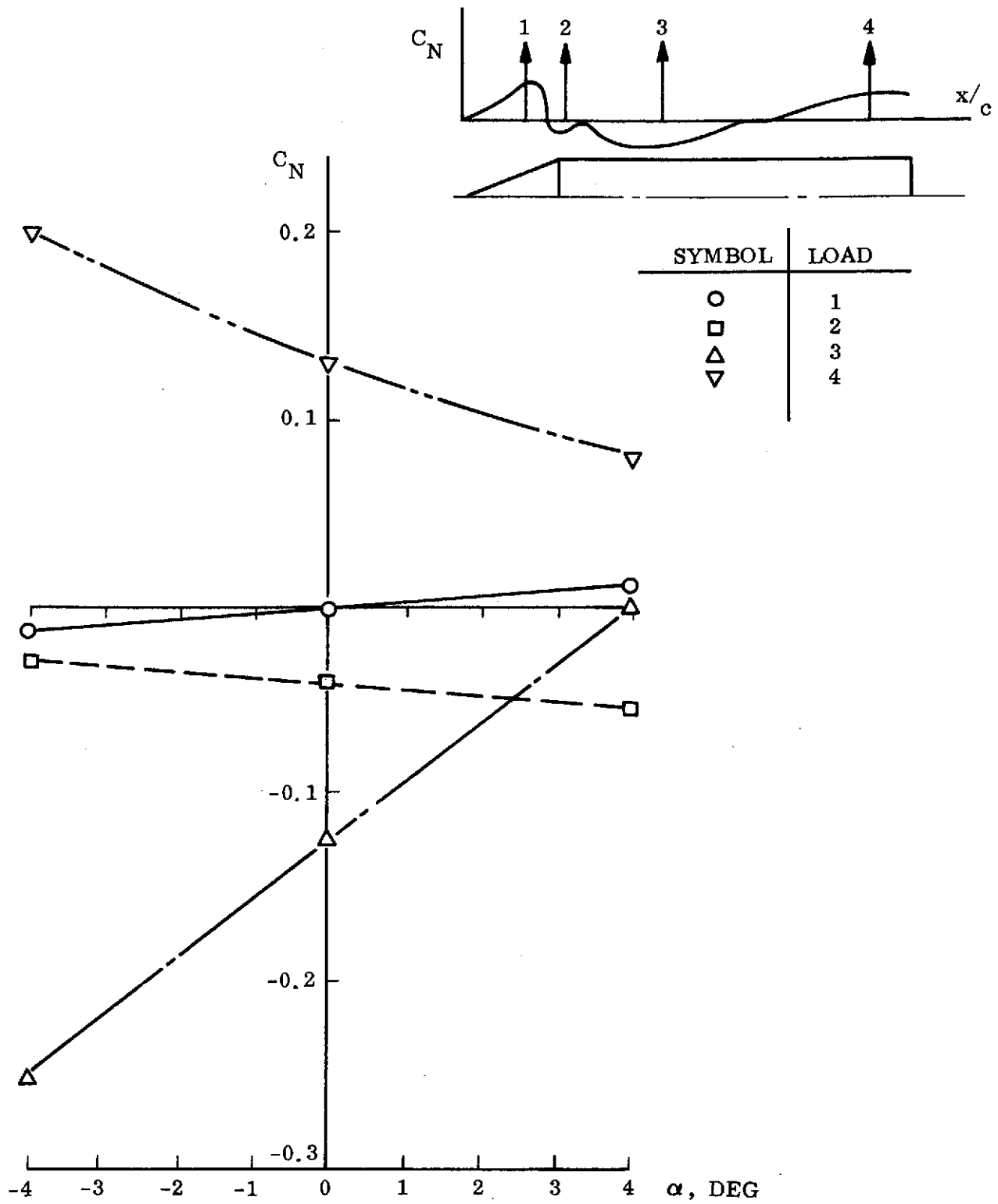


Figure 31. SRM Lumped Loads for 049 Booster, $M = 1.2$

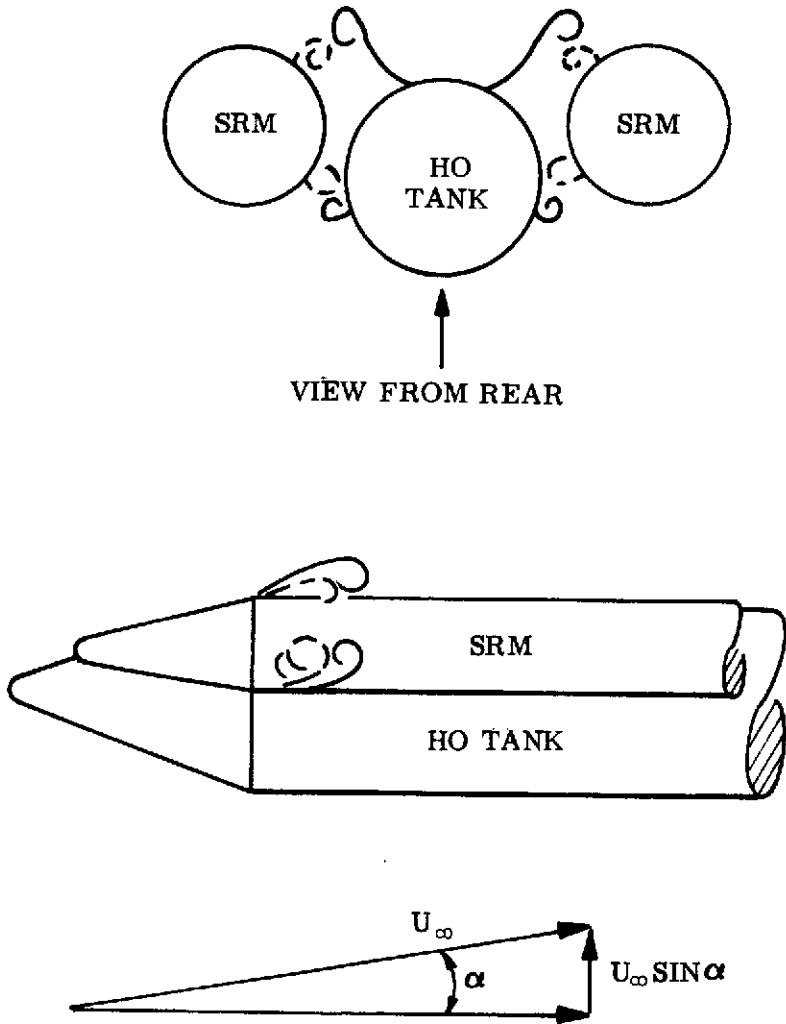


Figure 32. Effect of α on Skewing the Expansion-Separation Vortices Between HO Tank and SRM

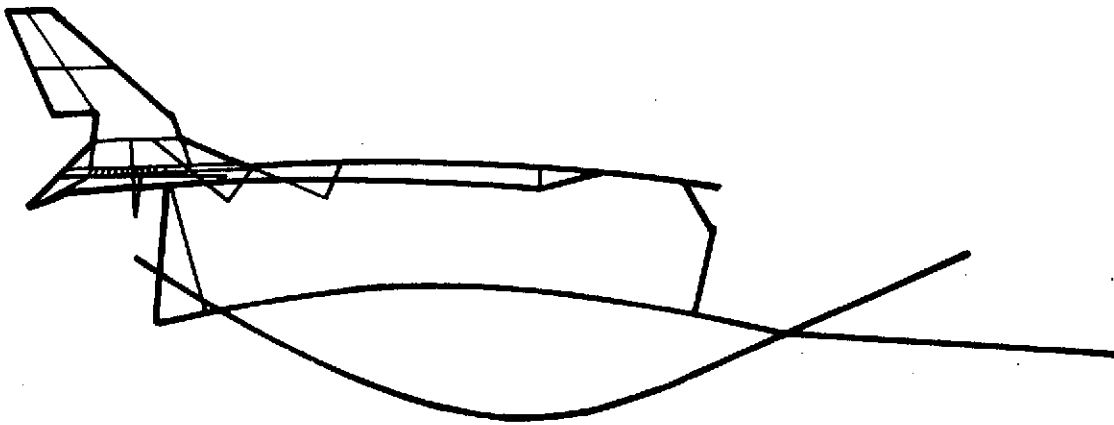


Figure 33. 3.64-Hz Symmetric Mode of the 049 Booster (Ref. 17)

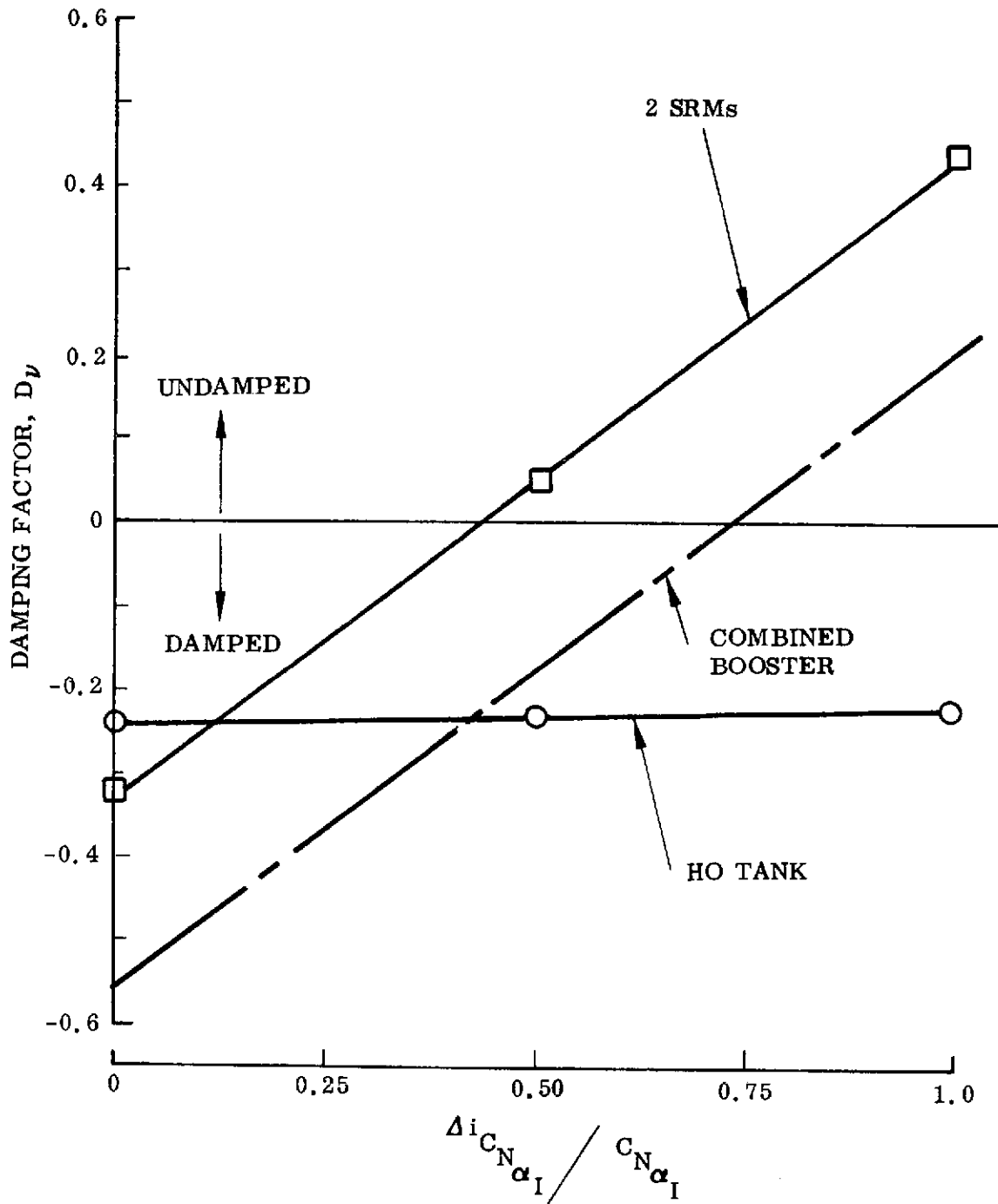


Figure 34. Effect of the Induced Interference Load on the Aerodynamic Damping Factor of the 049 Booster, 3.64 Hz Symmetric Mode, $M = 1.2, \alpha = 0$

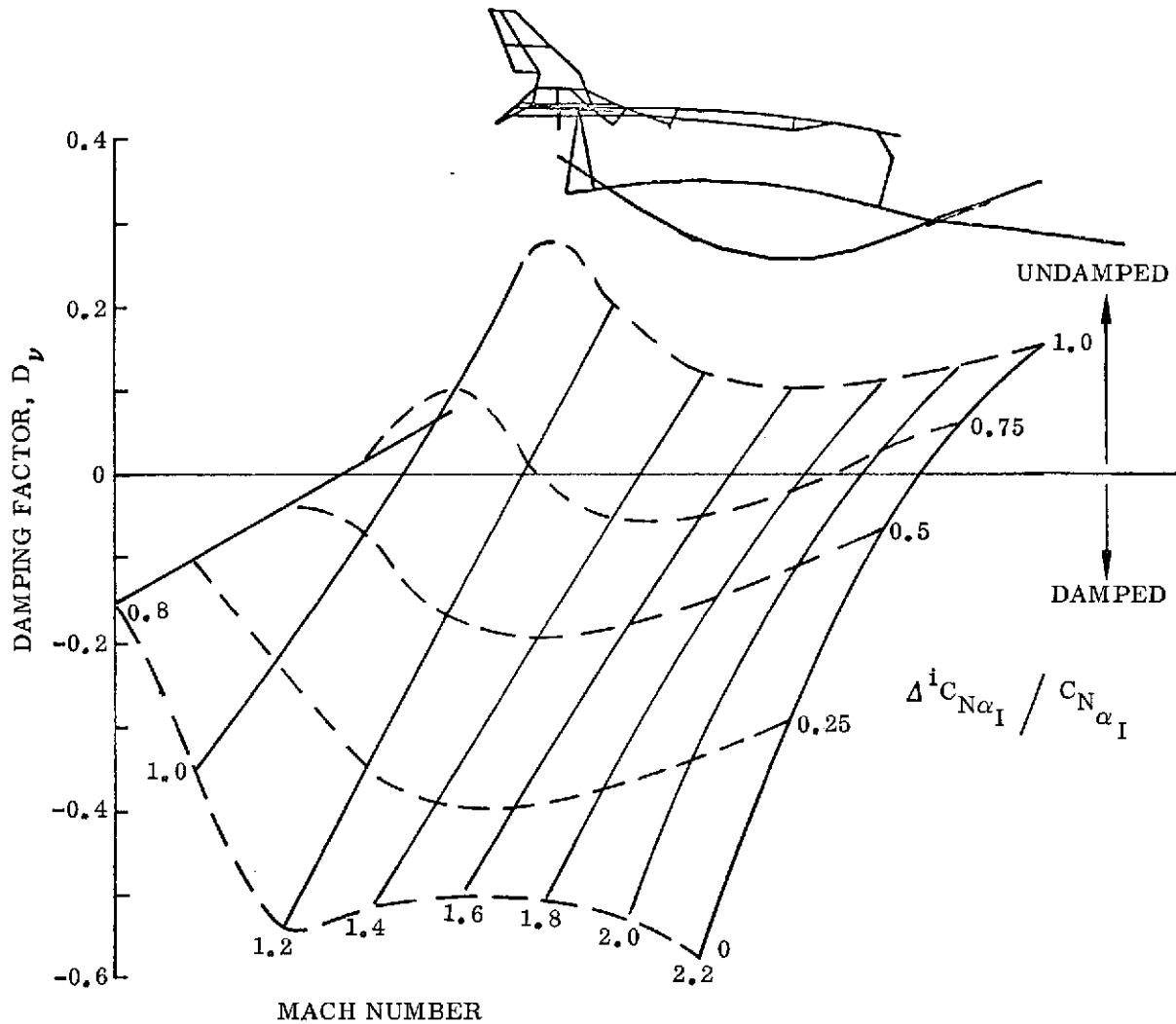


Figure 35. Effect of HO Tank and SRMs on the Aerodynamic Damping Factor of the 0.49 Booster, 3.64 Hz Symmetric Mode, $\alpha = 0$

Section 4
PLUME-INDUCED EFFECTS

A preliminary study of the effect of the exhaust plumes of the SRM and orbiter engines showed that the plumes, simulated by solid bodies, could cause a significant alteration of booster stability (Ref. 18). Dods et al. have obtained qualitatively similar results for gaseous plumes (Ref. 19). Both investigations (Refs. 18, 19) indicate that the plumes cause a large trim change at $\alpha = 0$ (Fig. 36a). The plumes evidently cause a flow separation over the delta wing. This is borne out by the observed loss in elevon control effectiveness (Refs. 18, 19). Because of the negative incidence of the orbiter relative to the booster centerline, the orbiter is at a negative attitude (-3.5° in Ref. 18 and -3.0° in Ref. 19) at $\alpha = 0$. Thus, the wing, which dominates the booster stability, is producing a negative lift. The separation between the booster (HO tank plus SRMs) and the orbiter reduces the negative lift, causing a positive $\Delta^i C_{N_{op}}$ and, because the wing is aft of the center of gravity, a negative $\Delta^i C_{m_{op}}$ (Fig. 36a). Thus, the major force change due to the plume-induced separation occurs between the booster and the orbiter. That is, the exhaust plumes (solid or gaseous) act as large sting flares (Ref. 20) and cause a flow separation to occur between the booster and the orbiter similar to the one caused by the SRM flares on the ATP configuration with SRMs forward. Comparison of Figs. 36 and 12 indicates that the effect of the plumes on C_{m_o} is approximately the same as the effect of the SRM flares on the orbiter C_{m_o} at $M = 1.2$. Thus, it does not take an unrealistically large separation to produce interference effects of this magnitude. Further corroborating evidence of the dominance of the separation between the stages is furnished by unpublished oilflow photographs from investigations by Dods et al. that show a large region of separation on the bottom surface of the orbiter wing for $-4^\circ \leq \alpha \leq 2^\circ$ and little or no effect on the upper surface. Henderson has published one of Dods' oilflow photographs in Ref. 21; it shows a nearly negligible plume-induced leeside flow separation at the very

trailing edge of the orbiter wing at $\alpha = 4^\circ$, $M = 1.6$. A sketch of the postulated plume-induced flow field is shown in Fig. 37. When the booster is pitched, the vortices that are shed by the various separated flow regions (Fig. 7) move to the leeward side. The flow entrained by these vortices, assisted by the local flow jetting through the SRM-HO tank gaps, tends to suppress the plume-induced separation as it did for the separation generated by the SRM flare (Fig. 14). The separation shrinks with α , as illustrated in Fig. 37. The result is a decreasing wing load, $-\Delta^i C_{N_{\alpha_p}}$ (Fig. 36b), aft

of the center of gravity (Fig. 36c), which is destabilizing. Yawing the booster skews the separation towards the leeward side. The separation becomes asymmetric on the booster, expanding on the leeward SRM (Fig. 37). Thus, a positive $\Delta^i C_{Y_{\beta_p}}$ is generated on

the aft portion of the booster, giving a negative $\Delta^i C_{n_{\beta_p}}$ (Fig. 38). The booster

vortices cause a reduction in the flow separation on the wing adjacent to the HO tank just as they did for the SRM flow-induced separation. However, the large exhaust plume, which is directed outboard as well, also causes a significant separation at the wing tips. This tip separation expands on the leeside along with the general expansion of the separation on the booster. The separation probably also contracts on the windward wing due to local crossflow effects. These tip effects dominate the rolling moment, causing a positive $\Delta^i C_{l_{\beta_p}}$ (Fig. 38).

The preceding flow model is highly speculative. However, it does fit the available flow visualization evidence; and it explains the plume-induced forces. It also allows one to make some judgment about the important factors affecting the unsteady aerodynamics of the plume-induced loads, the pertinent crossflow influence point, and the convection speed. For example, the induced normal load ($\Delta^i C_{N_{\alpha_p}}$) is the

result of the crossflow at the SRM shoulder because it sets the expansion-separation asymmetry and, thereby, the strengths and trajectories of the associated vortices, which can be assumed to be convected downstream with freestream velocity (Ref. 11). However, $\Delta^i C_{N_{\alpha_p}}$ is also somewhat a function of the flow below the wing jetting through

the SRM-HO tank gap. This can be assumed to happen instantaneously in comparison with the convection of vortex effects. Obviously, it is only possible to make an order-of-magnitude estimate of the effect of the plumes on the aeroelastic stability of the shuttle. Even making these estimates involves more assumptions. Because the only structural deformation modes available were for the 049 booster (Ref. 17), it must be assumed that the plume-induced loads for the 040A and the 049 are the same. Also, slender-body lift was assumed for the rest of the booster. That is, other flow-separation effects were neglected in order to get an estimate of plume-alone effects.

The effect of pitching the 049 orbiter in the vicinity of the booster was obtained from the data of Refs. 22 and 23, and solid-plume results were obtained from Ref. 18. Fig. 39 shows the results of the calculations, which indicate that if half the plume-induced load is due to conditions at the SRM shoulder (i. e., due to vortex suppression of the separation), the plume will cause aerodynamic undamping of the 3.64-Hz symmetric mode for $M \geq 1.6$ (mode shape illustrated in Fig. 33). Furthermore, if the fraction is less than about 37%, no negative aerodynamic damping will result in the Mach range investigated. Calculations were also made for the two asymmetric modes shown in Fig. 40 (Fig. 13). In this case, $\Delta^i C_{Y\beta}$ and $\Delta^i C_{l\beta}$ were assumed to be functions of the crossflow at the SRM shoulders. The orbiter sideslip characteristics were taken from Ref. 24; and the orbiter roll damping was computed from supersonic slender-wing theory (Ref. 25), assuming that the wing was responsible for all the roll damping. The results are summarized in Fig. 41. It appears that negative aerodynamic damping is possible for the 2.76-Hz mode at $M = 2.2$. However, the 3.62-Hz mode is aerodynamically damped, at least for the Mach numbers investigated (i. e., $M = 1.6$ and 2.2). The roll damping of the orbiter is responsible for the higher damping of the 3.62-Hz mode at $M = 2.2$. The relative deflection of the orbiter wing tip for the 3.62-Hz mode is 5.6 times that for the 2.76-Hz mode, which means that the wing supplies approximately 30 times as much damping for the 3.62-Hz mode. Thus, the separated flow effects have negligible effect on the 3.62-Hz mode damping.

The preceding results were obtained using experimental data with solid fairings simulating the exhaust plumes. Naturally, the question of how well the solid plumes simulate gaseous plumes is pertinent. Dods et al. show that at $M = 1.6$, their solid

plumes nearly simulate the gaseous plumes (Fig. 42). However, there is a significant difference between the solid plume effects of Dods et al. (Ref. 19) and those of Brownson et al. (Ref. 18). The most significant difference between the two tests is that Brownson measured the loads on the booster, including the loads on the SRM nozzles; whereas Dods could not include loads on the nozzle because it was part of the gas supply plumbing. Other model differences were involved in the Dods model: the orbiter incidence was different (-3.0° compared to -3.5°), there was a minor length change, wing pods were removed, and the SRM domes were not simulated (Fig. 43). However, these differences are considered minor compared to the nozzle loads.

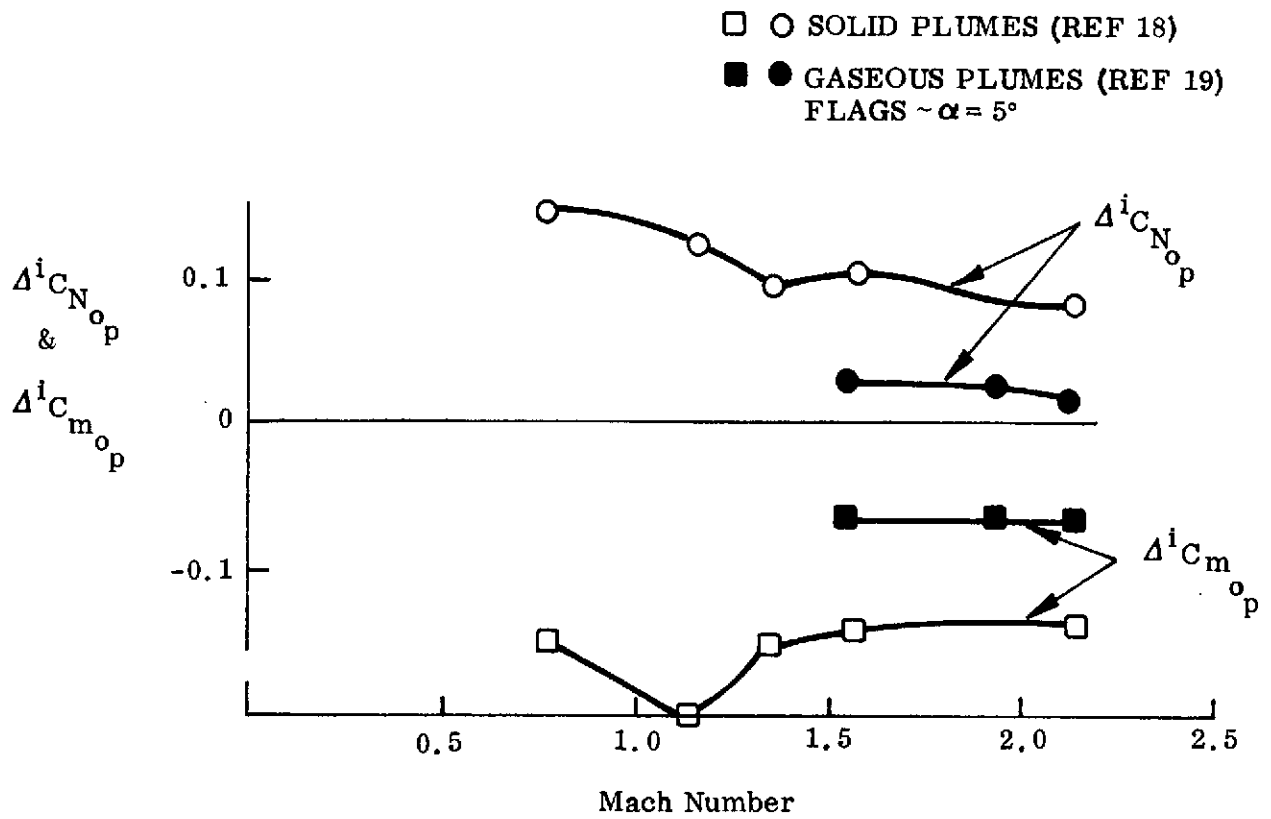
The importance of these differences is shown, for example, when damping results are compared at $M = 1.6$ (the only common Mach number) for three cases: solid plumes with nozzle loads, solid plumes without nozzle loads, and gaseous plumes without nozzle loads (Fig. 44). If the nozzle loads are assumed to be the same, the gaseous plumes would cause aerodynamic undamping of the 3.64-Hz symmetric mode if the induced load is equal to or greater than 60% of the total plume effect. The asymmetric modes are damped for all three configurations at $M = 1.6$ (Fig. 45); however, the effect of the gaseous plume is qualitatively similar to its effect in Fig. 44. That is, the plume-induced undamping is less for the gaseous plume. This is quite reasonable. The gaseous plume shape is evidently altered by crossflow effects; thus, it presents a less steep flare at angle of attack, and the resulting shock-induced separation is decreased.

The aerodynamic damping derivative by itself does not give the full answer to the unsteady flow effects on the elastic vehicle. To get a quantitative measure, the aerodynamic damping must be related to the structural damping. Fig. 46 presents the aerodynamic damping of the 049 booster in percent of critical for the 3.64-Hz symmetric mode. These values include the combined effects of solid exhaust plumes (Fig. 39) and flow separation (Fig. 35) on the booster damping. The necessary trajectory information was obtained from Ref. 26. It should be emphasized that no unsteady aerodynamic effects on the orbiter due to interference effects other than the exhaust plumes have been included. If the usual rule-of-thumb value of 1% of critical for the structural damping ($\pm 0.5\%$) is assumed, the aerodynamic undamping comes dangerously close to dominating the structural damping. Thus, the shuttle booster

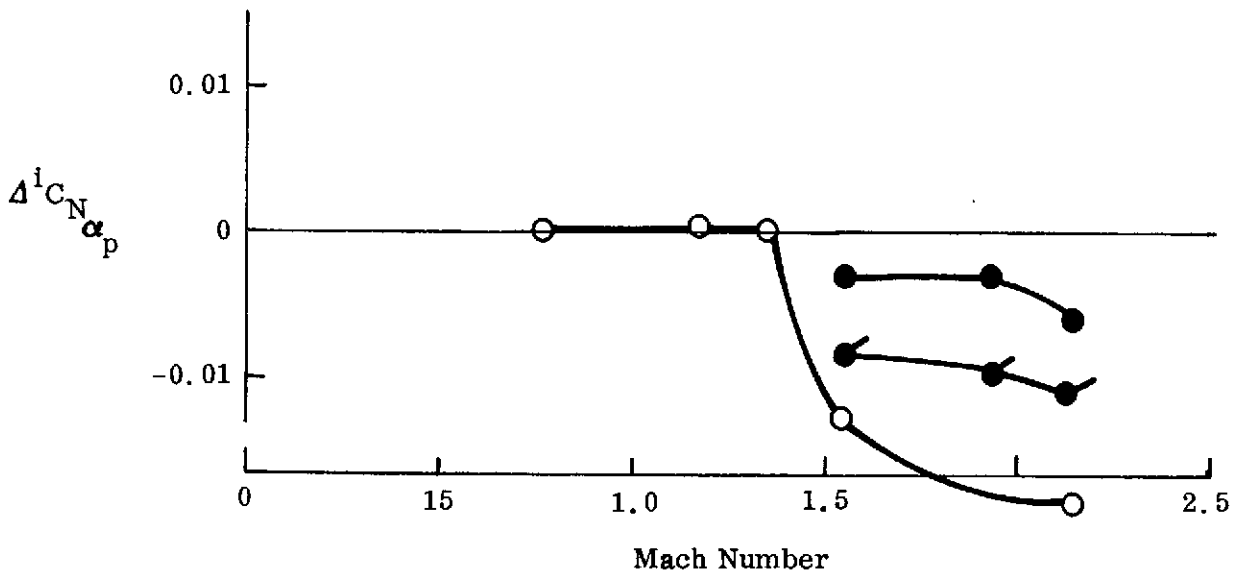
could experience undamping of this particular elastic mode. Even when one accounts for gaseous exhaust plume effects, the aerodynamic undamping is still dangerously close to overtaking the structural damping (Fig. 47).

Of course, these results are only approximate. However, they do show that negative aerodynamic damping is possible; and they indicate, therefore, that the problem requires further investigation. As stated previously, these estimates do not include unsteady flow effects on the orbiter other than the plume effects. It has been shown that the vortices from the shock-induced separation on the HO tank retro-rocket housing can affect the orbiter, as can the other booster vortices at angle of attack. Furthermore, the current configuration with the SRMs in the normal position has a greatly expanded region of flow separation forward of the orbiter. All these effects contribute further to negative aerodynamic damping.

Dods et al. obtained a vapor screen photograph during the gaseous plume tests (Ref. 19) that has some interesting implications (Fig. 48). The photograph shows SRM and orbiter plumes 15 inches aft of the 0.019 scale model at $M = 1.6$, $\alpha = -4^\circ$ (orbiter $\alpha = -7^\circ$). Traces from the leading edge vortices from the orbiter wing are evident in the upper outside edge of the SRM plumes. It is not difficult to imagine the exhaust plumes having an effect similar to Hummel's obstruction (Ref. 27), thus causing burst of the orbiter leading-edge vortices, which could result in a discontinuous change of aerodynamic characteristics (Fig. 43 of Ref. 11). At $\beta \neq 0$ the effects would be felt by the moments about all three axes as burst occurs first on one wing. It may be fortuitous, but there is also a sudden increase in the magnitude of the pitching moment induced by the gaseous plume near this angle of attack ($\alpha = -4^\circ$ in Fig. 42). This C_m change could be a sign that plume-induced vortex burst occurs on the orbiter. Burst in itself is not always serious, as has been discussed in connection with the delta-wing dynamics (Refs. 11, 28). However, the encounter of discontinuous, stepwise on-off loadings due to burst can have a large effect on the aerodynamic damping. Again, this points out the need for further investigation before one can assure the shuttle a safe ascent.

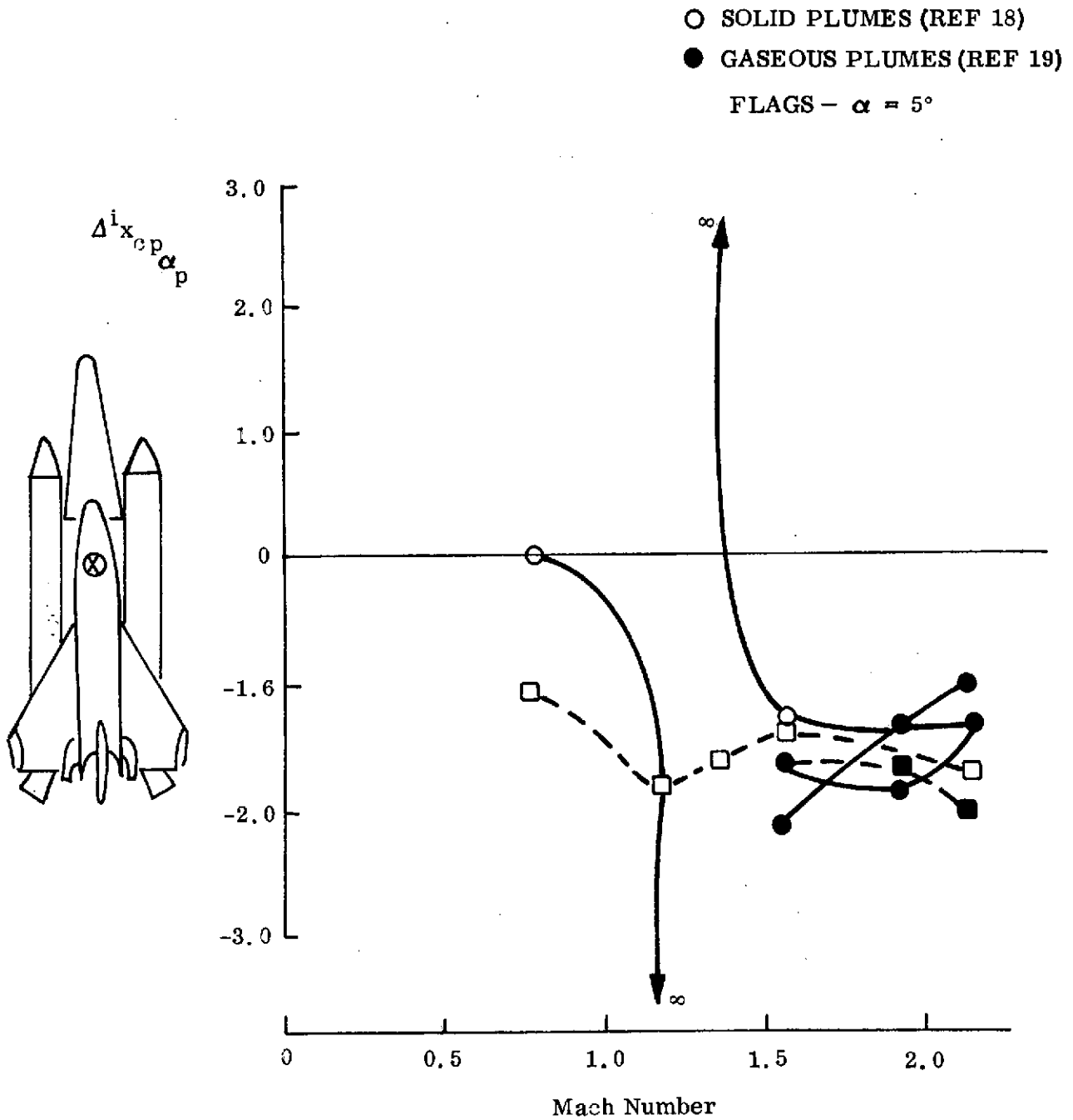


a. $\alpha = 0$ Normal Force



b. $\alpha = 0$ Normal Force Derivative

Figure 36. Plume-Induced Effects on Pitch Stability, #040A Booster
 (Sheet 1 of 2)



c. Center of Pressure

Figure 36. Plume-Induced Effects on Pitch Stability, 040A Booster
(Sheet 2 of 2)

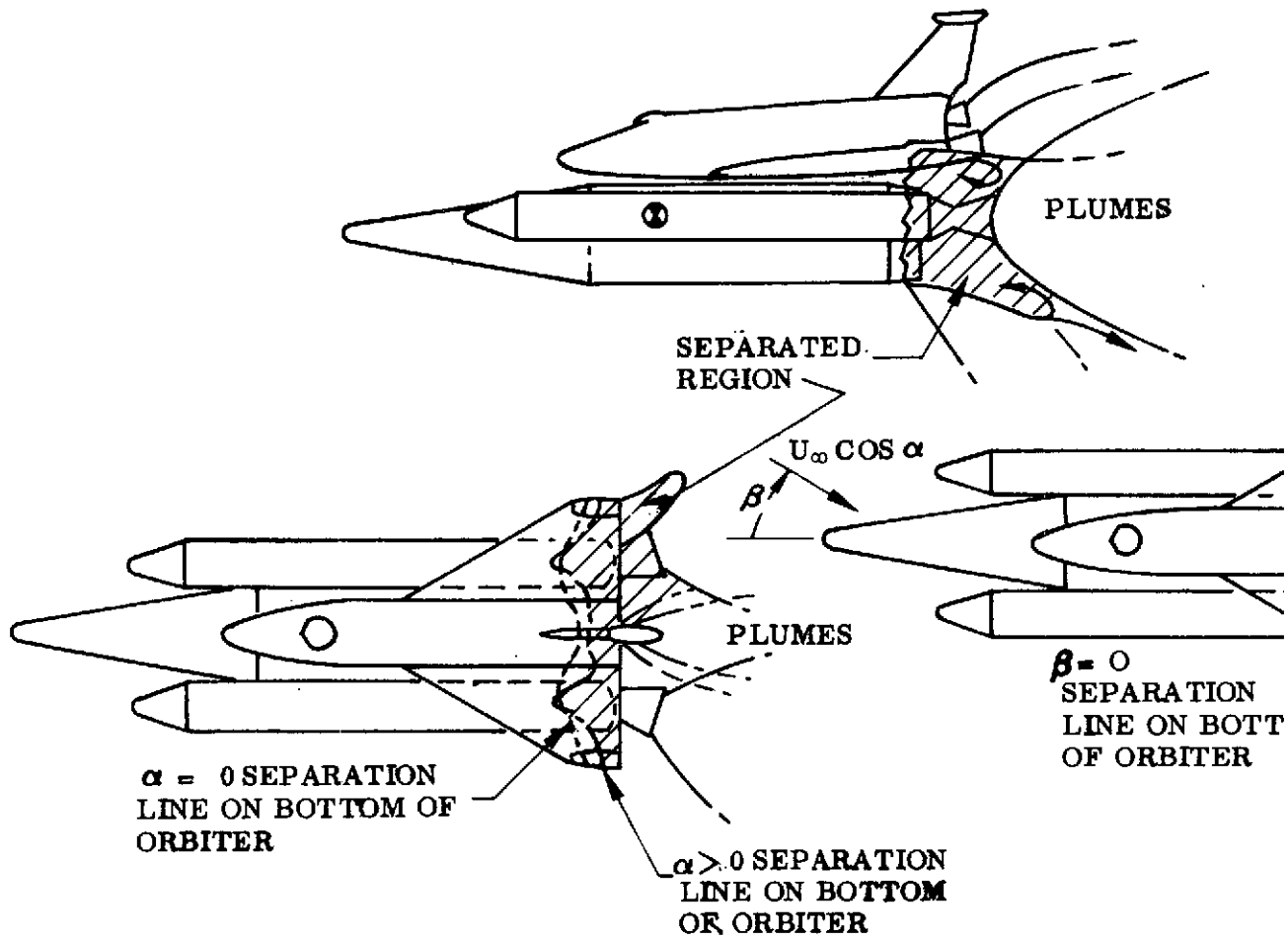


Figure 37. Postulated Effects of Small α and β on Plume-Induced Sep

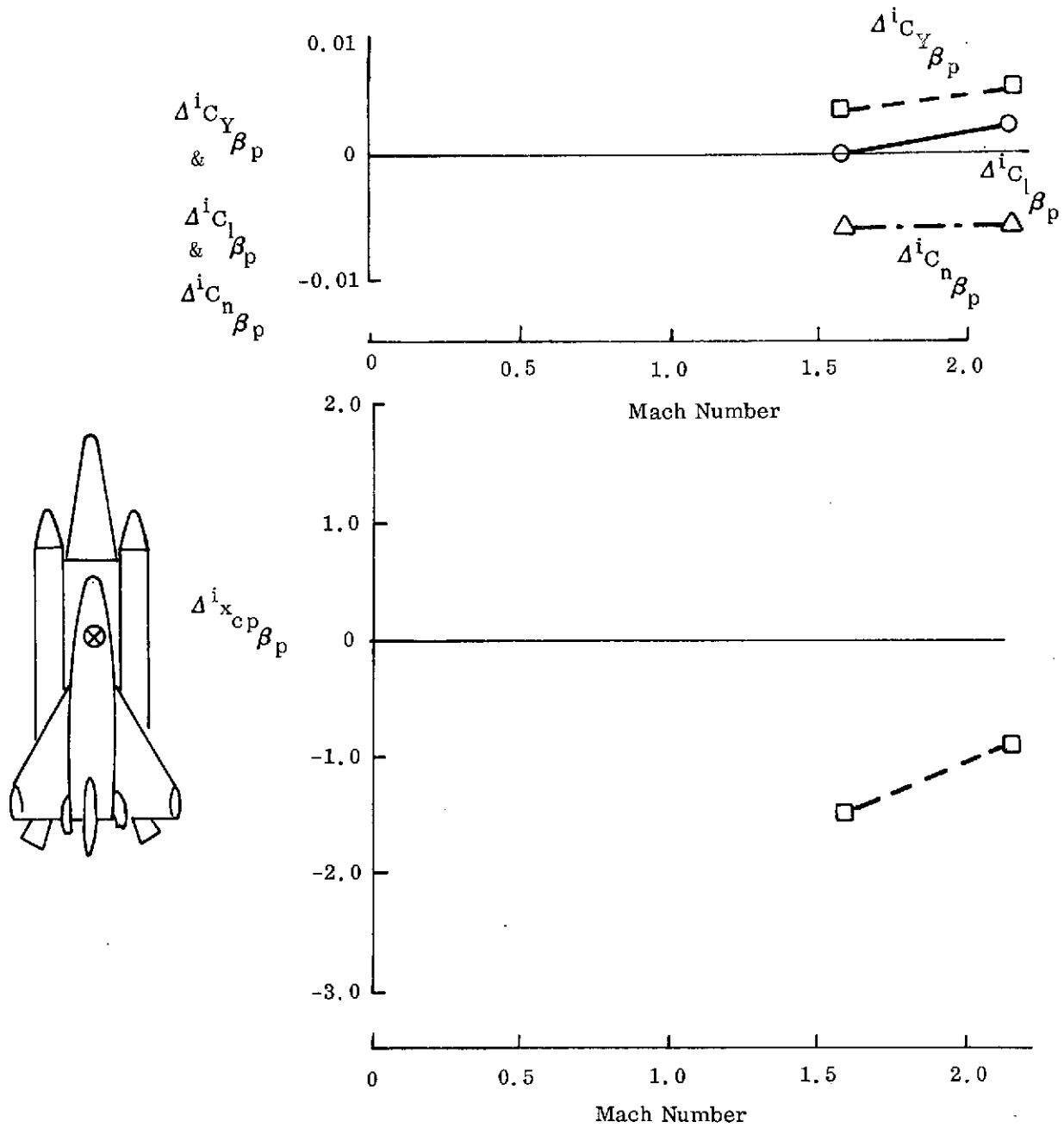


Figure 38. Plume-Induced Effects on Directional Stability, 040A Booster (Ref. 18)

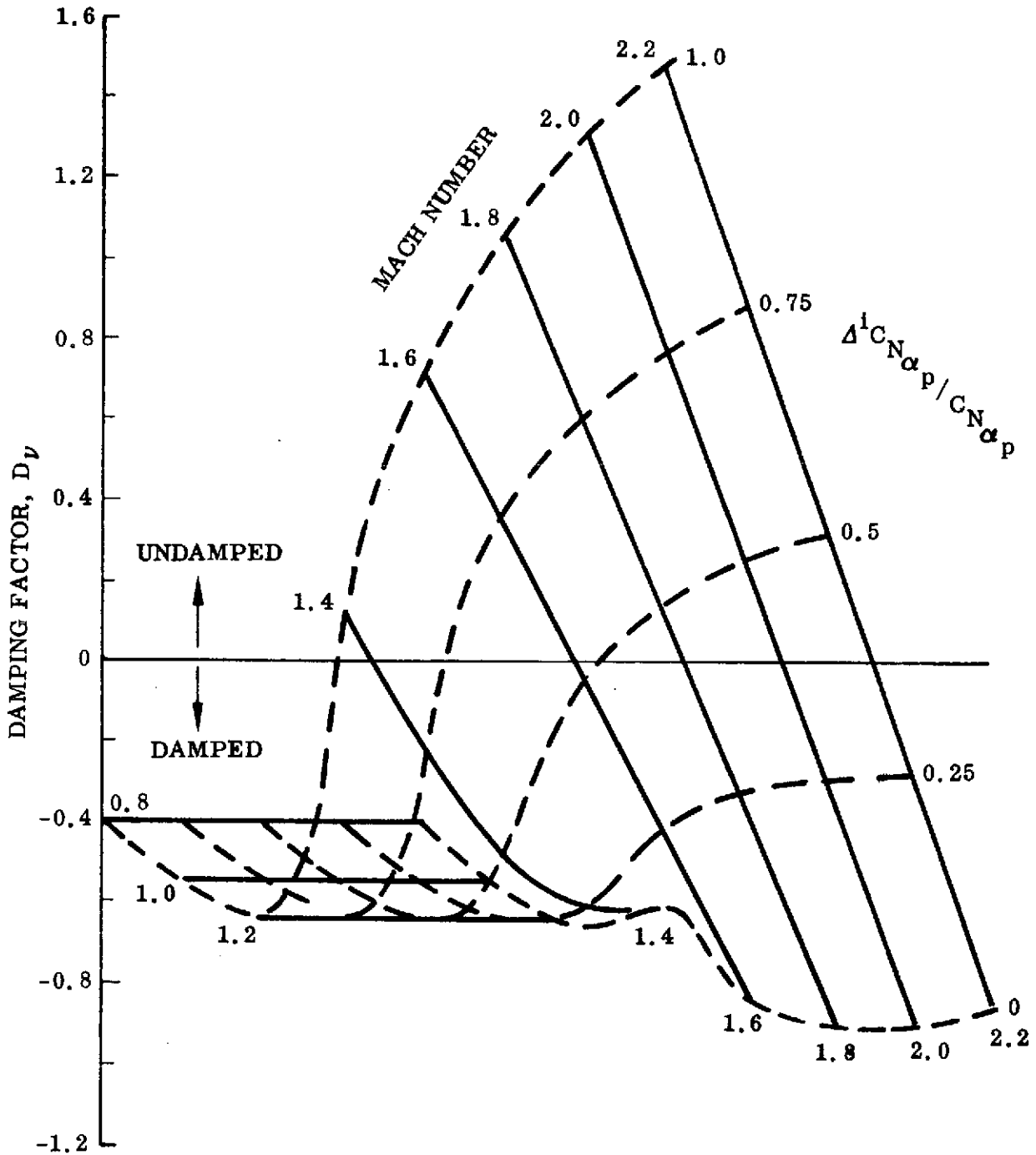
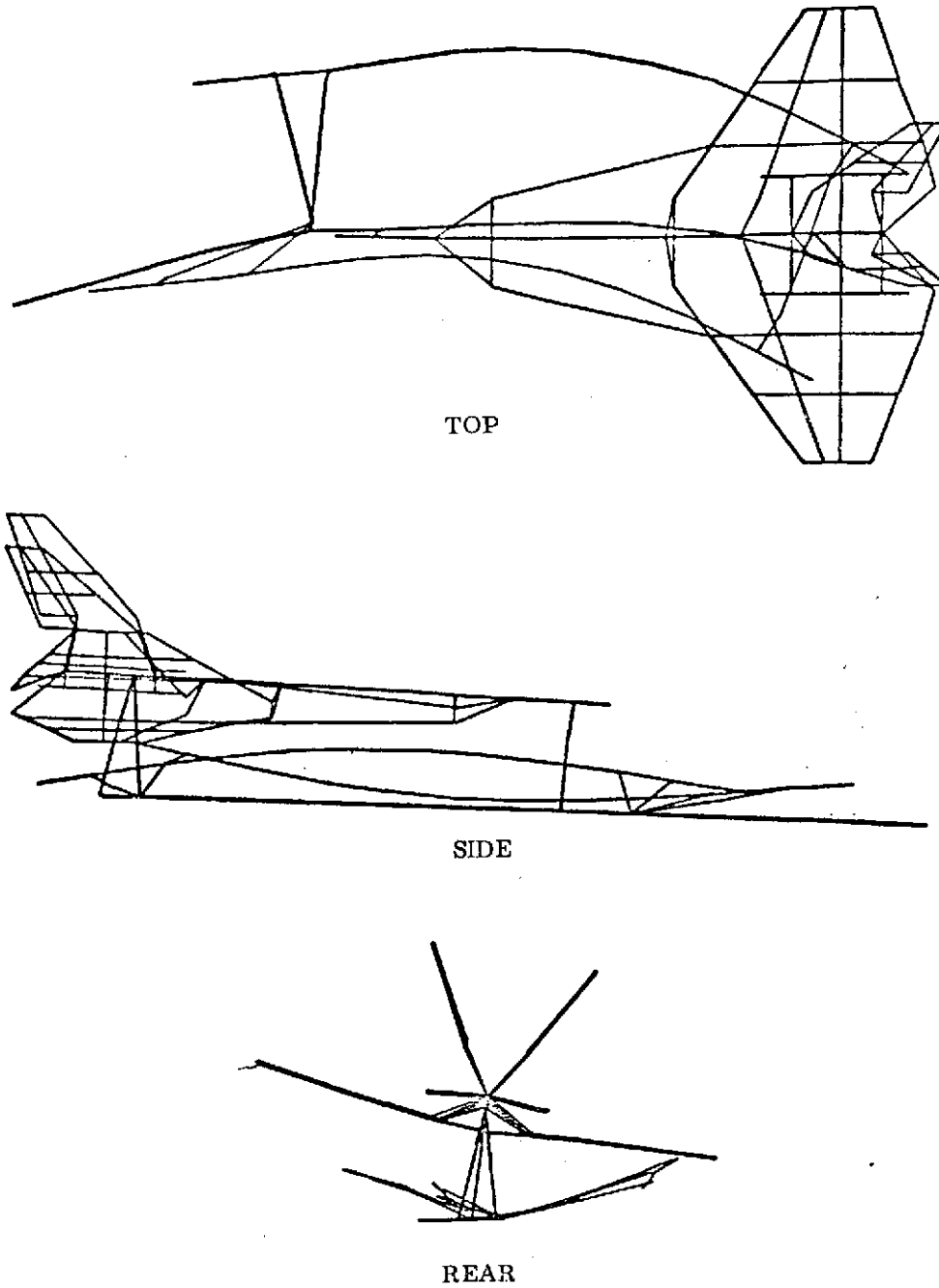
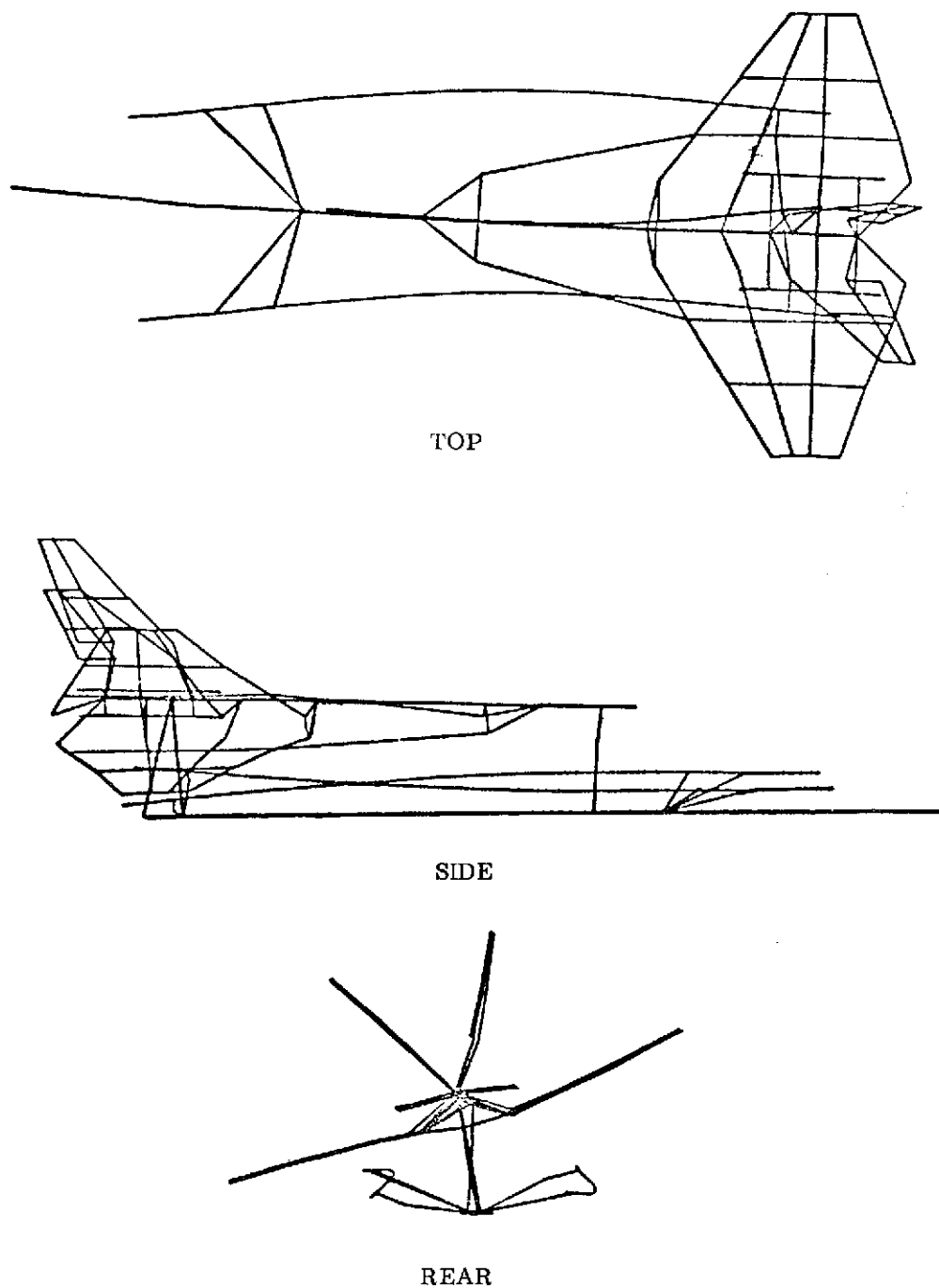


Figure 39. Effect of Solid Plumes on the Aerodynamic Damping Factor of the 3.64 Hz Symmetric Mode of the 049 Booster



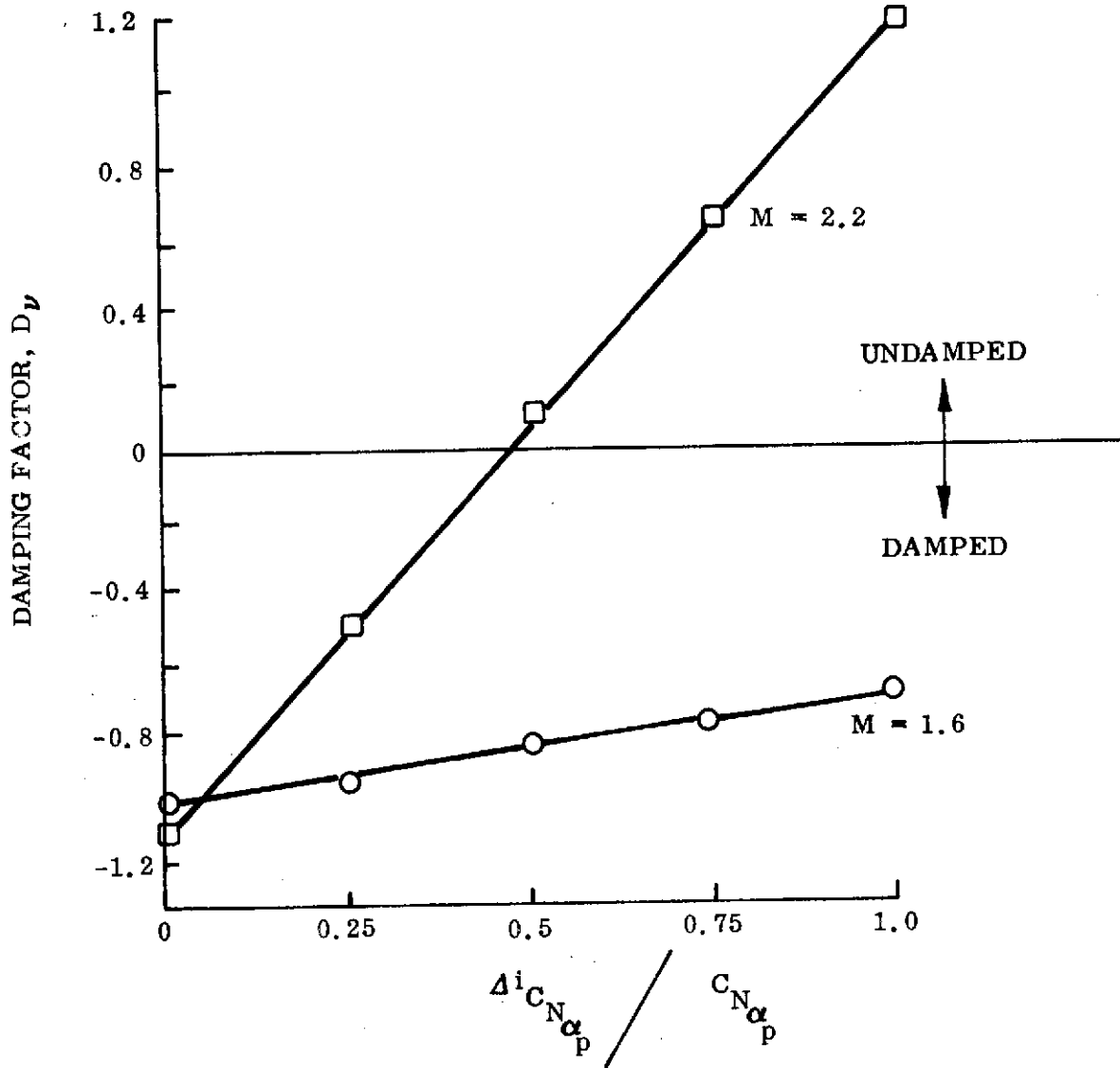
a. 2.76 Hz Asymmetric Mode

Figure 40. Typical Asymmetric Modes of the 049 Booster (Ref. 17)
(Sheet 1 of 2)



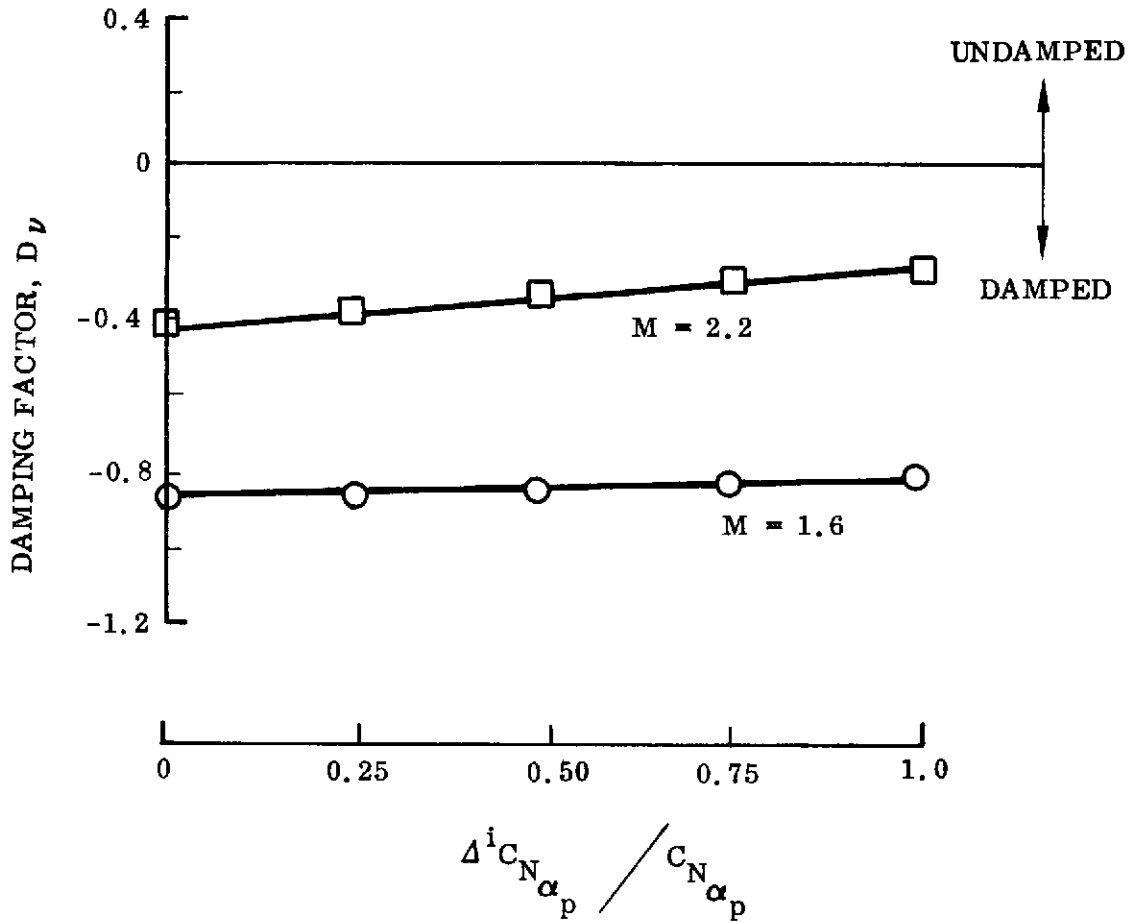
b. 3.62 Hz Asymmetric Mode

Figure 40. Typical Asymmetric Modes of the 049 Booster (Ref. 17)
(Sheet 2 of 2)



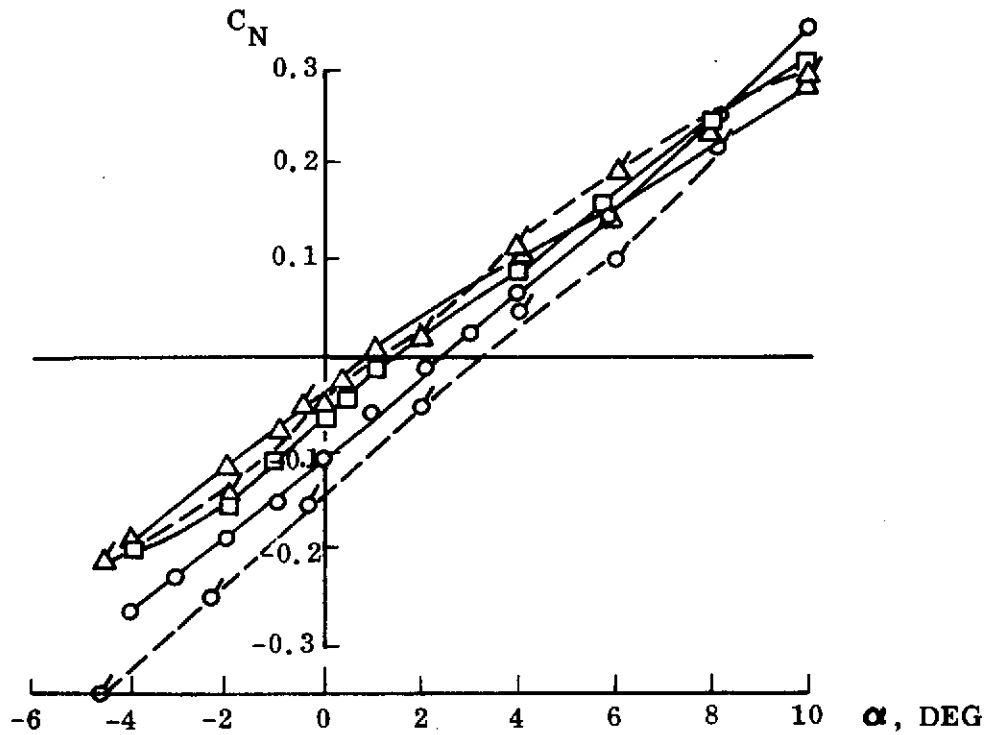
a. 2.76 Hz A Symmetric Mode

Figure 41. Effect of Solid Plumes on the Aerodynamic Damping Factor of Some Typical Asymmetric Modes of the 049 Booster (Sheet 1 of 2)



b. 3.62 Hz ASYMMETRIC MODE

Figure 41. Effect of Solid Plumes on the Aerodynamic Damping Factor of Some Typical Asymmetric Modes of the 049 Booster (Sheet 2 of 2)



WITHOUT NOZZLE LOADS (REF 19)

- NO PLUMES
- △ SOLID PLUMES
- GASEOUS PLUMES

WITH NOZZLE LOADS (REF. 18)

- - ○ NO PLUMES
- - △ SOLID PLUMES

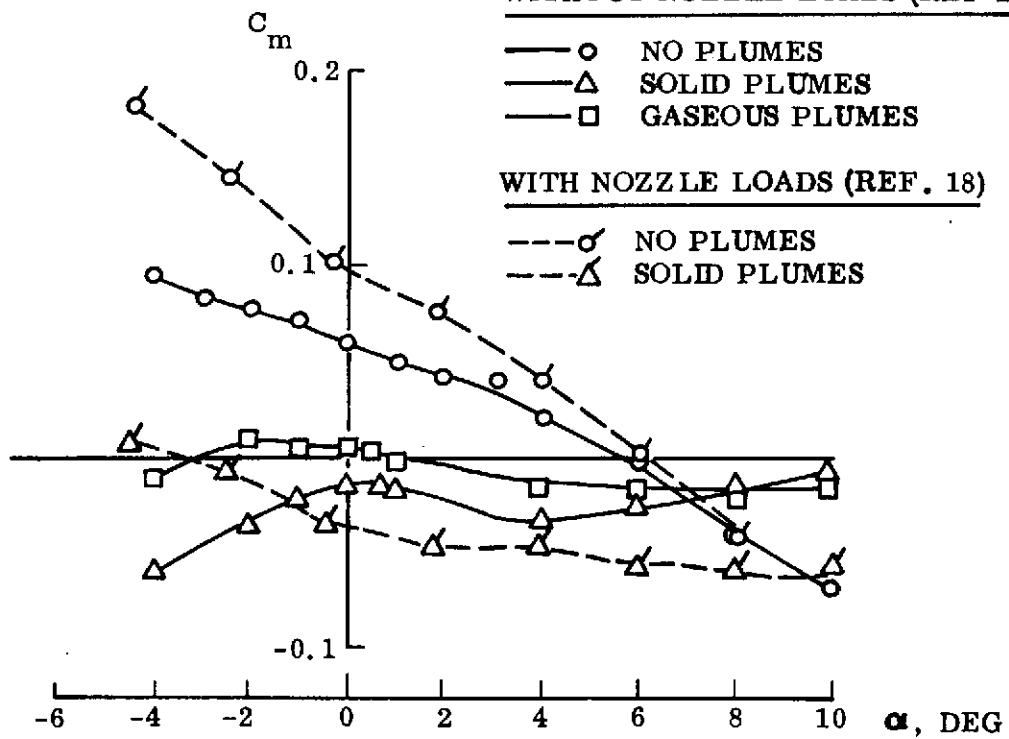
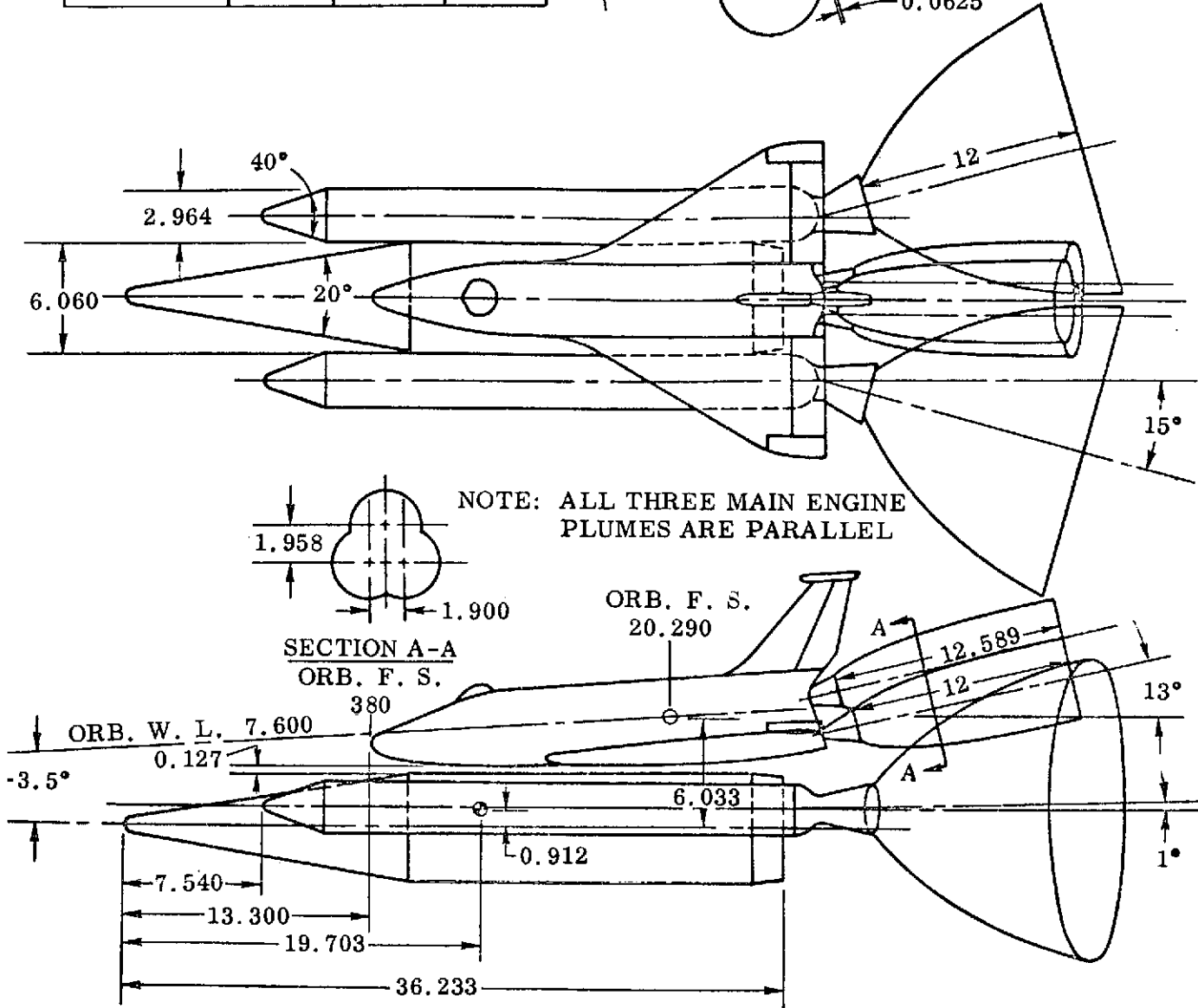
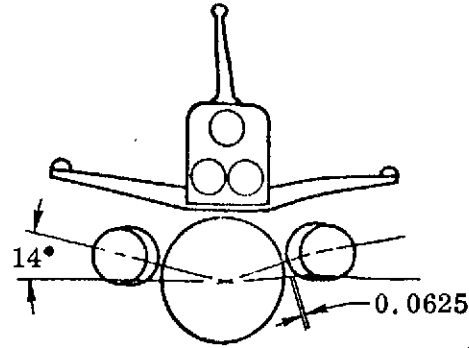


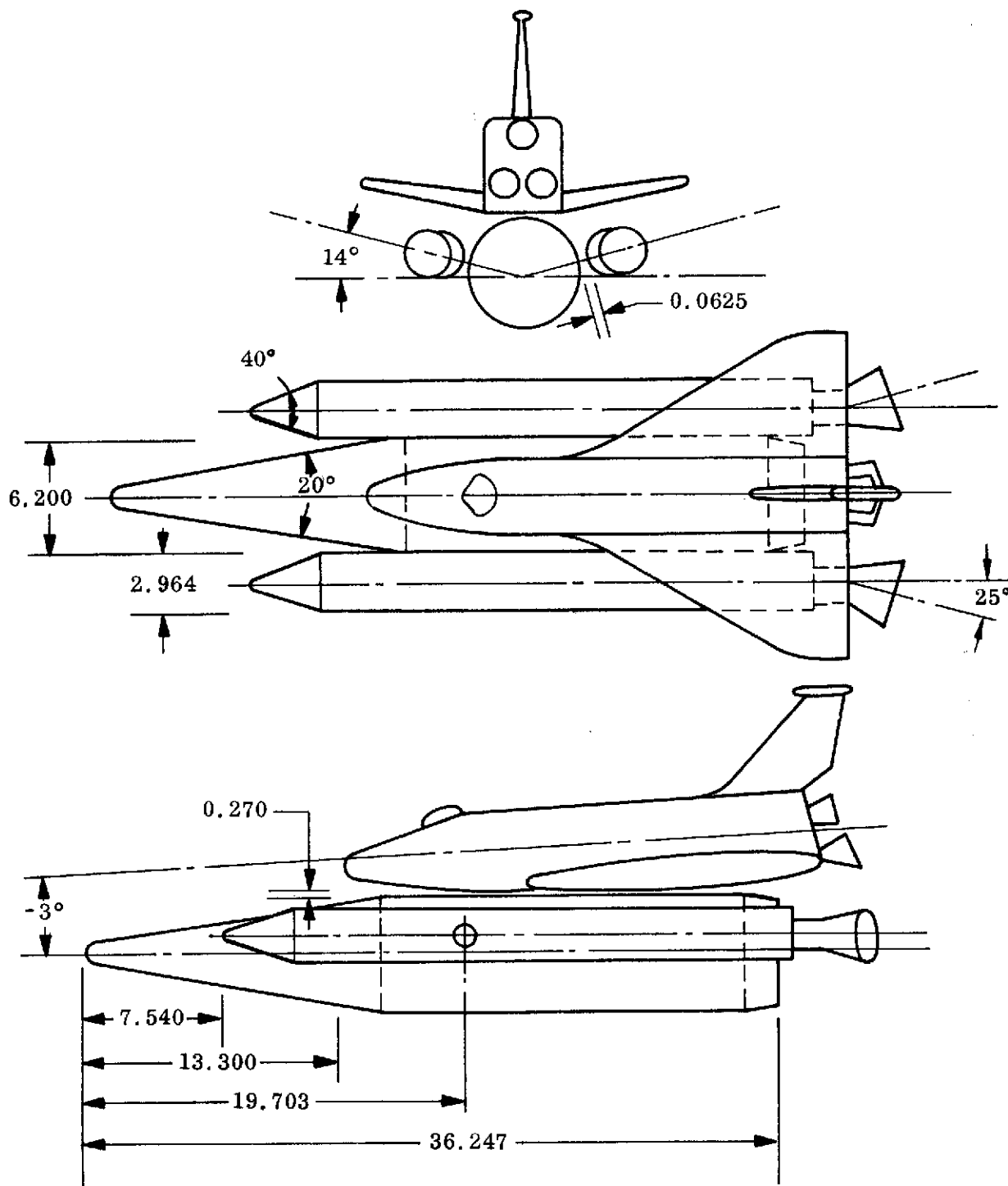
Figure 42. Comparison of Solid and Gaseous Plumes and Nozzle Load Effects

LOCATION OF CENTER OF NOZZLE EXIT PLANE FROM TANK NOSE AND C			
	X	Y	Z
ORB. TOP	39.113	0	7.440
ORB. BOT.	40.128	±1.90	5.662
SRM	42.114	±5.403	1.172



a) Booster Configuration for Solid Plume Tests (Ref. 18)

Figure 43. Comparison of Configurations Used in Plume Tests (Sheet 1 of 2)



b. Booster Configuration For Gaseous Plume Tests (Ref 19)

Figure 43. Comparison of Configurations Used in Plume Tests
(Sheet 2 of 2)

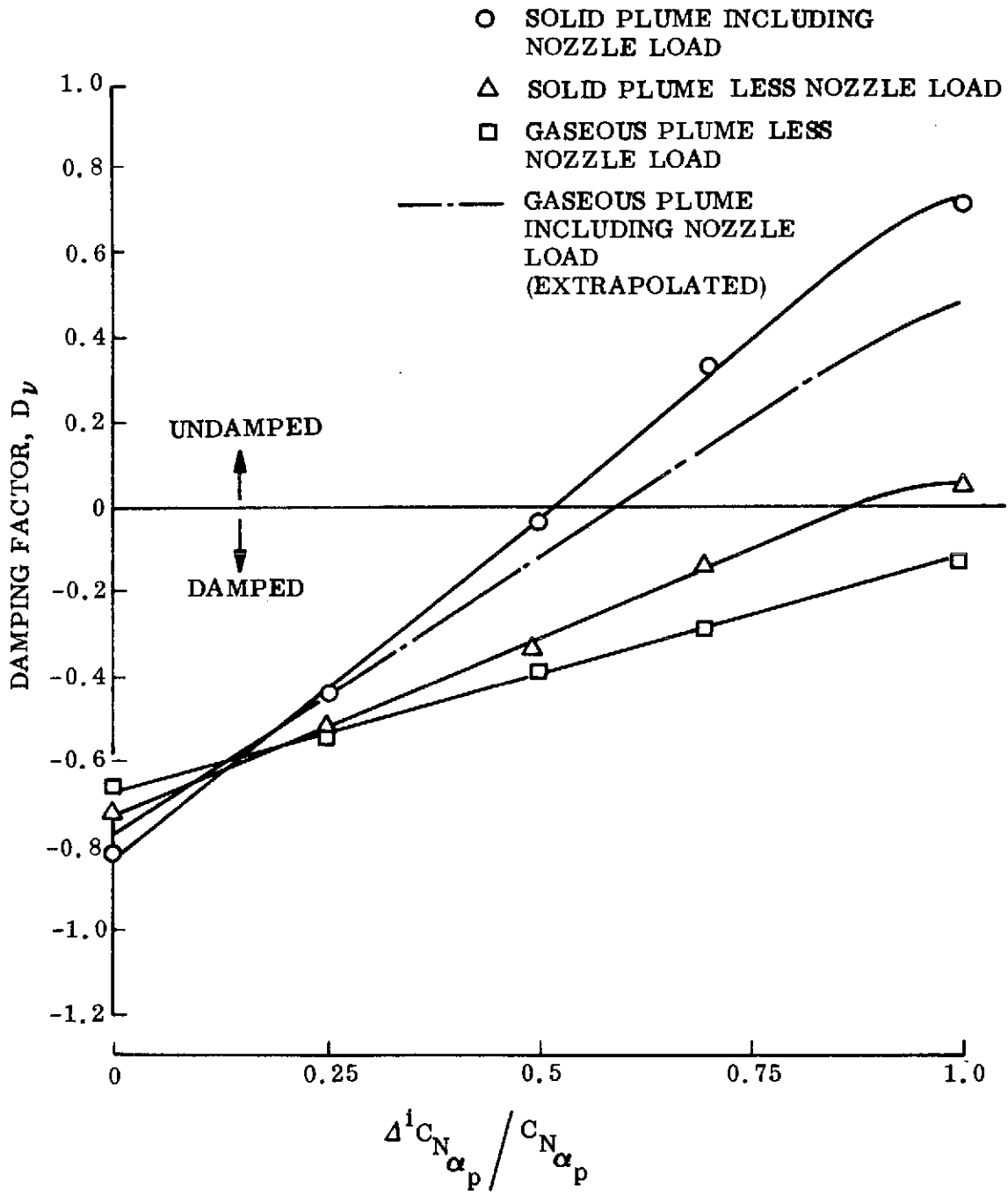


Figure 44. Effect of Gaseous Plumes and Nozzle Loads on the Aerodynamic Damping Factor of the 3.64 Hz Symmetric Mode of the 049 Booster, $M = 1.6$

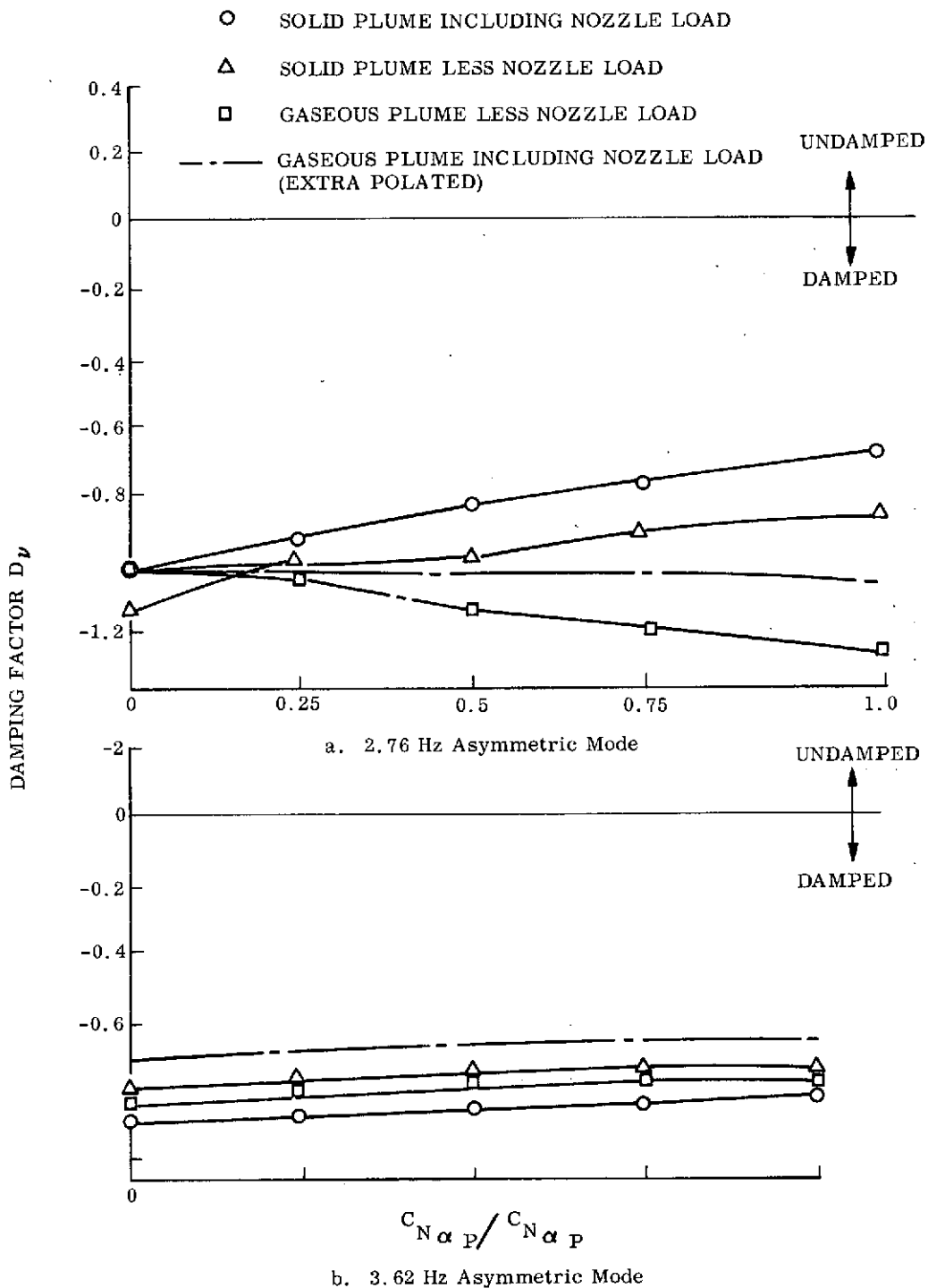


Figure 45. Effect of Gaseous Plumes and Nozzle Loads on the Aerodynamic Damping Factor of Some Typical Asymmetric Modes of the 049 Shuttle Booster, $M = 1.6$

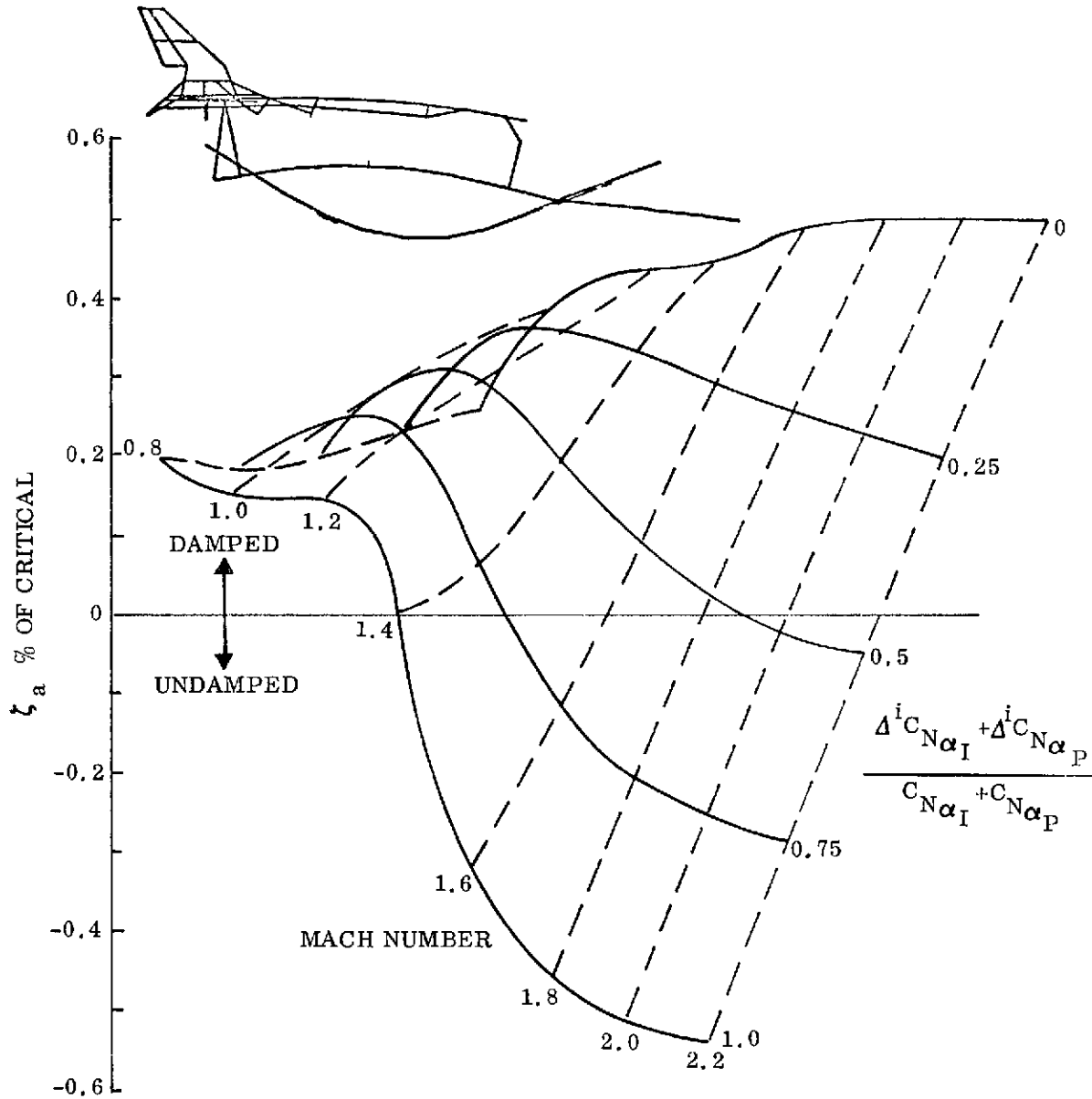


Figure 46. Effect of Solid Plumes and Booster Interference on the Aerodynamic Damping of the 3.64-Hz Symmetric Mode of the 049 Booster

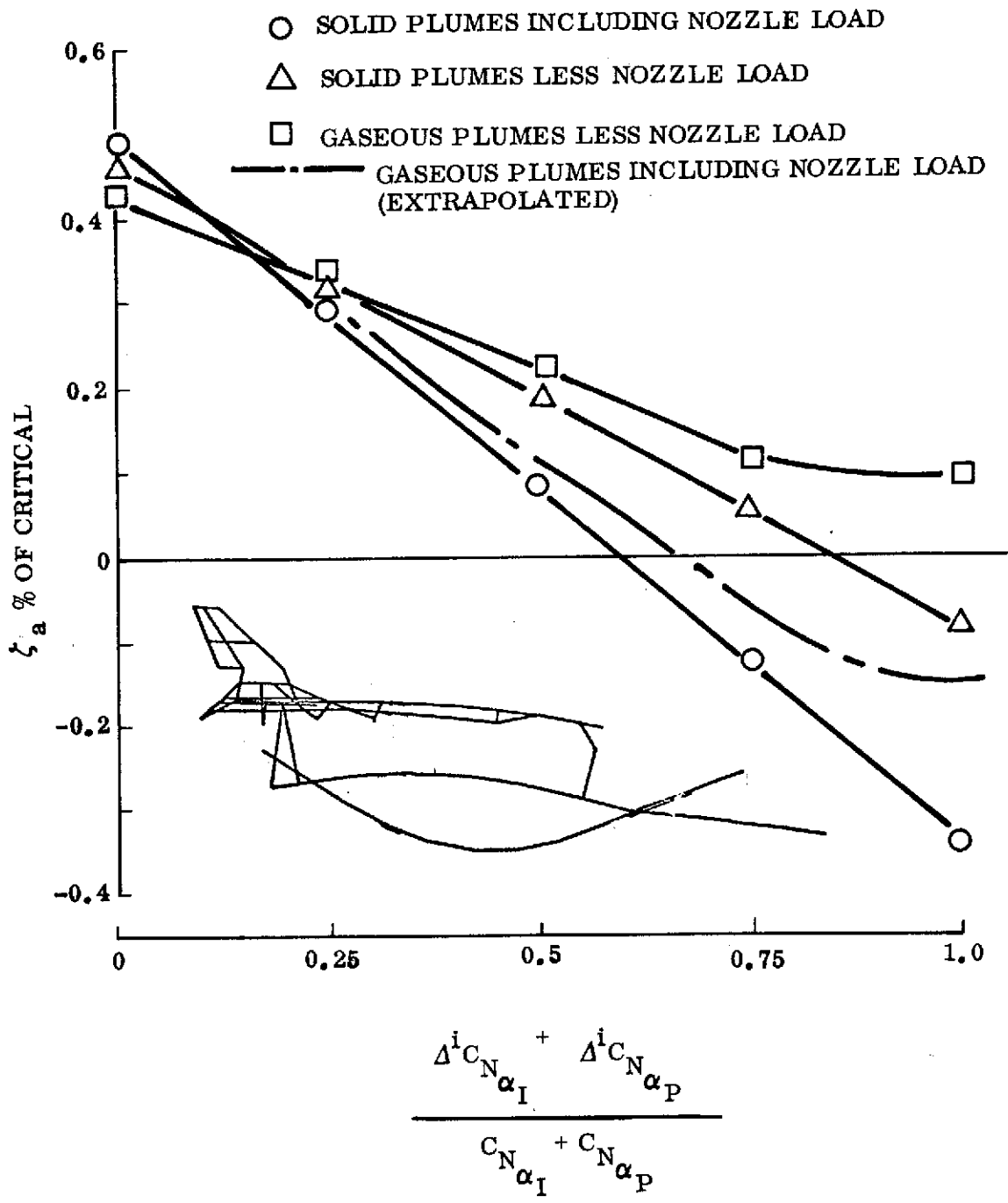


Figure 47. Effect of Gaseous Plumes and Booster Interference on the Aerodynamic Damping of the 3.64-Hz Symmetric Mode of the 049 Booster, M = 1.6

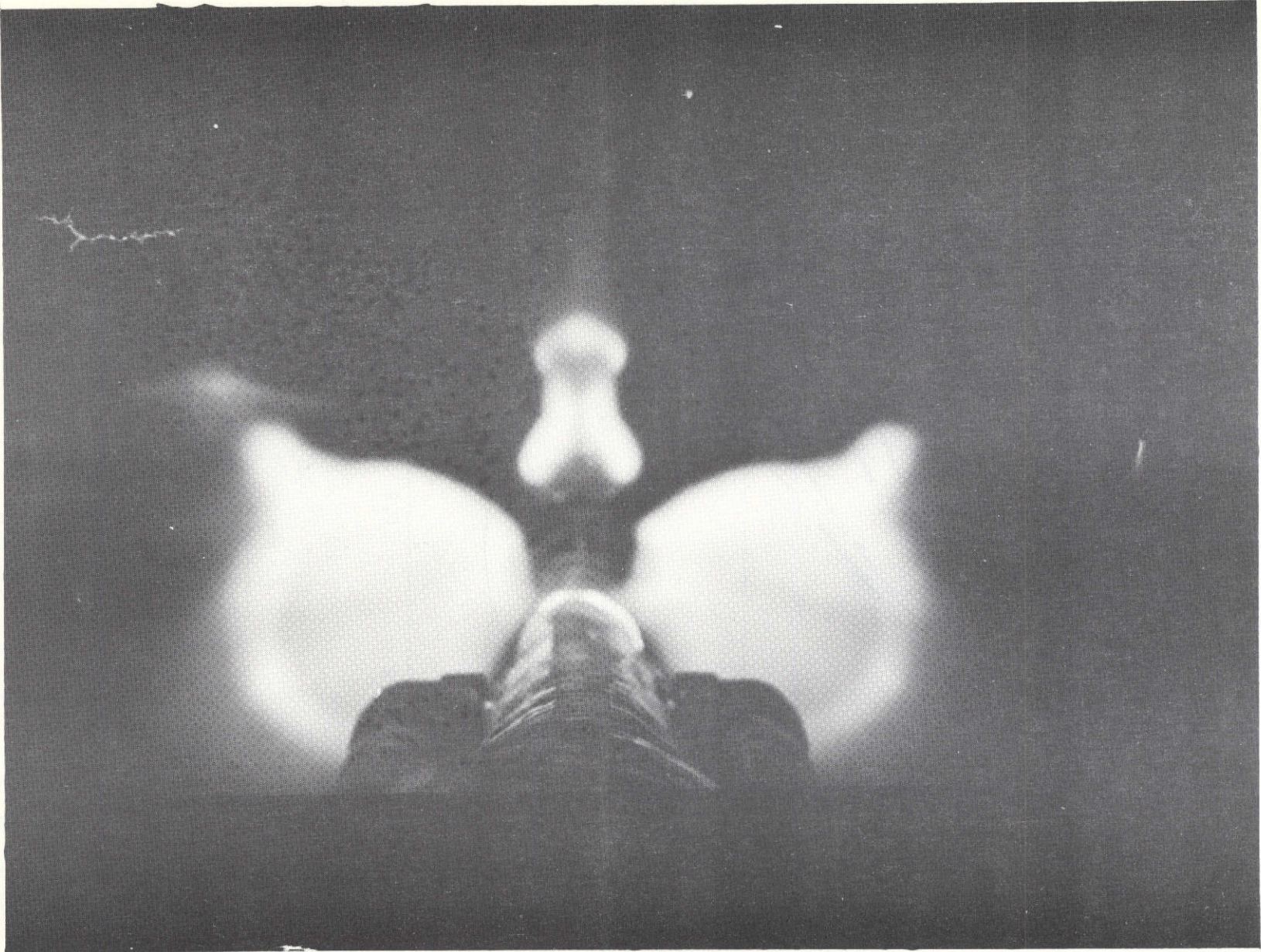


Figure 48. Evidence of Leading Edge Vortex-Exhaust Plume Interaction, 15 Inches Downstream of Nozzles, $M = 1.6$, $\alpha = -4^\circ$

(Courtesy of Jules Dods, NASA Ames Research Center)

Section 5
CONCLUSIONS

An investigation of the interference flow field on the space-shuttle boost configuration has shown that interference effects can dominate the shuttle aerodynamics. Preliminary order-of-magnitude estimates of the aeroelastic stability of the shuttle booster have been made. The results indicate the possibility of negative aerodynamic damping for at least one of the elastic modes of magnitudes sufficient to dominate the structural damping. Since the implication of these results is possible structural failure, further experimental and theoretical investigations are warranted.

Unfortunately, the results are not for the current configuration, which has a more severe flow separation on the HO tank. Furthermore, they do not include the unsteady aerodynamic interference effects on the leeside of the orbiter, which could be significant. Thus, the unsteady aerodynamic effects could possibly be even more adverse than these first estimates indicate.

The understanding of the unsteady aerodynamics gained from this preliminary investigation, which necessarily had to depend on incomplete information scattered over a number of different configurations, is encouraging. Good quality flow-visualization data combined with pressure distribution and force data on the correct configuration could supply the needed information for successful aeroelastic analysis of the space shuttle booster. Furthermore, as illustrated in the present report, such an analysis can reveal the causes of detrimental effects on the aeroelastic stability so that they can be eliminated. This should be done as early in the design period as possible, before it becomes very inconvenient or expensive to effect necessary configuration changes.

Section 6

RECOMMENDATIONS FOR FURTHER STUDY

The fact that the present analysis, rough and rather speculative as it is, predicts negative aerodynamic damping of at least one elastic mode indicates that the problem is sufficiently serious to warrant further investigation. Analytic tools are essentially in hand to predict the aeroelastic stability of the shuttle booster, provided that the proper static data and a thorough understanding of the flow phenomena are available. The experimental results that will supply the needed input data for this analysis is outlined briefly below.

First, a consistent set of static experimental data for the correct configuration is required. The bulk of the data required is the usual static aerodynamic data used for design (e. g. , pressure distribution results and force data on each body element). In order to determine which portion of each load component is due to local flow conditions and which portion is due to flow conditions elsewhere, it is recommended that each body element (HO tank, SRM, orbiter) be pitched and yawed in the presence of the others. This should be done for both pressure distribution and static force tests. This is a special requirement for the aeroelastic analysis. However, much of the data from the separate perturbation of each body element will also be of use in the analysis of ascent separation dynamics (Ref. 29).

The oilflow results proved invaluable in the present analysis. Likewise, oilflow photographs will be an essential part of any further analysis. Finally, the validity of the analysis can be checked without resorting to very expensive aeroelastic wind tunnel tests by performing special rigid-body dynamic tests similar to those done for the Apollo-Saturn boosters (Ref. 30). The response (force, moment, phase shift) of each body element should be measured while the other elements are oscillated one by one. This will allow verification of the dynamic effects of the interference loads (Ref. 31).

Section 7

REFERENCES

1. Fournier, R. and Spencer, B., Jr., "Aerodynamic Stability and Control Characteristics of a .01925 Scale Model NR ATP Orbiter at Mach Numbers from 1.9 to 4.63," NASA DMS-DR-2001, November 1972.
2. Spencer, B. and Mennell, R., "Results of Transonic Tests in the NASA/LaRC 8 Foot Pressure Tunnel on a 0.015 Scale Model NR-PPR Space Shuttle Orbiter," NASA CR 128, 752, March 1973.
3. Hamilton, J. T., Rampy, J. M., and Sims, J. F., "Preliminary Pressure Distributions on the 049 Orbiter, Orbiter in Presence of H/O Tank and Orbiter in Launch Configuration," NASA CR 120, 066, January 1973.
4. Hama, F. R., "Experimental Studies on the Lip Shock," AIAA Paper No. 67-29, AIAA 5th Aerospace Sciences Meeting, New York, N. Y., January 23-26, 1967.
5. Ericsson, L. E., Reding, J. P., and Guenther, R. A., "Analytic Difficulties in Predicting Dynamic Effects of Separated Flow," Journal of Spacecraft and Rockets, Vol. 8, No. 8, August 1971, pp. 872-878.
6. Treon, S. L., "Effects of Nose-Cone Angle on the Transonic Aerodynamic Characteristics of a Blunt Cone-Cylinder Body Having a Cylindrical, Flared, or Blunt-Finned Afterbody," NASA TM X-582, October 1961.
7. Edney, B. E., "Effects of Shock Impingement on the Heat Transfer around Blunt Bodies," AIAA Journal, Vol. 6, No. 1, June 1968, pp. 15-23.
8. Reding, J. P. and Ericsson, L. E., "Unsteady Aerodynamic Analysis of Space Shuttle Vehicles, Part IV, Effect of Control Deflections on Orbiter Unsteady Aerodynamics," LMSC-D352320, Part IV, August 1973.
9. Reding, J. P., French, N. J., Jecmen, D. M., and Ericsson, L. E., "The Aeroelastic Characteristics of the Saturn-IB and Saturn-V Launch Vehicles," M-37-65-1, March 1965, Lockheed Missiles & Space Company.

10. Kuehn, Donald M., "Turbulent Boundary-Layer Separation Induced by Flares on Cylinders at Zero Angle of Attack," NASA TR-117, 1961.
11. Ericsson, L. E. and Reding, J. P., "Unsteady Aerodynamic Analysis of Space Shuttle Vehicles, Part II, Steady and Unsteady Aerodynamics of Sharp-Edged Delta Wings," LMSC-D352320, Part II, August 1973.
12. Lott, R. A. and Ramsey, P., "An Investigation of the Load Distribution over the SRB and External Tank of a 0.004 Scale Model of the 049 Space Shuttle Launch Configuration," NASA CR 120, 058, March 1973.
13. Chevalier, H. L. and Robertson, J. E., "Pressure Fluctuations Resulting from an Alternating Flow Separation and Attachment at Transonic Speeds," AEDC TDR 63-204, November 1963.
14. Anon., "Handbook of Supersonic Aerodynamics, Section 8, Bodies of Revolution," NAVWEPS Report 1488 (Vol. 3), October 1961.
15. Ericsson, L. E. and Reding, J. P., "Analysis of Flow Separation Effects on the Dynamics of a Large Space Booster," Journal of Spacecraft and Rockets, Vol. 2, No. 4, July-Aug. 1965, pp. 481-490.
16. Ericsson, L. E. and Reding, J. P., "Report on Saturn I-Apollo Unsteady Aerodynamics," LMSC-A656215, February 1964, Lockheed Missiles & Space Company.
17. Low, P. F. and Stuhlman, C. E., "Lift-off Vibration Characteristics MSC Model 049 Shuttle Configuration," Northrop Services, Inc., internal document 9243D-72-11, August 16, 1972.
18. Brownson, J. J., Whitnah, A. M., Kassner, D. L., and Rampy, J., "Aerodynamic Characteristics of an 040A Space Shuttle Configuration with Simulated Rocket Plumes at Mach Numbers from 0.8 to 2.2," NASA TM X-62, 126 (SSPD-88), September 1972.
19. Dods, J. B., Jr., Brownson, J. J., Blackwell, K. L., Decker, J. P., and Roberts, B. B., "Effect of Gaseous and Solid Simulated Rocket Plumes on an 040A Space Shuttle Configuration at Mach Numbers from 1.6 to 2.3," Prospective NASA TM.

20. Reding, J. P. and Ericsson, L. E., "Dynamic Support Interference," Journal of Spacecraft and Rockets, Vol. 9, No. 7, July 1972, pp. 547-553.
21. Henderson, A., Jr., "Aerothermodynamic Technology for Space Shuttle - and Beyond," AIAA Paper 73-59, Presented at the AIAA 9th Annual Meeting and Technical Display, January 1973.
22. Ellis, R. and Gamble, M., "Static Stability and Control Effectiveness of a Parametric Launch Vehicle," NASA CR 120, 059, July 1972.
23. Sims, F., "Aerodynamic Stability and Drag Characteristics of a Parallel Burn/SRM Ascent Configuration ($M = 0.6$ to 4.96)," NASA CR 120, 055, April 1972.
24. Weaver, J., Ellis, R. R., and Gamble, M., "Aerodynamic Characteristics of a Double Delta Wing Space Shuttle Orbiter ($M = 0.6 - 5.0$)," NASA CR 120, 051, August 1972.
25. Liepman, H. W. and Roshko, A., Elements of Gasdynamics, John Wiley and Sons Inc., New York, N. Y., 1957.
26. Anon., "Aerodynamic Design Data Book, Vol. I," North American Rockwell Report SD72-SH-60-1, 1972.
27. Hummel, D., "Untersuchungen über das Aufplatzen der Wirbel an schlanken Delta-flügeln," Zeitschrift für Flugwissenschaften 13, 1965, pp. 158-168.
28. Reding, J. P. and Ericsson, L. E., "Effects of Delta Wing Separation on Shuttle Dynamics," Journal of Spacecraft and Rockets, Vol. 10, No. 7, July 1973, pp. 421-428.
29. Orlik-Rückeman, K. J., LaBerge, J. G., and Hanff, E. S., "Experiments on the Dynamic Stability of the Space Shuttle," Space Shuttle Aerothermodynamics Technology Conference, Volume III Aerodynamics, NASA TM X-2508, December 15-16, 1971.
30. Reding, J. P., "Partial Simulation of Elastic-Body Dynamics for the Upper-Stage Apollo-Saturn Launch Vehicle" LMSC-M-37-67-4, December 1967. Lockheed Missiles & Space Company, Inc.
31. Orlik-Rückeman, K. J., "Survey of Needs and Capabilities for Wind Tunnel Testing of Dynamic Stability of Aircraft at High Angles of Attack," NASA CR-114583, 1973.

Appendix A
NOMENCLATURE

A	axial force coefficient $C_A = A/(\rho_\infty U_\infty^2/2) S$
a	speed of sound
AR	aspect ratio, $AR = b^2/S$
b	wing span
c	reference length (mean aerodynamic chord)
c_ℓ	local chord
D_ν	equivalent elastic body damping derivative
f	frequency
L	vehicle length
ℓ	rolling moment: coefficient $C_\ell = \ell/(\rho_\infty U_\infty^2/2) Sb$
M	Mach number, $M = a/U$
M_p	pitching moment: coefficient $C_m = M_p/(\rho_\infty U_\infty^2/2) Sc$
N	normal force: coefficient $C_N = N/(\rho_\infty U_\infty^2/2) S$
n	yawing moment: coefficient $C_n = n/(\rho_\infty U_\infty^2/2) Sb$
p	pressure: coefficient $C_p = (p - p_\infty)/(\rho_\infty U_\infty^2/2)$
p	roll rate
S	reference area, wing planform area for delta wing
t	time
U, U_∞	free stream velocity
\bar{U}	convection velocity
x	horizontal coordinate

Y	side force: coefficient $C_Y = Y/(\rho_\infty U_\infty^2/2) S$
y	lateral coordinate
z	vertical coordinate
α	angle of attack
β	sideslip angle
Δ	increment
ξ	damping, fraction of critical
ρ	air density
ϕ	roll angle
ψ	yaw angle
ω	oscillation frequency, $\omega = 2\pi f$

Subscripts

a	aerodynamic
I	interference
p	plume
α	$\partial/\partial\alpha$
β	$\partial/\partial\beta$

Superscripts

i	induced, e. g., $\Delta^i C_N =$ separation induced lift coefficient
---	--